3-6-2007

Characterizationn of Polumer-Based MEMS Pyroelectic Infrared Detector

Mark E. Allard

CHARACTERIZATION OF A POLYMER-BASED MEMS PYROELECTRIC INFRARED DETECTOR

THESIS

Mark E. Allard, 1st Lieutenant, USAF

AFIT/GEO/ENG/07-01

DEPARTMENT OF THE AIR FORCE
AIR UNIVERSITY

AIR FORCE INSTITUTE OF TECHNOLOGY

Wright-Patterson Air Force Base, Ohio

The views expressed in this thesis are those of the author and do not reflect the official policy or position of the United States Air Force, Department of Defense, or the U.S. Government.

AFIT/GEO/ENG/07-01

CHARACTERIZATION OF A POLYMER-BASED MEMS PYROELECTRIC INFRARED DETECTOR

THESIS

Presented to the Faculty

Department of Electrical and Computer Engineering

Graduate School of Engineering and Management

Air Force Institute of Technology

Air University

Air Education and Training Command

In Partial Fulfillment of the Requirements for the

Degree of Master of Science in Electrical Engineering

Mark E. Allard, BS

1st Lieutenant, USAF

March 2007

AFIT/GEO/ENG/07-01

CHARACTERIZATION OF A POLYMER-BASED MEMS PYROELECTRIC INFRARED DETECTOR

Mark E. Allard, BS

1st Lieutenant, USAF

Approved:

James A. Fellows, Lt Col, USAF (Chairman) — 6 MAR 07 — Date

LaVern A. Starman, Maj, USAF (Member) — 6 Mar 07 — Date

Michael A. Marciniak, PhD (Member) — 6 Mar 07 — Date

Abstract

AFRL/MLPJE had developed a novel thermal sensing material termed protein-impregnated-polymer (PIP). Thus far, a proof-of-concept has been demonstrated using a macro-sized pixel (0.64 mm^2) as a bolometric detector. In an effort to better characterize this novel thermal sensing material, experimental data was used to determine figures of merit (FOMs) comparative to off-the-shelf thermal detectors. Microelectromechanical (MEMS) pixels were designed and used as the support structure for an inkjet-deposited droplet of the PIP. During the material characterization, two observations were made: PIP is a pyroelectric material, and the polymer (polyvinyl alcohol (PVA)) without the protein was found to be more suited for measurements taken on the micro-scaled pixels. Both PVA and PVA doped with carbon black (PVA_CB) were the materials focused on in this research, with the latter being the material used for FOM characterization. Pyroelectric coefficients for PVA and PVA_CB were found to be 755.11 nC/(cm^2 K), and 108.32 nC/(cm^2 K), respectively, which are both two orders of magnitude higher than values for current pyroelectric polymers. A responsivity of 1.66×10^4 V/W, thermal time constant of 3.59 sec, noise equivalent power of 21.3 nW, and a detectivity of 1.93×10^5 $cm\sqrt{Hz}/W$ were the FOMs found in this thesis. Although the calculated FOMs are not stellar in comparison to current thermal detector technology, this material shows much promise. The shortfalls in FOMs could potentially be attributed to a poor pixel design. This thesis plants the scientific seed in cultivating a thermal imaging focal plane array (FPA) using a newly found pyroelectric polymer.

Acknowledgments

Before revealing the scientific research that was discovered in this thesis, I would like to recognize some very important people who have impacted my life both personally and professionally.

My wonderful wife and daughter deserve the utmost thanks for all of the lonely hours they spent waiting for me to come home from school; for those sleepless late nights I spent finishing assignments; for the many weekends I was not there for family time. I want to thank my wife for all of the lunches and dinners that were prepared, for the warm welcomes home; for listening to me vent. More than that, I would like to thank her for her encouragement and unconditional love. I would like to thank my daughter for her understanding in the value of education when I was not available to go to the pool or play Barbie and for her pre-bedtime calls, that gave me motivation to succeed.

My dad and mom deserve my gratitude for their loving support. To always doing more than needed and expecting nothing in return. Special loving thanks to my father who was diagnosed with cancer at the beginning of my assignment at AFIT. His struggles and perseverance solidified the fact that he's my hero and is what gave me the strength to give 110 %. To mom, who is the most multitasking mother on this earth; for her continued nurture and love.

Special thanks to my advisor, Lt Col James Fellows, for his constant encouragement and unparalleled logic. To Dr. Michael Marciniak for his clear guidance and IR expertise; to Major LaVern Starman for his MEMS expertise.

Dr. Rajesh Naik, Dr. Larry Brott, and Kristi Singh from AFRL/MLPJE are to be thanked for their financial support, equipment use, and fulfilling every request. A special thanks to Dr. Brott for his scientific mentoring and unrivaled craftiness. It was an absolute pleasure to work with all of you.

I am also grateful to my classmates Nate, Matthew, James, and Karl. It has been quite the experience solving what seemed to be impossible homework problems. I wish each of you the best of luck in your AF careers.

Mark E. Allard

.

Table of Contents

Page

List of Figures

Page

Page

Page

Page

Page

Page

Page

Page

List of Tables

Page

CHARACTERIZATION OF POLYMER-BASED MEMS PYROELECTRIC INFRARED DETECTOR

I. Introduction

Nature offers a great model for imitating, learning, and providing inspiration for new and emerging technologies. Nature is continually evolving to meet the needs of ever changing environments by finding solutions that work. "Through evolution nature has experimented with various solutions to challenges and has improved upon successful solutions" [1].

For the past several years, the Air Force Research Laboratory (AFRL) has been developing sensors capable of detecting electromagnetic (EM) radiation across the spectrum—from the infrared (IR), through the visible, and into the ultraviolet regimes. These sensors have become integral parts of military weapons systems, as well as intelligence, surveillance, and reconnaissance systems—and, in general, the capabilities developed are technologically sophisticated [2]. Detecting electromagnetic radiation is of specific interest in aviation because of the increased distances over which sensors need to operate. "The ability to detect such radiation in the IR without cryogenics—the science of low-temperature phenomena—has been an important technology driver because of increased sensor reliability and reduced payloads" [2]. AFRL's developmental research has found that many biological systems possess sensing capabilities unmatched by current technologies.

Recently, the military has been trying to emulate some of nature's IR sensing capabilities. "Biomimetics means to imitate life, and in a more practical sense, it is an

interdisciplinary effort aimed at understanding biological principles and applying them to improve existing technology" [2]. Three of nature's creatures that have been studied in detail in an effort to find the optimal IR detection system to emulate are the jewel beetle (Melanophilia acuminata), the pit viper, and bacterial proteins. The goal is to find the single biological "trigger" that is responsible for initial stimulus for IR detection.

The jewel beetle lays its eggs in the bark of freshly burned trees using the ability to detect forest fires from a distance of about 80 km [3]. The forest fires emit IR radiation that the beetle detects via a specialized IR sensor known as the IR pit organ or IR sensilla. Throughout the research of this creature, it was found that the sensilla is located on the abdomen of the insect and uses similar properties to that of a golay cell. The golay cell senses temperature by absorbing radiation in a gas chamber, heating the gas, causing it to expand and deflect a diaphragm in accordance with the amount of radiation [4]. Since this natural version of the golay cell is not very robust and is extremely complex, the evaluation of biomimetically modeling this creature by AFRL ceased.

The next IR-capable creature that was studied by AFRL was the pit viper. Pit vipers are named after their specialized thermo receptors, heat-sensitive organs located on either side of the head that look like small pits. These pits contain membranes sensitive to IR radiation and allow the snakes to locate their prey based on temperature differences with their environment. To the pit viper, rodents and birds that are only fractions warmer than the background stand out even in complete darkness [5]. These nocturnal creatures have been found to detect changes in temperature as small as 0.002 to 0.003 °C [6].

Further research, again by AFRL, proved this creature too complex to continue the study. The snake's IR detection system is only engaged when close to its prey. Also, it was found that the snake uses its blood to cool its sensors; remembering the original objective is to find the single biological "trigger."

The last avenue researchers at AFRL looked into was bacterial proteins. Certain proteins undergo substantial conformational changes in response to a given stimulus. "This conformational change can manifest in different manners and result in an actuation, that is, catalytic or signaling event, movement, interaction with other proteins, and so on" [7]. In all cases, the sensing-actuation process of proteins is initiated by a recognition event that translates into a mechanical action [7]. By harnessing this mechanical action, a thermal transducer can be envisioned.

Using the bacterial protein approach in creating an IR sensor has been Air Force Research Lab, Materials Lab, Experimental branch's (AFRL/MLPJE) objective over the last couple years. Finally, in 2001, the first biological IR sensing material was found. AFRL/MLPJE has developed a biological thermal sensing agent from the TlpA protein of *salmonella*. The TlpA protein uses its coiled-coil motif response that changes by expanding and contracting when exposed to varying temperatures [8]. To exploit this behavior, the TlpA is suspended in a mixture of poly vinyl alcohol (PVA) and carbon black. The PVA is used to provide flexible structural support, giving the protein the freedom to expand and contract. The carbon black particles improve the material's electrical properties and its IR absorbtivity. The resulting composite thermal sensing material is termed protein-impregnated-polymer (PIP) [8].

1.1 IR Detectors

"Although optical-sensor systems traditionally have been modeled after the human eye, recent research indicates that modalities other than image forming systems can be used to detect, identify, and monitor targets of interest" [9]. The sensors that are used to detect optical radiation fall into two categories: photodetectors and thermal detectors.

Photodetectors are devices or materials that detect light by direct interaction of the radiation with the atomic lattice of the material. Photodetectors are made from semiconductor materials and need to be cryogenically cooled to function as an IR detector which increases both the cost and payload of the detector system. In short, when photons are incident on a photodetector, electrons from the valence band are excited into the conduction band creating an electron-hole pair. This electron excitation is detected by associated circuitry or interfaces. There are three main types of photodetectors: photoconductive,, photovoltaic, and photoemissive. Due to the detection process, this regime of detectors typically has a fast response time, on the order of micro-seconds.

Thermal detectors respond to the absorbed energy of the optical radiation by changing the temperature of the sensor [9]. This is typically a two-step process: 1) the radiation must change the temperature of the active region in the sensor, and 2) this temperature change causes or induces some measurable parameter change. Once again, this parameter change is measured with associated circuitry or interfaces. Because the measurable parameter change in thermal detectors is due to heat, the response time will

be much slower. Some examples of thermal detectors and their mechanism are listed in Table 1.

Table 1: Thermal detectors and their respective material/measured parameter changes.

Type of Thermal Detector	Material Parameter	Measured Parameter
Bolometer	Resistance	Voltage or Current
Pyroelectric	Spontaneous polarization	Current
Thermocouple	Thermal potential difference	Voltage
Microcantilevers	Mechanical displacement	Mechanical displacement

For most of the aforementioned thermal detectors, no cooling system is required, and they can be operated at room temperature. The development of uncooled IR detectors capable of imaging scenes at 300 K has been an outstanding technical achievement. Much of the technology was developed under classified military contracts in the United States, so the public release of this information in 1992 surprised many in the worldwide IR community [10]. The benefits of uncooled thermal detectors in military applications are boundless. Although the response time is slower than its counterpart, the photodetector, less equipment to operate and minimal cost to fabricate are two of the major thrusts in continued research in uncooled IR detectors.

Since the invention of IR detectors, a means to compare and contrast between all the different detectors was needed. Figures of merit (FOMs) make this possible. FOMs enable the user to compare relative performance between detectors [9]. In order to analyze, quantify, and compare the performance of IR imaging devices, such as various types of focal plane arrays (FPAs), it is essential to have an in-depth understanding of their FOMs [11].

PIP has not been precisely classified into a particular type of thermal sensing material. Thus far, what is known is that PIP has been proven to detect thermal radiation. Manufacturing of this material can be done at low cost and has potential to be comparable to current thermal detection devices that exist on today's market.

1.2 Proof-of-Concept

Initially, when AFRL/MLPJE started their research with PIP, the material was thought to be bolometric, which when tested required a bias voltage. Their results showed that the TlpA protein both enhanced the recovery time after a thermal stimulus and mitigated noise in the signal [1]. From these experimental results, the protein was incorporated into the PVA/carbon black solution to make the PIP material. The experimental results collected by MLPJE are shown in Figure 1. For this experiment, all samples incorporated PVA, carbon black, and glycerol. The control sample consisted of only PVA and carbon black; the collagen sample included PVA, carbon black, and a collagen protein; the TlpA sample incorporated PVA, carbon black, and a TlpA protein. It is evident from these results that the TlpA sample both mitigated inherent noise in the response and also showed a faster response time when the sample was masked from the thermal source. The results of this experiment concluded that the TlpA protein should be included in the PVA-carbon black formulation, thereby developing a biomimetic thermal sensing material, termed PIP.

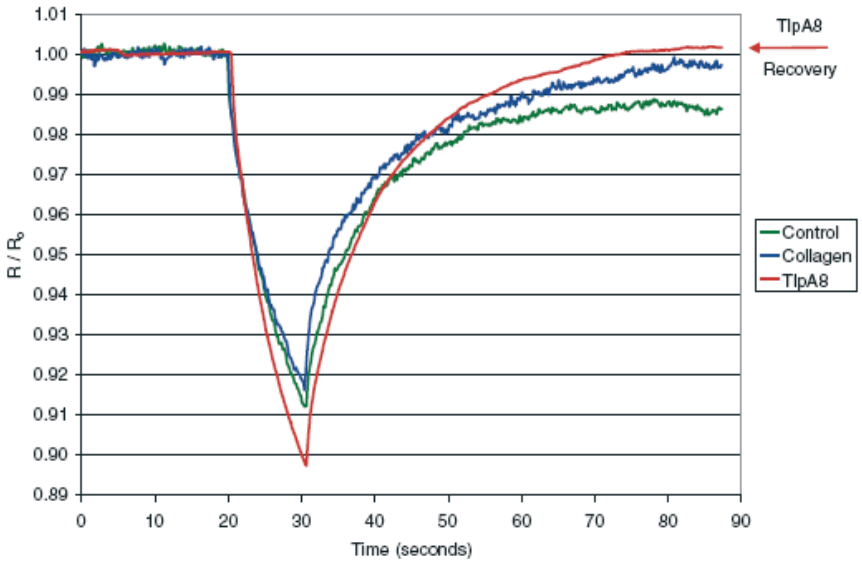

Figure 1: Experimental results collected by AFRL/MLPJE to determine the benefit of the TlpA protein. All of the materials under test in this experiment consisted of PVA and carbon black. The control sample only had PVA and carbon black, the collegen incorporated PVA, carbon black, and a collegen protein, and the TlpA8 consisted of PVA, carbon black, and the TlpA protein [1].

Thus far, AFRL researchers have successfully built a detection array using a PIP-based thermal detector, making the first ever biomimetic thermal detector [2]. A thin film of the PIP was deposited onto a circuit board pre-fabricated with 64 anodes and 64 cathodes making a total of 64 pixels. The film was evenly distributed across the circuit board with a draw-down bar creating a film thickness of ~250 μm. In an effort to individualize each of the pixels, a micromachining technique was invoked using a UV laser. Linewidths of 15 μm were made with minimal damage to the underlying substrate. The completed 8 x 8 array (625 mm^2) is shown in Figure 2.

The chips were tested under ambient temperature and pressure with the thermal signal being focused onto the chip using a germanium lens [8]. In an effort to monitor the output signal of the device, the pixel was biased while simultaneously measuring

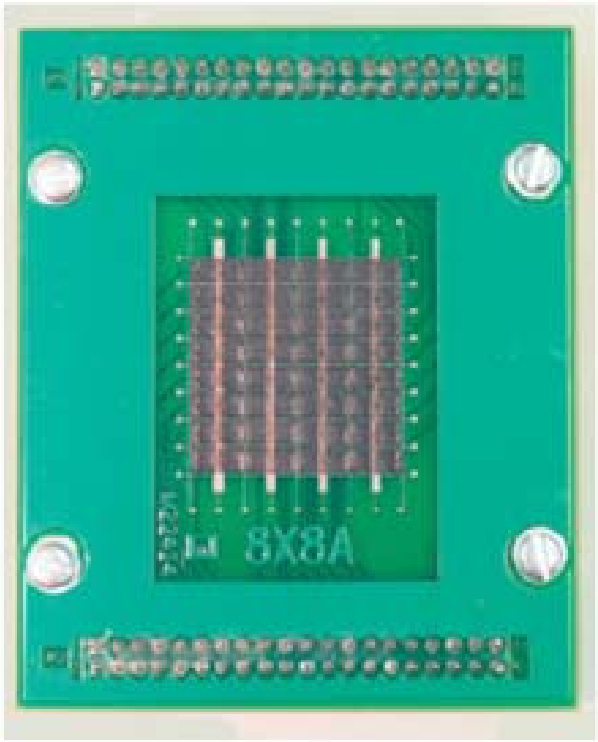

Figure 2: An image of the world's first biomimetic thermal imager [8].

resistance. The incident thermal radiation induces a change in resistance, thereby demonstrating the PIP material as a bolometric type thermal detector. In thermal detectors, the response time is directly proportional to the thermal mass of the pixel. Therefore, the pixel array shown in Figure 2 is less than ideal in producing an effective image because the size of the pixel (800 μm x 800 μm) is much larger than the typical size of current thermal IR detector pixels of 50 μm x 50 μm. Most bolometer designs allow the active thermal sensing material to be elevated off the substrate, both maximizing the sensitivity of the sensor and minimizing the thermal time constant. The design shown in Figure 2 was created by depositing PIP between two electrodes while the material is adhered to the underlying circuit board with no thermal isolation whatsoever.

Also, the deposition methods of current thermal device's active materials have allowed for thicknesses of less than 500 nm, whereas in the pixels shown in Figure 2 have a thickness of 250 μm.

1.3 Statement of Problem

The need to move from the macro-scale to a micro-scale PIP focal plane array is critical. By reducing the thermal mass, the response time will be greatly reduced, thereby enhancing the possibility of a fully functioning biological thermal imaging focal plane array. In an effort to minimize the thermal mass, both a micron-scaled structure and a PIP deposition method need to be developed. The objective of this aim is to enhance the PIP-based IR detector FOMs closer to current off-the-shelf IR thermal detectors.

Descriptions of the detector's structural design characteristics that will result in testing for FOMs are

1) Thermal isolation from the underlying substrate,
2) Dimensions large enough (~ 400 μm x 400 μm) for an unproven ink jet micro-deposition method (able to compensate for movement errors in x and y),
3) Interdigitized electrode fingers allowing the deposited PIP to complete the circuit,
4) The ability to electrically interact with each pixel.

Once the PIP material is deposited, the pixel will then be placed into a radiometric set-up in an effort to collect data from which to calculate IR detector FOMs to be compared with off-the-shelf thermal detectors.

1.4 The Proposed Solution

This thesis will be dedicated to design a functioning thermal detector prototype by applying the PIP material to the top of a polysilicon micro-electro-mechanical-system (MEMS) structure. The PIP material, when deposited, must have thermal isolation from the underlying substrate in an effort to minimize the thermal time constant. The ultimate goal of this thesis is to prove that a micron-scale biomimetics-based thermal sensor using the PIP material will have comparable FOMs to existing commercial thermal IR detectors.

1.5 The Approach

The detector's structure will be created using the poly-crystalline silicon surface micro-machining technique. The MEMS structures will act as the isolating structure and also provide electrical contacts for biasing and transduction measurements. The designs are created in a CAD-based program called L-edit. Once created, the designs are submitted to MEMSCAP to be fabricated using the Polysilicon Mulit-User MEMS Processes (PolyMUMPS).

The PIP deposition techniques will consist of an ink jet deposition method using MicroFab's MJ-AT Jetting Device. The smallest amount of PIP possible will need to be deposited onto the pixel while remaining thermally isolated from the underlying substrate. Also, the PIP material needs to complete the circuit between the interdigitized fingers of the MEMS structure to allow for electrical current to pass through the material. The main objective of this thesis is not to optimize the deposition method for a high yield rate; therefore, any necessary means to get the PIP material onto a pixel will be used.

The FOMs for IR detectors are responsivity, thermal time constant, noise equivalent power (NEP), and detectivity. The responsivity and detectivity of a thermal detector are measures of sensitivity of the electrical output signal to incident thermal flux. The NEP is a parameter that defines the radiant power incident on the detector that produces an output signal equal to the root mean square (rms) detector noise. The normalized detectivity, commonly known as D*, is the detector output signal-to-noise ratio (SNR) at 1 Watt of input IR flux normalized to a 1 cm detector area and 1 Hz bandwidth. These qualitative measures will be used to judge the performance characteristics of the fabricated PIP based pixels and be compared to current thermal detectors.

1.6 Scope

This thesis will demonstrate that the PIP material can be used to make a functioning micron-scaled thermal detector. Thus, this research will only concentrate on the following topics: building pixels using the PolyMUMPs foundry, micro-deposition of the PIP material, characterizing the PIP-based detector in a radiometric set-up that will result in testing for FOMs, and comparing these FOMs to commercial off-the-shelf thermal detectors.

1.7 Contributions

The research performed in this thesis will establish a baseline for the first-ever micron-scale biologically-based-IR thermal detector. Once the micron-scaled PIP-based detector proof-of-concept is demonstrated, more research into optimizing and mass

producing FPAs of these pixels is recommended. The visionary application of a PIP FPA is for IR detection/imaging on a micro-unmanned aerial vehicle (μUAV).

1.8 Thesis Overview

Chapter 2, titled "Background," will be devoted to understanding thermal detectors. A more detailed description will then be dedicated to pyroelectric detectors, which is what the PIP material was revealed to be. Chapter 3, titled "Material Characterization and Sample Preparation," will describe the electrical characterization that was accomplished to determine that PIP is a pyroelectric detection material. Also, in an effort to describe how the sample was prepared for FOM characterization, a description of MEMS pixels and the inkjet deposition system will be addressed. Chapter 4, titled "Figure of Merit Analysis," will describe how all of the FOMs will be experimentally and/or analytically found. In Chapter 5, titled, "Results and Analysis," a complete discussion on the results found for the FOMs will be described along with an analysis on some of the performance trends of the PIP detector. Also, the FOM results found in this thesis will then be compared to other thermal detectors to establish a performance baseline. In Chapter 6, titled "Conclusions and Recommendations," the scientific contributions from this thesis will be described and any future work that would be valuable to follow-on.

1.9 Works Cited

[1] Bar-Cohen, Yoseph. *Biomimetics, Biologically Inspired Technologies.* Florida: CRC Press, 2006.

[2] Stone, Morley, O. "Electromagnetic applications of biomimetic research," *Air & Space Power Journal*, Spring 2004, http://www.findarticles.com/p/articles/mi_m0NXL/is_1_18/ai_n6120608.

[3] Dalziel, Louise. "Jewel beetle flies into the inferno." http://news.bbc.co.uk/2/hi/science/nature/4362589.stm

[4] Keyword "Golay Cells," http://www.answers.com

[5] Keyword "Pit viper," http://www.wikipedia.com

[6] Hearn, Kelly. "Snake proteins may make good sensors." http://www.globalsecurity.org/org/news/2001/010228-ir.htm

[7] Ehrick, Jason,D., Deo, Sapna, K., "Genetically engineered protein in hydrogels tailors stimuli-responsive characteristics." *Nature*, vol 4, pp 298 – 302, Apr 2005.

[8] Brott, Lawrence L., Rozenzhak, Sophie, M., "A Poly (vinyl alcohol) / Carbon-Black Composite Film: A Platform for Biological Macromolecule Incorporation." *Advanced Materials*, vol 16, pp 592 – 596, Apr 2004.

[9] Dereniak, E.L., Boreman, G.D. *Infrared Detectors and Systems*. New York: John Wiley & Sons, Inc., 1996.

[10] Kruse, Paul, W., Skatrud, David, D., *Uncooled Infrared Imaging Arrays and Systems.* Boston, MA: Academic Press, 1997.

[11] Datskos, Panos, G., Lavrik, Nickolay, V., "Detectors –Figures of Merit." *Encyclopedia of Optical Engineering*, pp 349 – 357, 2003.

[12] Kaieda, Tetsuo. *Protein Impregnated Polymer (PIP) Film Infrared Sensor Using Suspended Microelectromechanical systems (MEMS) Pixels.* MS Thesis. AFIT/GE/ENG/05-10. School of Engineering and Management, Air Force Institute of Tehcnology (AU), Wright Patterson AFB, OH, September 2005.

II. Background

2.1 Chapter Overview

The purpose of this chapter is to give background information on the topics that are applicable to this thesis. These topics of discussion will essentially construct the foundation of why and how this thesis will benefit the IR community. The realization of the outcome of this thesis research will result in an unprecedented breakthrough in sensor technology. In this chapter, the following topics will be discussed: IR fundamentals, the basics of thermal detection, thermal detectors, and lastly, a detailed discussion of pyroelectric detectors.

2.2 IR Fundamentals

In 1900, Max Planck developed the law of blackbody radiation which predicted the spectral exitance of electromagnetic radiation at all wavelengths from a blackbody at a temperature, T [1]. The analytical solution that Planck derived matched the empirical data at all wavelengths and can be seen in Equation (1):

$$M_e(\lambda,T)=\frac{2\pi hc^2}{\lambda^5\left(e^{\frac{hc}{\lambda kT}}-1\right)}\left[\frac{W}{cm^2\mu m}\right], \tag{1}$$

where, $M_e(\lambda,T)$ is the spectral radiant exitance, h is Planck's constant $\left(6.626\times10^{-34}\left[J\cdot sec\right]\right)$, c is the speed of light $\left(2.998\times10^{8}\left[m/sec\right]\right)$, λ is wavelength [μm], k is the Boltzmann constant $\left(1.381\times10^{-23}\left[J/K\right]\right)$, and T is temperature $\left[K\right]$. This development proved that most living bodies emit radiation that is concentrated in the IR

spectrum and that such heated bodies emit their radiation in a continuum of wavelengths [2]. Figure 3 depicts plots of the spectral exitance for temperatures at 300 K, 400 K, and 500 K.

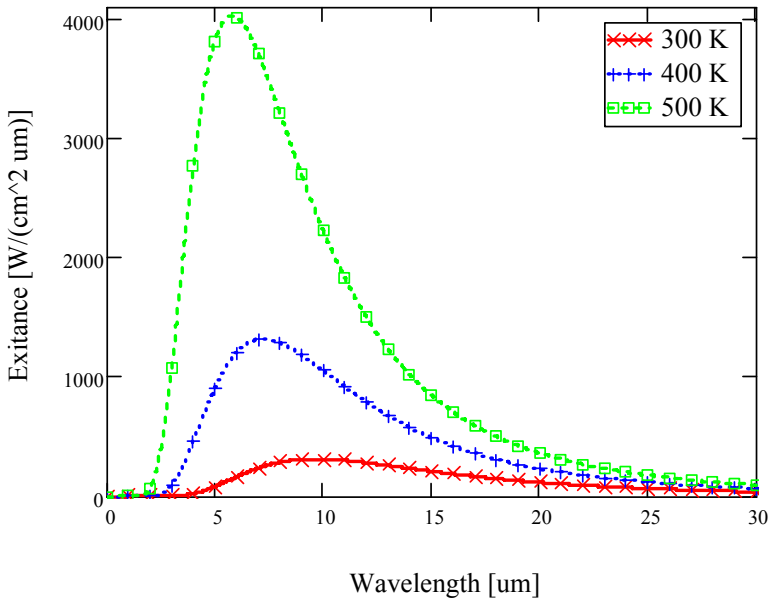

Figure 3: Plot of the spectral radiant exitance for 300 K, 400 K, & 500 K blackbodies.

The peak wavelength of the radiated signal for a specific temperature can be quantified using the equation defined from Wien's displacement law. This law states the hotter the object is, the shorter the wavelength at which the peak of its radiation is emitted [3]. By setting the partial derivative of the spectral exitance equal to zero,

$$\frac{\partial M_e(\lambda,T)}{\partial \lambda} = 0\,, \tag{2}$$

and solving for the wavelength, the peak wavelength at which the exitance is maximum for a particular blackbody temperature, can then be solved

$$\lambda_{max} = \frac{2898\,\mu m\,K}{T}. \tag{3}$$

Figure 4 depicts Wien's displacement law using various blackbody source temperatures.

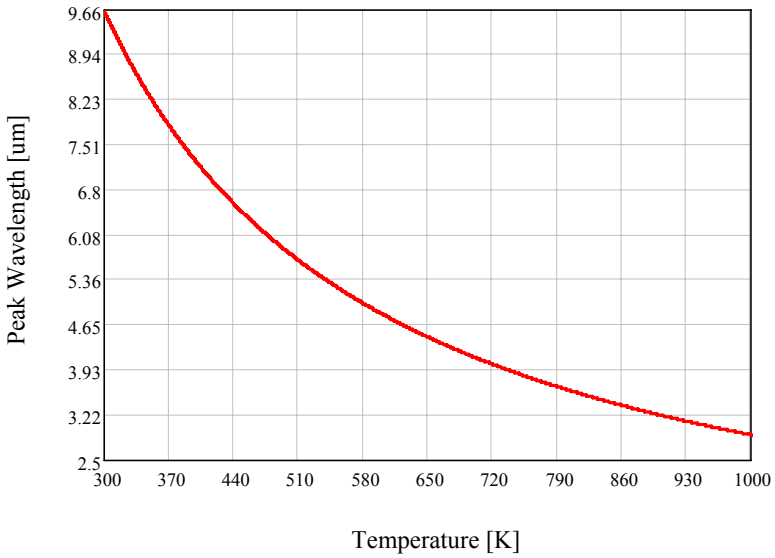

Figure 4: Peak wavelength at maximum exitance for various blackbody temperatures.

The understanding of atmospheric attenuation is crucial when designing an IR detection system. All IR applications require EM radiation transmission through air. As the object emits this radiation in the IR, molecules that comprise the air will both scatter and absorb this radiation, ultimately attenuating the EM signal to be detected. Larger particles, such as aerosols, easily absorb the EM radiation, making the IR detection very difficult. However, particles such as smoke and mist are usually small with respect to IR wavelengths, allowing the radiation to propagate much further in this type of austere environment [4]. Figure 5 illustrates a plot of the transmittance through 6000 ft of air at sea level as a function of wavelength. This plot demonstrates the effects of the various constituents that make up the earth's atmosphere. Also, it is evident the two IR operating

regimes are 3 – 5 μm and 8 – 14 μm. In these windows, the effects of atmospheric attenuation are minimal and targets in the IR are most easily detected.

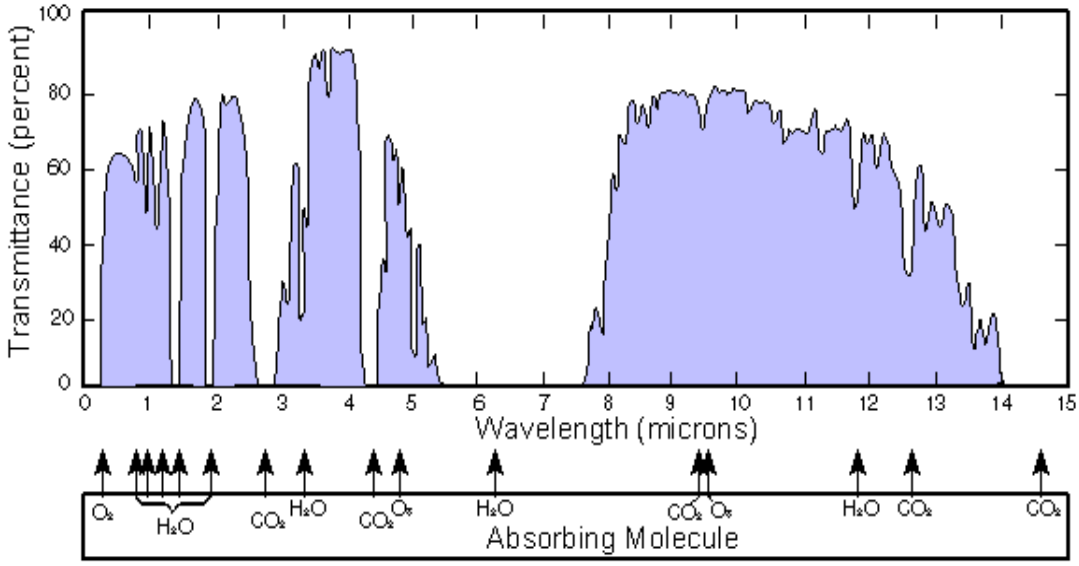

Figure 5: Transmittance of IR radiation through 6000 ft of air at sea level [5**].**

2.3 Basics of Thermal Detection

As described in the introduction, there are two main types of IR detectors, photodetectors and thermal detectors. Although both detectors have their own particular advantages and disadvantages, the focus of this thesis will be on using the PIP material as a viable thermal sensing material. Therefore, this section and the rest of this thesis will be dedicated to becoming intimately familiar with the physics and properties of thermal detectors.

Thermal detectors respond to incident radiation by raising the temperature of the active layer. The increase in temperature in turn causes a physical property to change in the thermal sensing material. These classes of detectors are termed "energy devices" due

to the fact that the amount of energy absorbed is determined by the absorption properties of the detector's material [2]. In an effort to describe the performance of thermal detectors, it is best to separate the discussion into two sections: the thermal characteristics (temperature rise due to incident thermal radiation) and the physical change in the material (the measurable response in the material when exposed to incident thermal radiation).

The most basic thermal detector model can be seen in Figure 6. This model's components consist of the active element's heat capacitance C_{th}, at a temperature of $T+\Delta T$, where T is the temperature of the underlying substrate, which is an infinite heat sink. ΔT is the change in temperature when exposed to incident IR radiation. The suspended structure is linked to the substrate via some thermal conductance, G_{th}. At thermal equilibrium, the structure will be at temperature, T.

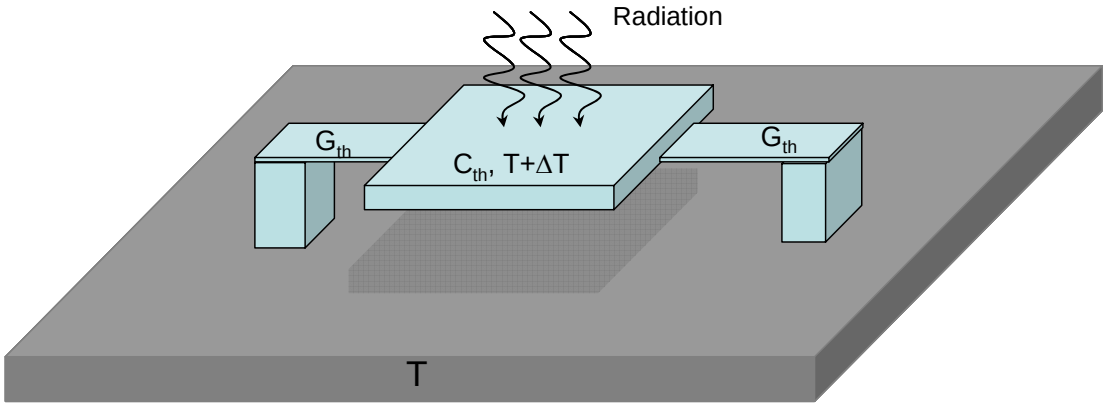

Figure 6: The fundamental representation of a thermal detector.

When IR radiation is detected, the active element will change to a temperature of $T+\Delta T$. This change in temperature can be found by solving the heat balance equation,

$$C_{th}\frac{d\Delta T}{dt}+G_{th}\Delta T=\varepsilon\Phi_e. \quad (4)$$

Emissivity, ε, of the material is the ratio of energy radiated by the material to energy radiated by a blackbody at that same temperature [6]. By Kirchoff's law, this also means emissivity is a measure of the material's ability to absorb IR radiation. The incident thermal flux, Φ_e, is radiation that changes the detector's temperature from T to $T+\Delta T$. If the assumption is made that incident thermal flux is a periodic function, then

$$\Phi_e=\Phi_0 e^{j\omega t} \quad (5)$$

where, Φ_0 is the amplitude of the incident sinusoidal flux, and ω is the frequency of the signal. This leads to the solution of the differential heat equation where the change in temperature, ΔT can then be solved. The simplified solution (removing the transient part without losing any generality) can be seen in Equation (6), and is valid for any type of thermal detector [7]

$$\Delta T=\frac{\varepsilon\Phi_0}{\sqrt{G_{th}{}^2+\omega^2 C_{th}{}^2}}. \quad (6)$$

Equation (6), can be mathematically evaluated to determine how to optimize performance. First, it is clearly evident that ΔT needs to be as large as possible. To make this possible, the emissivity of the thermal sensing material needs to be as high as possible. The theoretical limit for ε is one, and this value is typically used when evaluating thermal detectors. Next, to maximize the change in temperature, both the

thermal conductance and the heat capacitance need to be small. The interaction of the thermal detector with the incident radiation needs to be optimized by removing all other thermal contacts with the detector's surroundings. This means the detector mass must be as small as possible, and the connection between the elevated sensing area and the underlying substrate also needs to be as small as possible [7].

This change in temperature, ΔT, can then be further manipulated into a more useful term called responsivity, $\Re_{(v,i)}$. Responsivity, generically, is the electrical output of the detector divided by the incident thermal flux. From Equation (6), it is evident that ΔT and ω are inversely proportional, and therefore, a typical characteristic for thermal detectors, called thermal response time, τ_{th}, can then be found,

$$\tau_{th} = \frac{C_{th}}{G_{th}}. \tag{7}$$

Also, another variable substitution that will be used is the coefficient, K, which reflects how well the temperature change transduces into an electrical output voltage or current of the detector [7],

$$K_{(v,i)} = \frac{\Delta V}{\Delta T} \text{ or } \frac{\Delta I}{\Delta T} \tag{8}$$

Solving for ΔV or ΔI in Equation (8), and inserting both Equation (7) and (8) into Equation (6), the voltage responsivity , $\Re_v = \frac{\Delta V}{\Phi_0}$, or the current responsivity, $\Re_i = \frac{\Delta I}{\Phi_0}$ can be solved,

$$\Re_{(v,i)} = \frac{K_{(v,i)}\varepsilon}{G_{th}\sqrt{1+\omega^2\tau_{th}^{\ 2}}} \tag{9}$$

A basic understanding of how thermal detectors operate is paramount when trying to design a thermal IR detector. The background mathematical analysis clearly illustrates how to maximize the voltage and current responsivity of a thermal detector. Some of the key elements needed to succeed in this endeavor are the design of the detector's structure that gives the thermal isolation, and designing for as small a thermal conductance as possible. Also, the heat capacitance of the material needs to be minimized to effectively increase the reponsivity of the device. Most often, the heat capacitiy is a material parameter that is designed around or can be controlled by the thickness of the sensing area [16]. Reducing this value also reduces the thermal time constant, which is critical when trying to design FPAsof thermal detectors.

The value, K, in Equation (8) is generic to all thermal detectors. This value, depending on the type of thermal detector, varies due to the physical parameters that change with incident IR radiation. The next section will be dedicated to describing the four main types of the thermal detectors, thermocouples, bolometers, microcantilevers, and lastly, the recently categorized PIP-based sensor, pyroelectric detectors.

2.4 Types of Thermal Detectors

First, the four different types of thermal detectors shown in Table 1 will be described. Again, these four types of detectors are thermocouples/thermopiles, bolometers, microcantilevers, and lastly, pyroelectrics. All thermal detectors rely on the absorption of IR energy. This energy heats up the detection element which leads to a change in the physical properties of the detection material and/or detector structure. The

four thermal detectors that will be described here have their own unique physical response to incident IR radiation.

Both thermocouples and thermopiles (thermocouples connected in series) use the thermoelectric effect to sense thermal gradients (temperature difference between two points). These devices are formed by joining two dissimilar metals. Essentially, the thermoelectric effect states that when two different metals are subject to a temperature gradient, a voltage will be produced. In most cases, the "cold" junction is maintained at a known temperature while the "hot" junction is attached to a probe and exposed to the targeted object [8]. These devices are very inexpensive and can measure a large range of temperatures. The major constraint of thermocouples is their accuracy. Typically, these detectors cannot measure with < 1 °C accuracy and are less than ideal for thermal imaging.

The bolometer is a resistive element created from a material with a very small thermal capacity and a large temperature coefficient of resistance (TCR) so that absorbed incident radiation produces a large change in resistance. The TCR will be described in more detail in Chapter 3, but essentially when a bolometric-type material is heated or cooled, there will be a change in resistance. This relative resistive change is known as the TCR. The higher the TCR for the material, the more sensitive the bolometer will be. Figure 7 depicts a cross-section of a bolometer detector.

Microcantilever detectors are another class of thermal detectors in which incident IR radiation is absorbed by the micron-scaled cantilever, causing the structure to deflect.

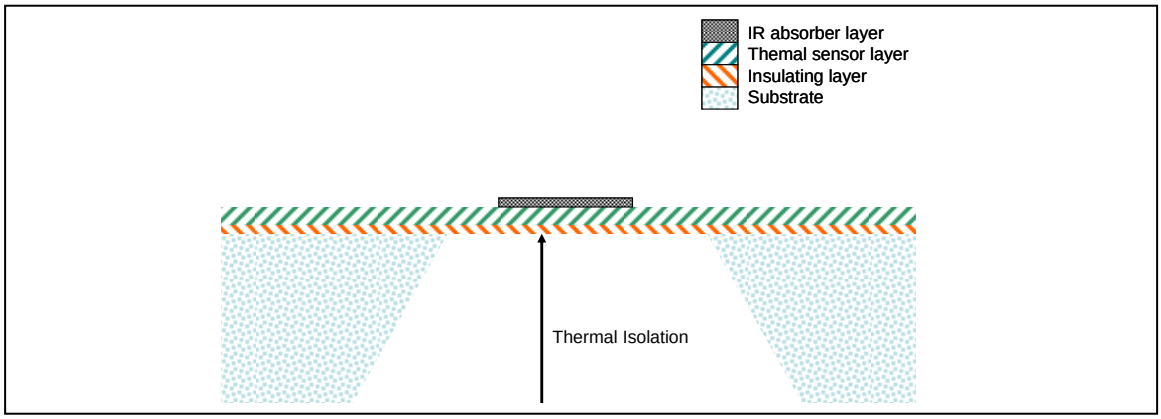

Figure 7: Cross-section of a thin film bolometer detector [7].

This deflection has been reportedly measured by numerous techniques, including optical, capacitive, piezoresistive, and electron tunneling [9]. Microcantilever thermal detector technology is typically designed with MEMS and uses the differences in thermal expansion coefficients of two different bimetals to cause a displacement in the microcantilever [4]. When the structure is released from the sacrificial layer, the bimetal material will tend to displace in the direction of the material with the higher thermal coefficient of expansion. This displacement will give the structure thermal isolation from the underlying substrate. When additional IR photons are absorbed, the cantilever is heated, causing the bimetal material structure to deflect.

A means to measure this deflection of the bimaterial microcantilever device, in response to absorbed IR radiation, is essential for this device to be considered a thermal detector. One approach, known as the "optical" lever, uses a beam of light from a laser source which is focused onto the tip of the cantilever beam. The type of laser must be strategically chosen depending on the type of material in an effort to be completely reflected rather than absorbed by the materials used in the cantilevers. The reflected

beam is focused onto a two-element or four-element photodiode. The outputs detected from the photodiodes are electrically amplified and the difference in signal is measured. The changes in measured signal level correspond to the degree to which the cantilever bends, and therefore, is a function of absorbed IR radiation. Figure 8 illustrates a typical MEMS based cantilever design.

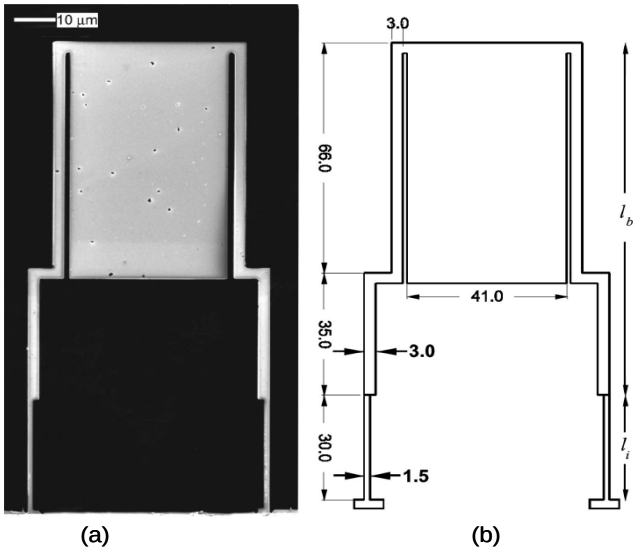

Figure 8: Microcantilever IR detector design. a) SEM image. b) Detector's dimensions in μm [9].

Pyroelectric detectors are another type of thermal detector. Pyroelectric materials are those materials that with a change in temperature create a change in polarization. This polarization change creates a surface charge that is produced in a particular direction as a result of the material's response to the change in spontaneous polarization with respect to temperature [7]. The thermal response is a generation of current when the pyroelectric material's temperature changes. If the temperature does not fluctuate, no

current is produced. This is the most common type of thermal detector in that they are inexpensive and are the most sensitive at room temperature [2].

Pyroelectric materials typically have crystalline asymmetry which possesses an electrical dipole moment without the application of an electric field. Therefore, this device can operate without bias. If the pyroelectric detector's temperature changes at a rate faster than the compensating surface charges can redistribute themselves, an electrical current can be seen. This category of detector is an alternating current type, which means rather than detecting a temperature level, it detects a temperature difference.

It will be shown that the PIP material was found to be pyroelectric, rather than bolometric. Therefore, this thesis will be dedicated to the characterization of a pyroelectric thermal sensing material. In the following section, I will discuss the background, materials overview, FOMs, pyroelectric detector structures, pyroelectric deposition methods, and lastly, some of the required signal conditioning needed for pyroelectric detectors.

2.5 The Pyroelectric Detector

2.5.1 Background

The physically observable phenomenon of pyroelectricity has been around for many centuries, discovered by Theophrastus in 315 BC, where he describes a stone, probably the mineral tourmaline, which could attract wood particles and small straw when heated [10]. Experimental research of static electricity in pyroelectric materials began in the early 18th century. This paved the way to crystal physics toward the end of the 19th century, when the Currie brothers discovered piezoelectricity. Studies done on

Rochelle salt resulted in the discovery of ferroelectricity in 1921. It was not until 1938, that applications of using the pyroelectric properties of tourmaline as an IR sensor were proposed by Yeou Ta. Due to the lack of technology, Ta's vision was not realized until the early 1960s. Since then, new materials, fabrication processes, and electronic circuitry have made pyroelectric detectors the most sensitive uncooled IR detectors on the market [10].

2.5.2 Material Overview

All crystals can be categorized according to their symmetry elements and are categorized into thirty-two crystal classes. Twenty of these thirty-two are known to be non-centrosymmetric (NCS), or acentric, crystal classes, i.e. types of crystals lacking a center of inversion, and can exhibit a variety of technologically important physical properties [12]. These twenty classes are known as piezoelectric crystals. Ten of these twenty piezoelectric crystals, known as pyroelectric, are found to be spontaneously polarized, attributed to having a dipole moment in their unit cell, and exhibit pyroelectricity. Ferroelectric crystals belong to the pyroelectric family of crystals. These crystals can be defined as pyroelectric crystals that have reversible polarization with the application of an electric field [11]. The aforementioned NCS classes are shown in Figure 9.

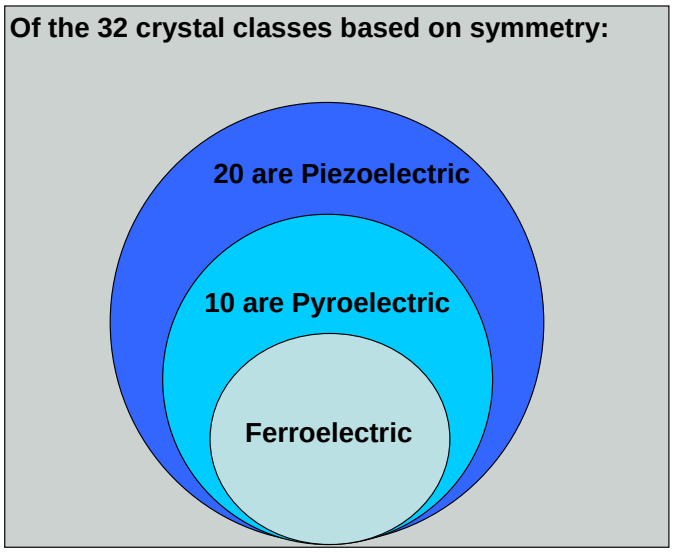

Figure 9: There are 32 total classifications of crystals which are based on symmetry. 20 of these 32, also known as acentric, have piezoelectric properties. Of all the acentric crystals, 10 are classified as pyroelectric, and some of the crystals that exhibit the pyroelectric effect also possess ferroelectric properties [11].

2.5.2.1 Piezoelectric Materials

Piezoelectricity is a term derived from the Greeks, piezen, meaning to press, and was discovered by Jacques and Pierre Curie in 1880. The Currie brothers observed that certain crystals exhibited an electrical current when subjected to a mechanical force. Also, it was found that the converse effect occurred when the crystal was exposed to an electric field; the crystal exhibited a macroscopic strain. Thus, with piezoelectric materials, two effects are possible, direct and converse. The direct effect acts like a generator where the piezoelectric material converts mechanical into electrical energy. Some applications of the direct effect are solid state batteries, sensing devices, and fuel lighting. The converse effect results in a motor action in which the piezoelectric material converts electrical into mechanical energy. The applications of the converse effect can be

seen in micro-motors, both acoustic and ultrasonic sensors, and in electromechanical transducers [12].

2.5.2.2 Pyroelectric Materials

A subclass of piezoelectric crystals is pyroelectric. The term, pyro, comes from the Greek meaning fire. Red tourmaline was discovered to hold electric properties when ash particles were attracted and repelled by pieces in a fire. Pyroelectric materials are inherently polarized even in the absence of an applied electric field. This inherent polarization is termed spontaneous polarization and an illustration of this spontaneous polarization is shown in Figure 10.

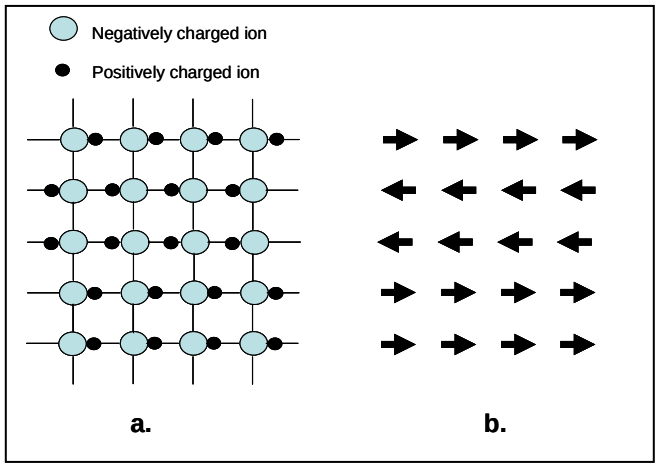

Figure 10: A simplistic model representing a two-dimensional pyroelectric crystal illustrating spontaneous polarization. a) The 2-D crystal lattice. b) The corresponding polarized vector field. Notice the net polarization of the field is oriented in one direction; giving the crystal a dipole moment [11].

As indicated from Figure 9, the larger circles represent negatively charged ions, and are located at the intersection of the lattice points. The smaller circles represent the positively charged ion. This crystal is seen to be spontaneously polarized because the net

polarization of the crystal is oriented in one direction. The spontaneous polarization is measured in terms of dipole moment per unit volume. The crystals that possess this effect are pyroelectric and the direction of the spontaneous polarization is called the polar axis. In the case of the oversimplified crystal structure shown in Figure 10, the polar axis would be from negative to positive [11].

The pyroelectric effect is defined as the generation of pyroelectricity when a pyroelectric material is subject to a thermal stimulus. When there is a temperature change, the crystal becomes electrically polarized. The net polarization is the dipole moment per unit volume, which is proportional to the surface charge per unit volume. When a pyroelectric material senses a temperature change, there is a movement of these charges. By definition, charge flow or charge per unit time, is current. Thus, a pyroelectric material produces a current if it senses a change in temperature. The material will continue to produce more and more current, assuming the temperature continues to increase, until the Currie temperature is reached. The Currie temperature, by definition, is the temperature at which the crystal no longer has an electrical dipole moment. Figure 11 illustrates a typical current response of a pyroelectric material with respect to a change in temperature. The temperature at which the current goes to zero is known as the Currie temperature, T_c, of the crystal. The pyroelectric effect is what makes pyroelectric materials ideal candidates for thermal detectors. Some major applications that use pyroelectric detectors are burglar alarms, IR imagers, and measuring of thermal properties of materials [12].

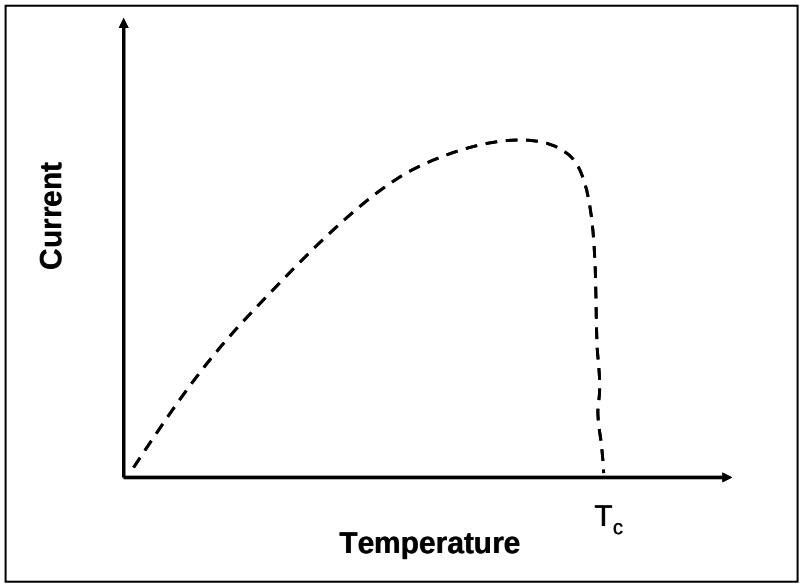

Figure 11: A generic current response, with respect to temperature of a pyroelectric crystal. The temperature at which the current goes to zero is known as the Currie temperature and is specific to each pyroelectric material [2].

2.5.2.3 Ferroelectric Materials

Ferroelectric crystals are a subset of pyroelectric crystals. This type of crystal may be defined as a pyroelectric material that has a reversible or switchable polarization [12]. This polarization can be switched or reversed by the application of an electric field. Therefore, in order for a crystal to have ferroelectric properties, it must possess a permanent dipole moment and be capable of having this dipole moment reversed in the presence of an electric field.

The ferroelectric effect was discovered by J. Valasek in 1921, in an investigation of the anomalous dielectric properties of Rochell salt. In 1935, a second ferroelectric material, KH_2PO_4 was discovered, followed by a third substance, $BaTiO_3$, discovered in 1944. Since then, more than 250 pure materials and many more mixed crystals have been discovered possessing ferroelectric properties [12]. Ferroelectric materials also have

many uses, as they exhibit the properties of both piezoelectric and pyroelectric materials. Devices based simultaneously on switched ferroelectric and piezoelectric properties include, oscillators and filters, while the analogous properties results in light switches, displays, optical memories, and thermal detectors [12].

2.5.2.4 Pyroelectric IR thermal detection materials

Thermal detection materials that capitalize on the pyroelectric effect to transduce the thermal response into an electrical signal can be categorized into three classifications: single crystals, ceramics (polycrystalline), and polymers. Each classification of material has its own unique benefit and disadvantages. This section will describe these three classifications and, in conclusion, illustrate a table depicting pyroelectric detector materials and their applicable parameters, allowing for a visual comparative analysis.

Single crystals like triglycine sulphate (TGS) are extremely attractive materials for pyroelectric detectors because they possess high pyroelectric coefficients, which is a parameter that characterizes how well the material electrically responds to a change in temperature. Equation (8) summarizes a generic change in a detector's electrical output, K, which occurs with a change in temperature in thermal detectors. Focusing on pyroelectric physics, the K value can now be replaced with the pyroelectric coefficient, p, which describes the responsiveness of the pyroelectric material. This parameter is described as,

$$p = \frac{I}{A\frac{dT}{dt}} \tag{10}$$

where I is the current produced by a change in temperature, A is the cross-sectional area normal to the polar axis, and dT/dt is the change in temperature with respect to a change in time (which is essentially the slope of the forced temperature ramp when finding p). Although single crystal materials have a high pyroelectric coefficient, they are difficult to handle and show poor long term stability [7]. Also, these materials have a low Currie temperature which prohibits them from meeting military specifications. TGS is typically used for high performance single pixel detectors. Two other single crystals that have been used for pyroelectric detectors are lithium tantalite ($LiTaO_3$) and strontium barium niobate (SBN).

Ceramic materials are another class of pyroelectic detector materials. There is an ample amount of ceramic materials that consist of solid solutions of PZ (lead zirconate, $PbZrO_3$), and PT (lead titanate, $PbTiO_3$), and other similar oxides. These materials have been developed over many years in an effort to satisfy the requirements of ferroelectric, piezoelectric, electro-optic, and pyroelectric devices. The polar axis can be controlled in these materials by the application of an electric field. Some of the benefits in using ceramics are mechanical and chemical robustness, high Currie temperatures, and that they can be modified by the inclusion of selected dopants to control the pyroelectric coefficient and the Currie temperatures [7].

Polymers can also be used in pyroelectric detectors. Two of the major polymer materials that are used are polyvinylidene fluoride (PVDF) and copolymers PVF_2. These materials possess low pyroelectric coefficients and low dielectric constants. Pyroelectric detectors using polymers typically have FOMs inferior to other types of pyroelectric

materials. Polymer materials are ideal candidates for designing low cost detectors since they are readily available in large thin sheets which do not require expensive lapping and polishing processes necessary for other materials [7].

Ideal pyroelectric materials should have large pyroelectric coefficients, low dielectric constants, low dielectric loss and low volume specific heat. The possibility of finding a material with all of these characteristics is not likely. Typically, a material that has a high pyroelectric coefficient will have a high dielectric constant. Likewise, the polymer type materials which have low pyroelectric coefficients also have low dielectric constants. It is evident that there are a plethora of pyroelectric materials to choose from when designing a pyroelectric detector. Table 2 summarizes some of the current pyroelectric materials and their respective properties.

One of the most important components of any pyroelectric device is the detector material [13]. Table 2 will be a useful resource that will be re-investigated once the PIP

Table 2: Pyroelectric materials and their properties [7].

Material	Material Type	Temp of Measurement (K)	Pyroelectric coefficient, p ($nCcm^{-1}K^{-1}$)	Heat capacity, c_{th} ($Jcm^{-3}K^{-1}$)	Dielectric constant, ε_r	Currie Temperature, T_C (K)
TGS	Crystal	308	55	2.6	55 (1 kHz)	322
DTGS	Crystal	313	55	2.4	43 (1 kHz)	334
TGFB	Crystal	333	70	2.6	50 (1 kHz)	346
ATGSAS	Crystal	298	70	-	32 (1 kHz)	324
$LiTaO_3$	Crystal	298	23	3.2	47	938
SBN-50	Crystal	298	55	2.34	400	394
PGO	Crystal	298	11	2.0	$5x10^{-4}$ (100 Hz)	451
PGP:Ba3	Crystal	298	32	2.0	$1x10^{-3}$ (100 Hz)	343
PZFNTU	Ceramic	298	38	2.5	290 (1 kHz)	503
PCWT-4/24	Ceramic	298	38	2.5	220 (1.5 kHz)	528
PVF_2[26]	Polymer	298	3.2			
PVDF	Polymer	298	2.7	2.43	12 (10Hz)	353

material parameters are defined. In an effort to optimize the performance of a pyroelectic detector, not only do the material properties need to be well understood, but so do the FOMs. The next section will describe the FOMs specific to pyroelectric devices.

2.5.3 Pyroelectric Figures of Merit

In this section, all of the FOMs for pyroelectric detectors will be discussed. FOMs for all IR detectors are a way to do a comparative analysis between all the different detector methodologies. An overview of the FOMs, responsivity ($\Re$), thermal time constant (τ_{th}), noise equivalent power (NEP), and detectivity (D*), for pyroelectric detectors will be discussed in this section.

2.5.3.1 Responsivity ($\Re_i$ and $\Re_v$)

The derivation will begin with the solution to the classical heat balance equation, previously shown in Equation (6),

$$\Delta T = \frac{\varepsilon \Phi_e(t)}{G_{th}\sqrt{1+\omega^2\tau_{th}^{\ 2}}}, \tag{11}$$

where ε is the emissivity, the incident modulated thermal flux is $\Phi_e(t)$, G_{th} is the thermal conductance attaching the raised structure to the infinite heat sink, ω is the modulation frequency, and the thermal time constant is τ_{th}, which is given in Equation (7). Recognizing that $d\Delta T/dt = dT/dt$, and assuming incident sinusoidal radiation, $\Phi_e(t)=\Phi_{e,0}\exp(j\omega t)$, Equation (11) results in,

$$\frac{dT}{dt} = \frac{d\Delta T}{dt} = \frac{\varepsilon j\omega \Phi_e(t)}{G_{th}\sqrt{1+\omega^2\tau_{th}^{\ 2}}}, \tag{12}$$

$$\left|\frac{dT}{dt}\right| = \frac{\varepsilon\omega\Phi_{e,0}}{G_{th}\sqrt{1+\omega^2\tau_{th}{}^2}} \tag{13}$$

By inserting Equation (13) into the rearranged Equation (10), $I = pA_d\frac{dT}{dt}$, the result gives [2]

$$I = \frac{p\varepsilon\omega\Phi_{e,0}A_d}{G_{th}\sqrt{1+\omega^2\tau_{th}{}^2}}. \tag{14}$$

Pyroelectric response due to the change in temperature of the active region is proportional to the pyroelectric coefficient. From a practical perspective, the sensitivity of the detector can be measured in two forms: current responsivity ($\Re_i$) and voltage responsivity ($\Re_v$). Responsivity, by definition, is the output electrical response, whether voltage or current, divided by incident radiant flux. Following this definition, Equation (14) can be divided through by incident radiant flux, $\Phi_{e,0}$, to give a current responsivity equation,

$$\Re_i = \frac{p\omega\varepsilon A_d}{G_{th}\sqrt{1+\omega^2\tau_{th}{}^2}}\left[\frac{A}{W}\right] \tag{15}$$

The current responsivity, $\Re_i$, is the ratio of current flow to the incident radiant flux. The analysis of Equation (15) reveals some interesting facts about pyroelectric detectors. First, when the detector is illuminated with a DC flux, the responsivity will be zero. Since the pyroelectric coefficient, p, is directly proportional to the responsivity, its value must be as high as possible. It is evident that frequency plays an important role in the pyroelectric detectors. A typical responsivity plot vs. modulation frequency can be seen in Figure 12.

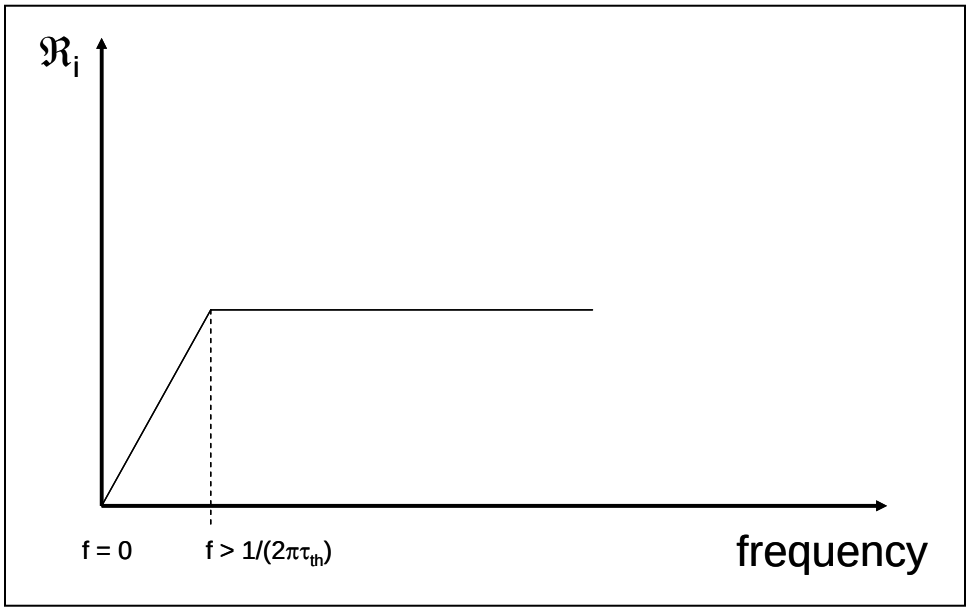

Figure 12: Current responsivity vs. modulation frequency plot [2].

When the pyroelectric detector is illuminated with a DC flux, f = 0 (f = ω/(2π)), there will be no current responsivity, when the chopping frequency reaches a value of f > $1/(2\pi\tau_{th})$, the responsivity will remain constant. Lastly, there is no upper cutoff frequency in the current responsivity. Thus, when the pyroelectric detector is operating at modulation frequencies above $1/(2\pi\tau_{th})$, the current responsivity can be simplified to,

$$\Re_i = \frac{pA_d\varepsilon}{G_{th}}\left[\frac{A}{W}\right] \tag{16}$$

The voltage responsivity, $\Re_v$, is defined as the ratio of voltage generated across the detector to the incident radiant flux. The equivalent circuit for a pyroelectric detector can be seen in Figure 13. This circuit will help in the description of the voltage responsivity.

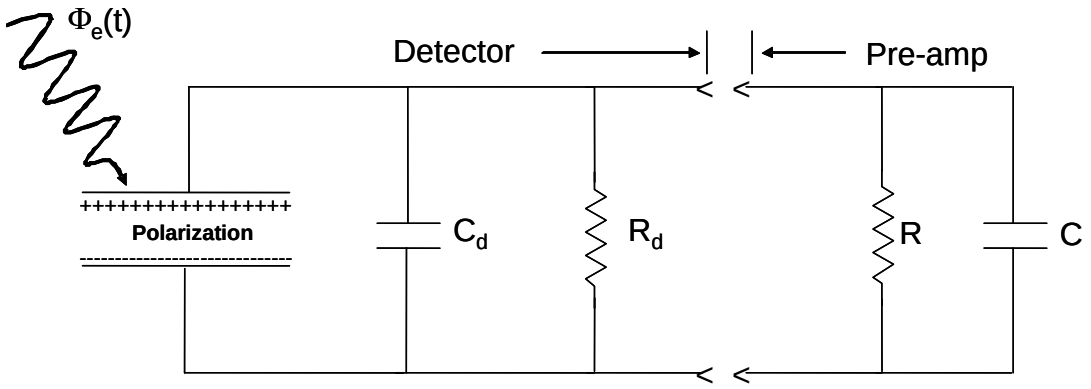

Figure 13: Equivalent circuit for a pyroelectric detector [2].

To calculate the voltage responsivity, the voltage across the detector is required. This detector voltage is the product of the current and the parallel electrical impedance of the detector and the amplifier. This voltage is then,

$$V=\frac{IR_d}{\sqrt{1+\omega^2\tau_e^{\,2}}}, \tag{17}$$

where $\tau_e=R_dC_d$, which is the electrical time constant of the circuit. The voltage responsivity is then given by,

$$\Re_v=\Re_i\left(\frac{V}{I}\right)=\frac{p\omega\varepsilon A_d}{G_{th}\sqrt{1+\omega^2\tau_{th}^{\,2}}}\left(\frac{V}{I}\right) \tag{18}$$

Equation (17) can then be plugged into Equation (18) to give,

$$\Re_v=\frac{p\varepsilon\omega R_dA_d}{G_{th}\left(\sqrt{1+\omega^2\tau_{th}^{\,2}}\sqrt{1+\omega^2\tau_e^{\,2}}\right)}\left[\frac{V}{W}\right] \tag{19}$$

The main difference between Equation (15), for the current responsivity, and Equation (19), for the voltage responsivity, is the fact that there is an upper cutoff frequency. Therefore, the voltage responsivity has three regions of operation. These

three regimes can be seen in Figure 14, which represents the voltage reponsivity with respect to frequency. The first region (1) is where $f < 1/\tau_{th}$, and $\Re_v$ increases linearly with frequency. The second region (2) is where $1/(2\pi\tau_{th}) < f < 1/(2\pi\tau_e)$, and $\Re_v$ is constant with frequency; and the last region (3) is where $f > 1/(2\pi\tau_e)$, and $\Re_v$ falls off linearly with frequency.

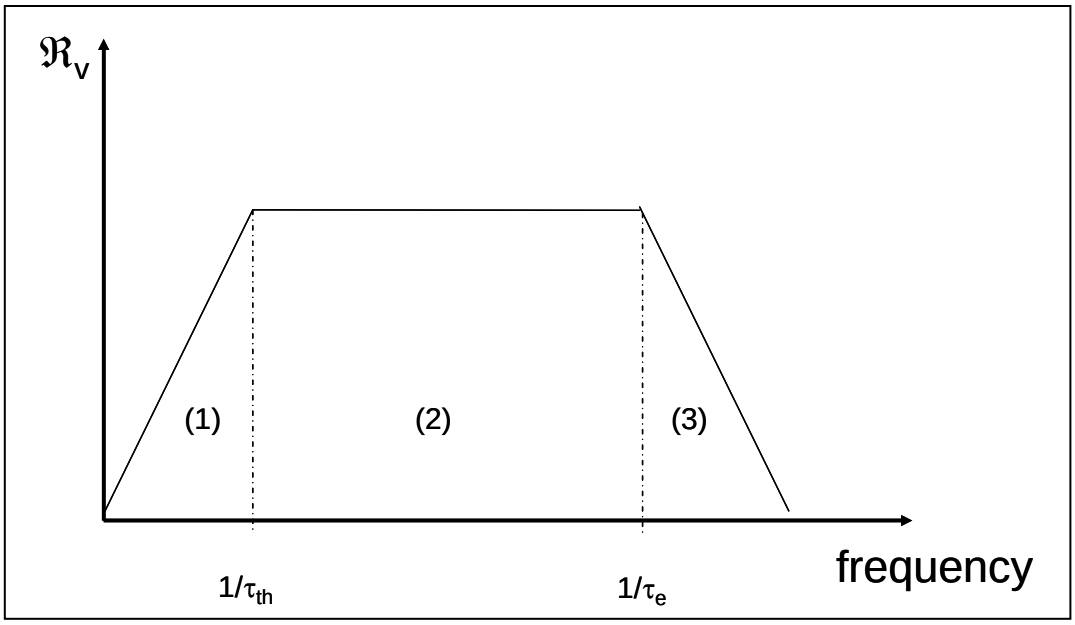

Figure 14: Voltage responsivity vs. frequency for a pyroelectric detector [2].

The responsivity parameter ($\Re_v$) is defined as the output voltage signal of the detector produced in response to a given incident radiant power falling on the detector. Again, responsivity is shown,

$$\Re_v = \frac{V_{out}}{\Phi_e}, \tag{20}$$

Since the voltage output is what was measured, the current responsivity will no longer be discussed. The output voltage was easily measured with an electrometer. However, the

incident power received at the detector requires a detailed discussion of radiometry and will now be discussed.

Typical radiometric calculations begin with the joule radiance,

$$L_e = \frac{\partial^2 \Phi_e}{\cos\theta_s \partial A_s \partial \Omega} \left[\frac{W}{cm^2 \, sr \, \mu m} \right] \tag{21}$$

where Φ_e is the joule flux [W], $\cos\theta_s$ is the angle to the optics measured from the normal of the radiating source, A_s [cm^2] is the area of the source, and Ω [steradians (sr)] is the solid angle subtended by the optic. The solid angle can be further simplified to

$$\partial \Omega = \frac{\partial A_o \cos\theta_o}{R^2} \tag{22}$$

where A_o is the area of the optic, $\cos\theta_o$ is the angle to the radiating source measured from the normal of the optic, and R [cm] is the distance between the optic and the source. Inserting Equation (22) into Equation (21) and solving for the radiant flux gives,

$$\Phi_{e\_optic} = \iint \frac{L_e \cos\theta_s \cos\theta_o \partial A_s \partial A_o}{R^2}. \tag{23}$$

A typical radiometric assumption can be made when $A_d << R^2$, which is called the paraxial approximation, and results in a algebraic solution,

$$\Phi_{e\_optic} = \frac{L_e \cos\theta_s \cos\theta_o A_s A_o}{R^2}. \tag{24}$$

Equation (24) can be further reduced if both the source and detector are coaxial, where $\theta = 0$, leaving both cosine terms equal to one. Thus, Equation (24) becomes the flux that arrives at the optics,

$$\Phi_{e\_optic} = \frac{L_e A_s A_o}{R^2} \tag{25}$$

In order to find the flux that arrives at the detector, a magnification of the radiating source area is used,

$$A_{imag} = \left(\frac{S_i}{R}\right)^2 A_s \tag{26}$$

where A_{imag} is the area of the image, and S_i is the distance from the image (detector) to the optic. Using this ratio, the portion of the flux that arrives at the detector can be found,

$$\Phi_{e\_det} = \frac{A_d}{A_{imag}} \Phi_{e\_optic}. \tag{27}$$

where A_d is the area of the detector.

A further discussion on the radiance (L_e) seen in Equation (25) is now needed. Since a blackbody source will be used, it can be assumed that the source is lambertian. By definition, a lambertian source is one that emits a flux proportional to the cosine of the angle from normal [4]. In other words, radiation is equally being emitted into 2π steradians. When the source is lambertian, the relationship between radiance and exitance can be made,

$$L_e = \frac{M_e}{\pi}, \tag{28}$$

where M_e, again is the exitance, and was shown in Equation (1). Dividing through by π leaves radiance as a function of wavelength and temperature,

$$L_e(\lambda,T) = \frac{2hc^2}{\lambda^5\left(e^{\frac{hc}{\lambda kT}}-1\right)} \left[\frac{W}{cm^2 \mu m}\right] \tag{29}$$

Remembering that this effort is to find the flux incident on the detector, replacing the L_e in Equation (25) with the $L_e(\lambda,T)$ of Equation (29) results in

$$\Phi_{e\_optic} = \frac{2hc^2 A_s A_o}{\lambda^5 \left(e^{\frac{hc}{\lambda kT}} - 1 \right) R^2}. \tag{30}$$

Now, the incident flux that arrives at the optic has been calculated. In an effort to find the flux that is incident on the detector, the transmittance of the lens must be taken into consideration. Each type of lens material will have a particular transmittance function, which is the fraction of light at a specific wavelength that passes through the material uninhibited. The lens that was used in this thesis was made from germanium (Ge) and had an anti-reflective coating that allowed for almost a 100 % passband between 8 - 14 μm. In order to find an accurate value of the flux that arrives at the detector, the transmittance function must be found. The best piece of equipment that allows for this type of material characterization is a Fourier transform infrared (FTIR) spectrometer. Figure 15a illustrates the transmittance function of Ge from the FTIR. Figure 15b represents a 700-K blackbody radiance. Figure 15c is the product of the transmittance function of the lens and the radiance of a 700-K blackbody source. This is the radiance that will be used to find the flux arriving at the detector. Therefore, Equation (30) becomes,

$$\Phi_{e\_optic} = \tau_{Ge}(\lambda) \frac{2hc^2 A_s A_o}{\lambda^5 \left(e^{\frac{hc}{\lambda kT}} - 1 \right) R^2} \tag{31}$$

where, $\tau_{Ge}(\lambda)$ is the transmittance function of the Ge lens as a function of wavelength (seen in Figure 15a).

The radiometry analysis has been discussed in an effort to find the flux arriving at the detector. Therefore, when using a blackbody source, Equation (27) will be used to calculate the flux arriving at the detector. The main objective of this section was to find the voltage output in response to this incident flux, which is the voltage responsivity. The change in voltage from that when the detector is not being exposed to incident radiation to when it is exposed, is the voltage output that will be used in calculating the voltage responsivity.

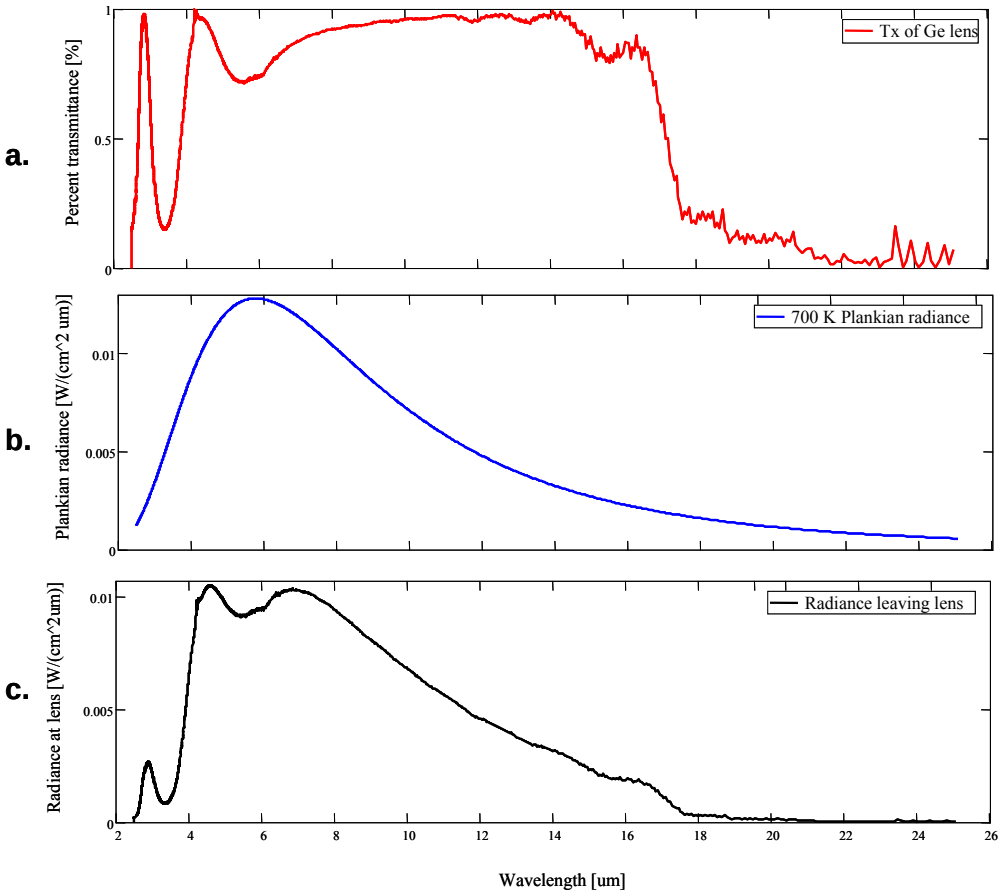

Figure 15: Data collected on the radiance seen before and after the germanium lens. This effort is crucial to obtaining an accurate flux calculation seen at the detector. a) The transmittance function of the germanium lens used in this thesis. Data was found using a FTIR. b) 700 K plankian radiance found using Equation (29). c) The radiance that will be seen by the detector.

2.5.3.2 Thermal Time Constant (τ_{th})

All IR detectors exhibit a characteristic transient behavior when the input IR flux changes abruptly. A general definition of the response time is the time it takes for the transient output signal to reach 63.2 % of its steady state change. In thermal detectors, the response time is typically slow, on the order of 1 – 100 msec. The thermal detector response time or thermal time constant, in the case of pyroelectric detectors, is related to the required accumulation of heat and is directly related to the increase in current on the output.

The thermal time constant, defined in Equation (7), again where C_{th} is the heat capacity of the active material in the detector and G_{th} is the total thermal conductance between the active area of the detector and the support structure, was illustrated in Figure 6. The heat capacity, C_{th} $[J/K]$, is the total capacitance which incorporates individual capacitances for each material comprising the detector active region. Heat capacity is the amount of heat required to raise the temperature of one gram of material by one degree Celsius (without a change in phase), which is basically the ability of the sensing material to store and bleed off heat. Therefore, for thermal sensing materials, the heat capacities need to be small, and can be made smaller by decreasing the film thickness.

Of critical importance in thermal detectors is the need to minimize the thermal conductance, G_{th} $[W/(mK)]$ [15]. This concept is shown by an analytical evaluation of Equation (11). In an effort to maximize the sensitivity, ΔT, the thermal conductance of the support structure needs to be small. At the same time, by decreasing the thermal conductance, the thermal time constant is increased, which leaves an engineering trade-

off between a fast thermal time constant and a high responsivity. A fast thermal time constant can be achieved by reducing the thermal material's heat capacity and a high responsivity can be achieved by thermally isolating the pixel's active region from the underlying substrate and by minimizing the thermal conductance of the support structure. Both the thermal time constant and the responsivity are incorporated into the next FOM, NEP.

2.5.3.3 Noise Equivalent Power (NEP)

Noise equivalent power (NEP) is the root mean squared (rms) value of the incident chopped radiant power that is necessary to produce an rms signal equal to the rms electrical noise. Before this FOM can be understood, the noise associated with pyroelectric detectors must first be explained.

Every detector of thermal radiation is also a detector of noise. Pyroelectric detectors are susceptible to three main types of noise. The sources of pyroelectric detector noise are as follows:

1) Microphonic noise – noise caused by a mechanical displacement,
2) Temperature noise – noise due to the heat exchange between the detector and its environment,
3) Johnson noise – fluctuations caused by the random thermal motion of the charge carriers in a resistive element.

Each source of noise and its importance in pyroelectric detector FOMs will be discussed below.

Microphonic noise is observed in many radiation detectors when there are mechanical vibrations propagated through the detector. A good indication of microphonic noise is its periodicity due to the fact it is made up of sinusoidal waves with their respective eigenvectors [14]. This noise results from changes in interelectrode capacitances. The equation for capacitance is

$$C = \frac{\varepsilon_d A}{d} \tag{32}$$

where ε_d is the dielectric constant, A is the area of the plates of the capacitor, and d is the distance between the parallel plates. When there is a mechanical vibration, the distance between the electrodes changes by Δd, thereby producing a voltage for a given amount of charge with a change in capacitance [2]. Thus, Equation (32) then becomes

$$\Delta C = \frac{\varepsilon_d A}{d \pm \Delta d}. \tag{33}$$

Figure 16 illustrates the result of microphonic noise using a single cantilever.

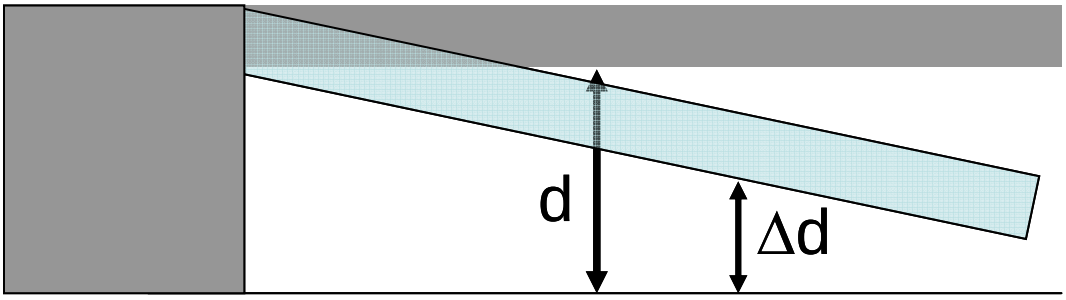

Figure 16: An illustration of a cantilever capacitor. When perturbed by vibrations, the distance between the cantilever and the bottom electrode changes by Δd thereby changing the capacitance.

The next type of noise that is prevalent in pyroelectric detectors is temperature noise. This noise is essentially the temperature fluctuation of the sensitive element. In

the case of all thermal detectors, the ultimate performance is attained when the detector is temperature-fluctuation limited. This means that the detector will only have an electrical response when there is a change in temperature. A good derivation is done by Dereniak [2] that leads to the spectrum of the mean-square fluctuations in temperature,

$$\Delta T^2 = \frac{4kG_{th}T^2\Delta f}{G_{th}{}^2 + \omega^2 C_{th}}, \tag{34}$$

where Δf is the noise equivalent bandwidth. This noise equivalent bandwidth is defined as an electrical filter with ideal uniform gain through the passband, and zero gain outside, essentially a rectangular function in frequency space. Noise equivalent bandwidth is used when the heating/cooling of a detector is achieved using a blackbody source complimented with an optical chopper wheel. The mathematical expression for the noise equivalent bandwidth for a square wave, derived in [2] is

$$\Delta f = \frac{1}{2\tau_{int}}, \tag{35}$$

where τ_{int} is the integration time, which is the on-time/off-time for a square-wave chopping.

Johnson noise is the last type of noise that is typically found in pyroelectric detectors. In general, pyroelectric detectors are operated in this Johnson noise-limited region. This means that Johnson noise is the dominating source of noise. Johnson noise, by definition, is the fluctuation caused by the thermal motion of the charge carriers in a resistive element. The Johnson noise represented by a current, again derived in [2], is

$$i_J = \sqrt{\frac{4kT_d\Delta f}{R_d}}, \tag{36}$$

again, where k is the Boltzmann constant, T_d is the temperature of the detector, Δf is the electrical bandwidth, and R_d is the resistance of the material. The voltage equivalent Johnson noise can also be represented by

$$v_j = \sqrt{4kT_dR_d\Delta f}\ . \tag{37}$$

NEP is defined as the minimum radiant flux level a detector can discern depending on the detector's noise level. The signal produced from the detector, as a response to incident radiation must be above the noise floor to be easily detected. The signal-to-noise ratio (SNR) can then be expressed in terms of the current responsivity of a pyroelectric detector,

$$\text{SNR} = \frac{\Re_i \Phi_e}{i_n} \tag{38}$$

where, i_n is the noise current produced in the detector. The incident power that produces an output current such that SNR = 1, is defined as NEP. Therefore Equation (38) becomes,

$$\text{NEP} = \frac{i_n}{\Re_i}\ . \tag{39}$$

The same applies for voltage responsivity,

$$\text{NEP} = \frac{v_n}{\Re_v}\ , \tag{40}$$

where v_n is the voltage noise.

When designing detectors, the smaller the NEP, the more sensitive the detector is. NEP is dominated by the square root dependence of both the noise equivalent bandwidth (Δf) and the area (A_d). This problem was mitigated when Jones (1953) normalized the

NEP to a 1-cm^2 detector area and a 1-Hz noise bandwidth. The term for this is detectivity (D*) and will be discussed next.

2.5.3.4 Detectivity (D)*

Detectivity is a very important FOM for IR detectors. This FOM is the sensitivity of the detector normalized to a 1-cm^2 detector area and a 1-Hz noise equivalent bandwidth. The larger the number quantified for D*, the better. D* is defined by

$$D^* = \frac{\sqrt{A_d \Delta f}}{NEP} \tag{41}$$

The units of D* are Jones, where 1 Jones = [cm Hz$^{1/2}$ W^{-1}]. D* was originally proposed for quantum detectors using the aforementioned scaling of area and bandwidth. Unfortunately, this trend is not always obeyed in thermal detectors due to the fact that neither a temperature fluctuation, nor thermo-mechanical noise, scales with the size of the detector area [15]. The D*, given in Equation (41), typically overestimates the performance of larger absorbing areas in thermal detectors and underestimates that of smaller area detectors.

Making the assumption that the major source of noise in the detector is Johnson noise and that voltage responsivity is what is being measured, Equation (40) can further be defined by

$$NEP = \frac{v_j}{\Re_v} = \frac{\sqrt{4kT_d R_d \Delta f}\sqrt{1+\omega^2 \tau_{th}{}^2}\sqrt{1+\omega^2 \tau_e{}^2}}{p\varepsilon A_d}, \tag{42}$$

which can be placed back into Equation (41) to give

$$D^* = \frac{\sqrt{A_d \Delta f}}{NEP} = \frac{\sqrt{A_d R_d}\, p\varepsilon A_d \omega}{G_{th}\sqrt{4kT_d}\sqrt{1+\omega^2 \tau_{th}{}^2}\sqrt{1+\omega^2 \tau_e{}^2}}. \tag{43}$$

2.5.4 Pyroelectric Detector Structural Design

All thermal detectors require thermal isolation from the underlying substrate to maximize sensitivity and performance. The ability to form raised structural designs in semiconductor fabrication is a direct result of solid-state micromachining [16]. The main rational for this isolation is to minimize the unwanted conduction path between the thermal sensing area and the associated substrate. In an effort to achieve thermal isolation, two methods are typically employed. The first method, commonly termed bulk-micromachining, uses chemicals to remove a substantial portion of the semiconductor substrate. The second method employed, called surface-micromachining, is the process of depositing sacrificial materials (removable layer) and structural materials. Both of these methods are employed to achieve the thermal isolation and are illustrated in Figure 17.

It is evident from Figure 17 that the pyroelectric detector pixel resembles a thermally isolated parallel plate capacitor. This design type is employed due to the physics of this device. Incident radiation must heat up the top surface of the structure, thereby invoking an alignment of the electrical dipoles in the pyroelectric material. This alignment produces a current through the material which can be measured at the electrodes.

There are two main designs for the electrode configuration of pyroelectric detectors. The first design, shown in Figure 17, is the face electrode configuration. In this form, the top electrode must be blackened in an effort to maximize the absorption of heat. This heat is then transferred to the pyroelectric material where it performs its

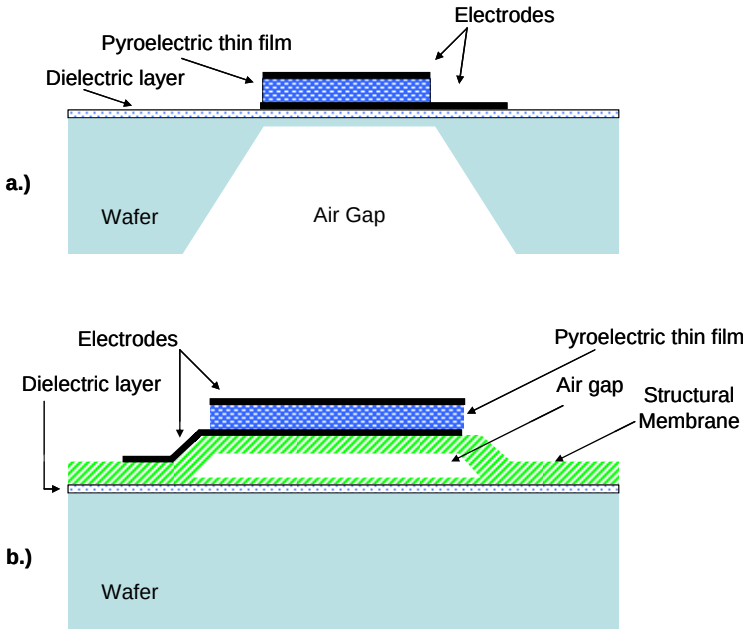

Figure 17: Two typical pyroelectric detector structures constructed using both, a) bulk-micromaching technique – in which unwanted layers are removed using chemical etching, and b) surface micromachining technique – where thin film layers are added (deposited) and one of the layers is selectively removed [15].

physical phenomenon to detect objects in the IR. The second design configuration is termed the edge electrode method. In this design, the electrodes are located on the sides of the pyroelectric material. This time, since the IR flux is being absorbed by the pyroelectric material itself, it also must be blackened to enhance this process. These two electrode configurations are shown in Figure 18.

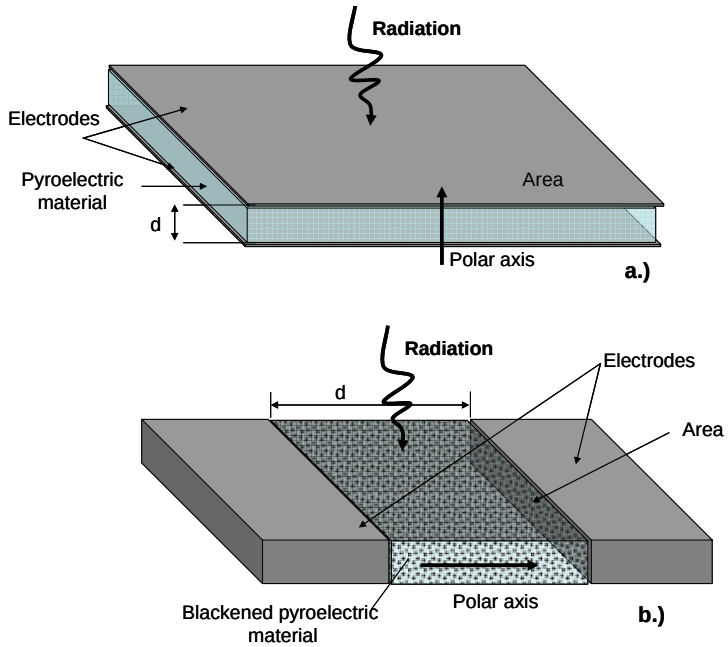

Figure 18: Typical electrode configuration used in pyroelectic detector designs. a) Face electrodes – a thin film of pyroelectric material is sandwiched between two vertically deposited electrodes. b) Edge electrodes – a thin blackened film of pyroelectric material is deposited between two horizontally spaced electrodes [17].

2.5.5 Pyroelectric Material Deposition

There are many deposition techniques used to deposit thin pyroelectric films. Four techniques that will be described include sputtering, metal organic chemical vapor deposition (MOCVD), laser ablation, and lastly, the Langmuir-Blodgett method. The objective of this section is to give a brief introduction into these deposition methods. In this thesis, a new technique of depositing the novel PIP pyroelectric material will be demonstrated.

Sputtering is a deposition process where atoms are ejected from a solid target by the bombardment of energetic atoms. This process allows for the growth of thin layers of materials with sub-micron thicknesses. One major pyroelectric material that uses

sputtering to deposit thin films on silicon substrates is lead scandium tantalite (PST). It must be noted that this technique lays a conformal layer across the substrate. Therefore, in an effort to design pyroelectric detectors, subsequent steps (i.e., chemical etching, thermal annealing, and other epitaxial growth techniques) in the fabrication process need to be accomplished. This means that the pyroelectric material used needs to be compatible with all of these steps.

MOCVD is yet another pyroelectric deposition technique that is typically used when depositing pyroelectric thin films. MOCVD is a vapor phase epitaxial growth process that forms thin layers by a chemical reaction between gaseous compounds and the substrate [19]. As the source gas is flowed over the heated substrate, metal-organic bonds are broken, creating a chemical bi-product that grows as a crystalline structure on the substrate. This technique is typically used on lead-based pyroelectric materials, such as PLT [20]. Again, this technique deposits a conformal layer across the entire substrate, so all subsequent fabrication steps must be compatible with the material.

Laser ablation deposition, commonly known as pulsed laser deposition (PLD), is a newer deposition technique that uses a pulsed laser to deposit thin films of a wide range of target materials onto multiple types of substrates. The main benefit of this technique is that the target materials can be deposited at room temperature. It has been found that PLD, in comparison to other deposition methods, can synthesize the pyroelctric film at a faster rate, with closer stoichiometric control, and with a wider variability in the deposition parameters [21]. Two of the pyroelectric materials that have used this technique are PLT and SBN-50.

Although there are many pyroelectric deposition techniques used, the final method to be discussed is the Langmuir-Blodgett (LB) thin film technique. This is an elegant method for producing high quality organic films of precisely defined thickness and symmetry [22]. Basically, the substrate is immersed into the liquid to be deposited. A monolayer is added with each immersion step, leading to accurate growth thicknesses [23]. LB has been demonstrated using layers of fatty acid and fatty amine, which are two proteins that have exhibited the pyroelectric effect. Eleven layers demonstrated a thickness of ~34 nm using the LB process on fatty amine [22].

2.5.6 Pyroelectric Signal Conditioning

As shown in Figure 13, the pyroelectric detector is typically modeled as a capacitor, due to the material's extremely high DC resistance (~10^{13} Ω). The capacitance is found to be very low (30 pF). Thus, the detector has very large impedance which makes reading the signal output difficult. Therefore, in an effort to bring this high impedance down to a manageable level, two methods can be employed: voltage follower or current amplifier. Both of these amplification schemes have their advantages and disadvantages [24].

The pyroelectric detectors that use the voltage follower circuit offer low output impedance and a high SNR. Also, referring back to the voltage responsivity, the output response for this method of amplification will be frequency dependant (see Figure 14). The voltage follower circuit is used as a trans-impedance circuit which is illustrated in Figure 19.

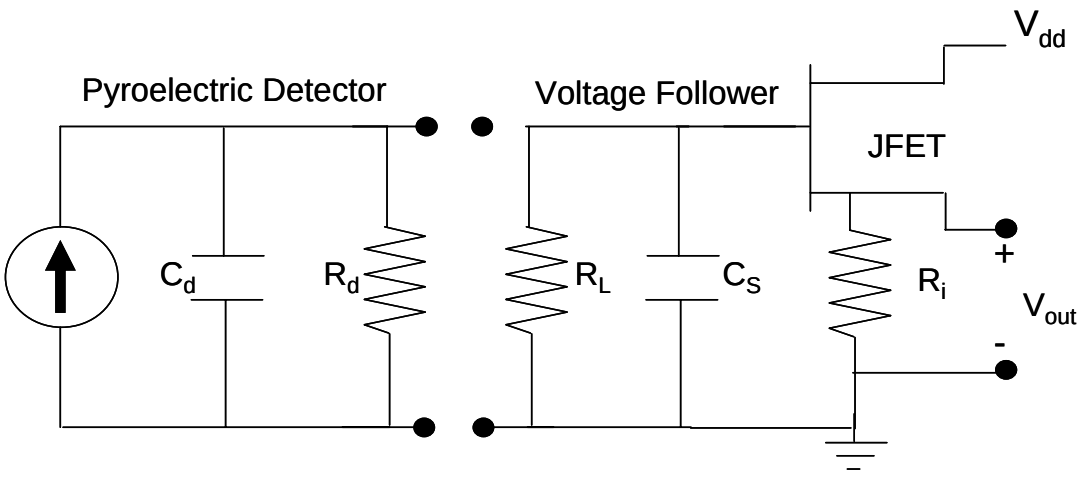

C_d: Pyroelectric capacitance
R_d: Pyroelectric resistance
R_L: Resistance connected in parallel with pyroelectic element
C_S: FET input capacitance
R_i: Resistance to prevent leakage current

Figure 19: Pyroelectric detector connected to a voltage follower circuit (source follower) [2].

The other signal amplification method that allows for bringing the output response above the noise floor is the high impedance amplifier, where current mode offers a much greater amplification of the signal. This method, shown in Figure 20, uses an operational amplifier with a feedback resistor (R_F) in parallel with a feedback capacitor (C_F). Using this mode to amplify the signal allows for a flatter frequency response (represented in Figure 12). The downside to this method is the low SNR and the higher operating current and voltage requirements [25].

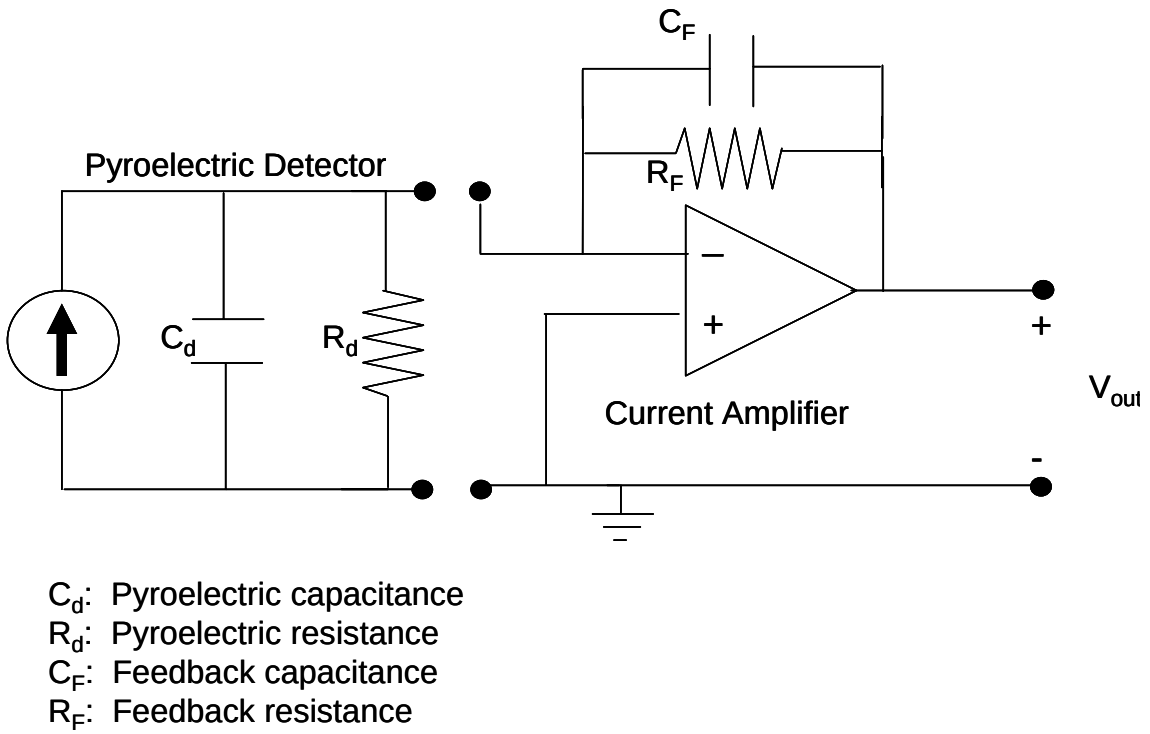

Figure 20: Pyroelectric detector connected to a high impedance amplifier [2].

2.6 Chapter 2 Summary

The intent of Chapter 2 was to give the reader a background understanding of IR detection. As will be shown in the next chapter, PIP was found to be a pyroelectric material; therefore, Chapter 2 concentrated on pyroelectric detectors. All aspects of pyroelectric detectors were discussed, to include materials, theory of operation, FOMs, detector structures, currently used thin film deposition techniques, and lastly, some pyroelectric detector signal conditioning circuit designs.

2.7 Works Cited

[1] Keyword: "Blackbody," http://www.wikipedia.com

[2] Dereniak, E.L., Boreman, G.D. *Infrared Detectors and Systems*. New York: John Wiley & Sons, Inc., 1996.

[3] Keyword: "Wien's displacement law," http://www.wikipedia.com

[4] Sqn Ldr Sharma, UC., "Infrared Detectors," *M. Tech Credit Seminar Report, Electronic Systems Group, EE Dept, IIT Bombay*, pp 1 -26, Oct 2004.

[5] Keyword: "Atmospheric window," http://www.wikipedia.com

[6] Keyword: "Emissivity," http://www.wikipedia.com

[7] Rogalski, Antoni., *Infrared Detectors*. The Netherlands, Gordon and Breach Science Publishers, 2000.

[8] Keyword: "Thermocouple," http://www.wikipedia.com

[9] Datskos, P.G., Lavrik, N.V., Rajic, S., "Performance of uncooled microcantilever thermal detectors." *Review of Scientific Instruments*, vol 75, pp 1134 – 1148, Apr 2004.

[10] Ding-Quan, Xiao & Lang, Sidney B., "Measurement application based on pyroelectric properties of ferroelectric polymers," *IEEE Transactions on Electrical Insulation*, vol 23, pp 503 – 515, Jun 1988.

[11] Preezant, Yulia. "Advanced laboratory report – Pyroelectricity: Triglycine sulfate crystal growth and characterization." 18 Aug 2003.

[12] Ok, Min, Kang, et al, "Bulk characterization methods for non-centrosymmetric materials: second harmonic generation, piezoelectricity, pyroelectricity, and ferroelectricity." *Chemical Society Reviews*. vol 35, pp 710 – 717, 2006.

[13] Lang, Sidney, B. "Pyroelectricity: From ancient curiosity to modern imaging tool." *American Institute of Physics*. pp 31 – 36, Aug 2005.

[14] Hossain, Akram. "Pyroelectric detectors and their applications." *IEEE transactions on Industry Applications*. pp 2301 – 2307, 1989.

[15] Datskos, Panos, G., Lavrik, Nickolay, V., "Detectors –Figures of Merit." *Encyclopedia of Optical Engineering*, pp 349 – 357, 2003.

[16] Kruse, Paul, W., Skatrud, David, D., *Uncooled Infrared Imaging Arrays and Systems*. Boston, MA: Academic Press, 1997.

[17] Liu, S.T. and Long, Donald. "Pyroelectric Detectors and Materials," *Proceedings of the IEEE*, vol 66, pp 14 – 26, Jan 1978.

[18] Keyword: "Sputtering," http://www.wikipedia.com

[19] Sze, S.M., *Semiconductor Devices, 2nd Edition*, John Wiley & Sons Inc: Lehigh Press, 2002.

[20] Roeder, J.F, et al, "Liquid delivery MOCVD of PLT pyroelectric detectors," *Proceeding of the IEEE*, pp 227 – 230, 1996.

[21] Wang, Hui-Ling & Hu, Chen-Ti Hu, "Laser ablated pyroelectric thin films for room temperature IR sensors," *Electronic Devices and Materials Seminar*, pp 13 – 16, 1994.

[22] Jones, Carole, A., Petty, Michael, C., & Roberts, Gareth, G., "Langmuir-Blodgett films: A new class of pyroelectric materials." *IEEE Transactions*, pp 736 – 740, 1988.

[23] Keyword: "Langmuir-Blodgett films," http://www.wikipedia.com

[24] Chirtoc, M., et al., "Current mode versus voltage mode measurements of signals from pyroelectric sensors," *Review of Scientific Instruments*, vol 74, pp 648 – 650, 2003

[25] Eltec Instuments Inc., "Introduction to infrared pyroelectric detectors," Application notes, ELTECdata #100, 2002.

[26] Newsome, R.W., "Measurement of the pyroelectric coefficient of poly(vinylidene fluoride) down to 3 K," *The Amercian Physical Society*, vol 55, num 11, pp 7264 – 7271, 1997

III. Material Characterization and Sample Preparation

3.1 Chapter Overview

The intent of Chapter 3 is two-fold. First, the material must be better understood before it can be characterized with FOMs as a thermal detection device. This includes a description of the test evolution that was accomplished to define why PIP is presumed to be a pyroelectric-type thermal detection material. Secondly, in an effort to transpose from the macro-world to the micro-world, a description of how the sample was prepared is necessary. Describing the structural design that will support this newly found thermal detection material is the first step to understanding the sample preparation. The design of the structure that makes this effort possible will first be described, which is a MEMS-based design fabricated with the PolyMUMPs foundry. Next, in addition to the pixel design, the novel deposition method used to transport the material onto the pixel will be discussed. Inkjet deposition is the system that makes this possible, therefore, a complete description on the theory of operation of the system and the inkjet droplet characterization will be reviewed.

3.2 Material Characterization

The basis of materials science relates the desired properties and relative performance of a material in a particular application to the structure of the atoms and phases in the material under investigation, through material characterization [1]. Typically, a device is made from first understanding the material, then optimizing the material for peak performance. This order of events may not always be the case, as was seen in the PIP thermal detector.

3.2.1 PIP...the Bolometric Detector

While trying to measure the conformal changes of the TlpA strand of *salmonella* embedded in polyvinyl alcohol (PVA), it was found that the material was responsive to incident thermal radiation. This discovery led to research aimed at creating a biomimetic material for thermal imaging [2]. As indicated in Chapter 1 of this thesis, Figure 2 illustrates a protein-based polymer array of pixels. Testing of these pixels concluded that the PIP-based pixels were bolometer-type thermal detectors, meaning the resistance changes with respect to temperature. Typical bolometric detectors will have a particular resistance for a given temperature. This is not case for the PIP-based thermal detection material, as will soon be shown.

FOMs are the core of this thesis topic; therefore, an understanding of the material characteristics is needed. In an effort to better understand the electrical response, macro-scaled PIP-based material samples were prepared and then tested. The samples were prepared by AFRL/MLPJE by dropwise depositing the solution onto a four electrode circuit board. By using a squeegee technique, the samples were uniformly coated with any desired thickness (~1– 250 μm) [2]. Figure 21 is an illustration of the samples that were prepared by AFRL/MLPJE. The samples are ideal for electrical characterization because the circuit board allows for easy access to the electrodes for biasing/measuring the electrical properties of the material.

Once the PIP was deposited onto the circuit board, electrical characterization commenced. First, in an effort to understand the PIP's electrical response and further duplicate the efforts of AFRL/MLPJE's experiments, resistance measurements were

taken. Initially, an Agilent 34410A digital mulitimeter was used to capture resistance data. The results quickly showed that the electrical resistance of the PIP material far exceeded the resistance measurement specs of the device (~1 GΩ).

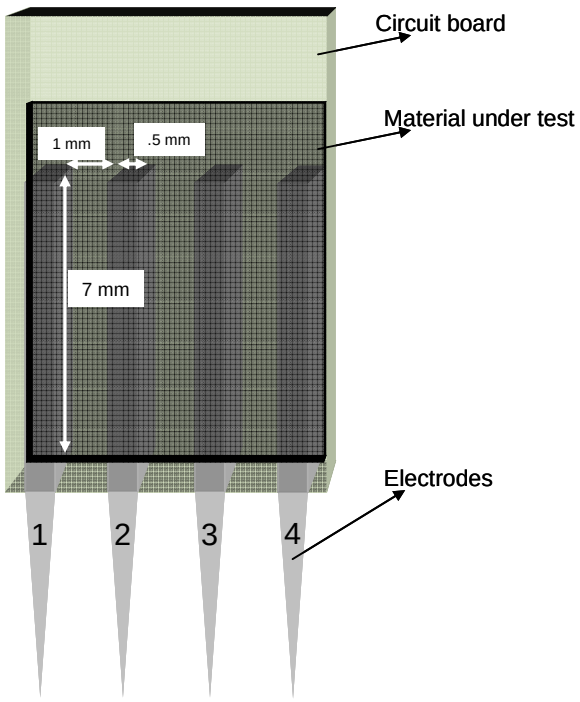

Figure 21: An illustration of the PIP based thermal detector samples prepared by MLPJE. These samples were prepared in an effort to electrically characterize the material.

High resistance implies low current and one device that is made for this type of measurement is the Keithley 6517a electrometer. This device is capable of measuring extremely high resistances (> 100 TΩ) and low currents (~0.1 pA). The 6517a comes equipped with an internal voltage source that allows for biasing with voltages of 100 V, while simultaneously measuring V/I, which from Ohm's law, is resistance. The sample was first placed into a breadboard and electrically connected to the Keithley 6517a for resistance measurements.

Using a 100-V bias, the resistance between electrodes, 1 and 2, 2 and 3, and 3 and 4 (shown in Figure 21) were measured. The material's electrical response was unusual, because the resistance increased with time. The results of this experiment can be seen in Figure 22. Typically, bolometers will possess a specific resistance for a particular temperature from a heat source. In the case of this experiment, since there was no heat source incident on the sample, the resistance should stabilize (flat-line) to the ambient background temperature. Many unsuccessful sub-experiments were performed, to include an overnight resistance measurement, in an effort to stabilize this resistance. Also, an interesting aspect of this material's electrical resistive response is that each pixel tested has a defined slope.

To demonstrate the material's thermal response, an experiment was conducted that exposed the same sample to a heat source (flashlight) at a distance of 12 inches from

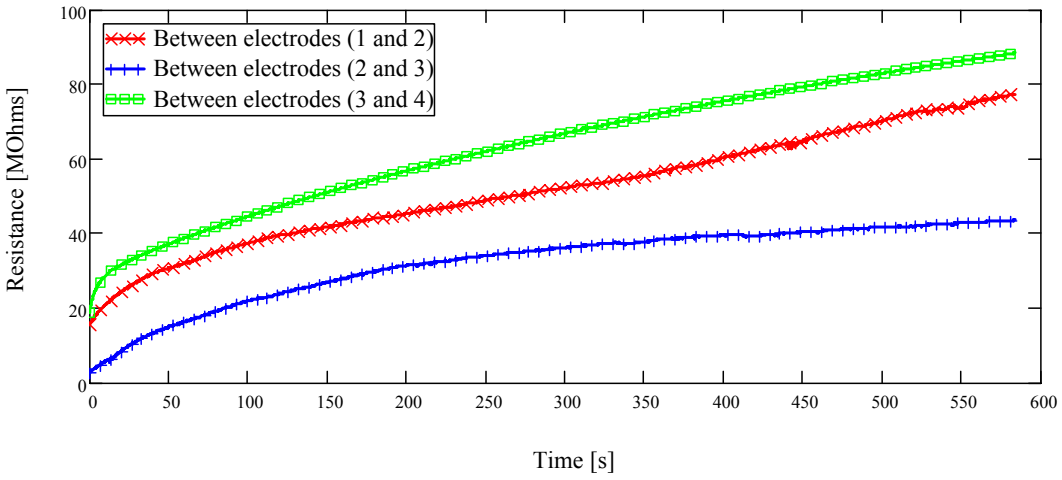

Figure 22: The resistance measurements initially performed on PIP sample. Three pixels were tested with a 100 V bias, while simultaneously measuring the resistance. The resistance was found continuously increases with time having a defined slope for each of the pixels measured.

the same sample. The thermal response was reproduced to the results found by AFRL/MLPJE, in which the material had a negative temperature coefficient of resistance. This means when the material is heated, its resistance decreases. After exposure to the thermal source, the resistance decreased significantly. When the source was removed, the resistance slowly increased back to the original rate of change that was found prior to thermal exposure. Three exposures were demonstrated in this experiment, and can be seen in Figure 23. The thermal response from the exposure to heat (flashlight) can be attributed to the thermal bleed-off of the sample where the exposed pixel is cooling back to ambient conditions. In thermal detectors, this process needs to be as fast as possible in an effort to be ready for the next scene to be imaged. A quick analysis of Figure 23 shows that the time it takes the resistance, after the first exposure, to reach the original resistance prior to thermal stimulus (~ 0.64 GΩ) is ~ 34 seconds. This thermal time constant is far too slow if this sample were to be employed as a thermal detector. The

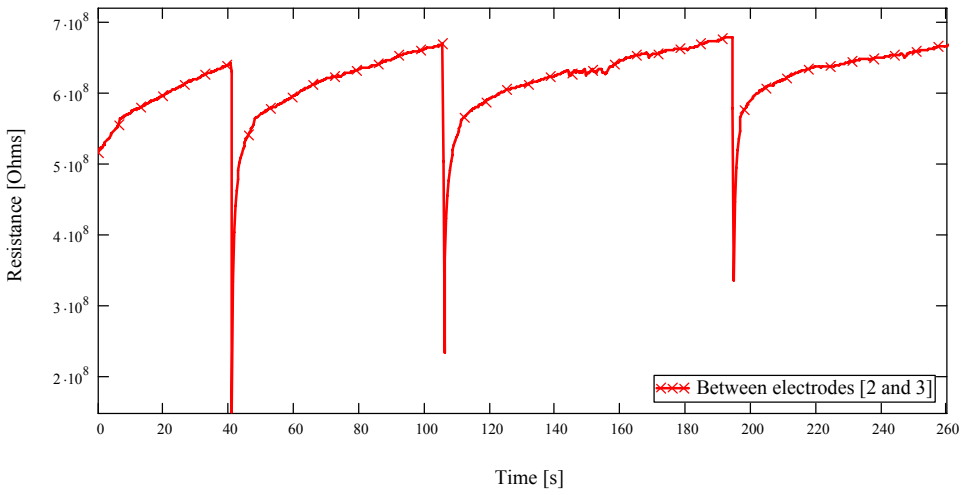

Figure 23: PIP material's thermal response stimulated by a flashlight at ~ 12" from the sample. The material portrays a negative temperature coefficient of resistance with a thermal stimulus. The resistive recovery after thermal exposure seems to slowly increase back to its original resistive rate of change prior to thermal exposure.

main cause of this slow thermal time constant is the large thermal mass of the sample under test and lack of thermal isolation from the underlying support structure, in this case, the circuit board.

The continual increase in resistance causes significant problems when trying to evaluate PIP's potential as a thermal detector. Each thermal detector has its own unique K value, as in Equation (8). In the case of bolometers, the K value is known as the TCR. The formula that governs a bolometer's TCR is given by

$$\mathrm{TCR} = \frac{1}{R_d}\frac{dR_d}{dT}\left[\frac{1}{K}\right], \tag{44}$$

where R_d is the resistance of the material, and dR_d/dT is the resistive change with respect to the induced temperature change. It is evident from Equation (44) that there is no time dependence on the resistance. This concept imposes a problem when trying to experimentally find a TCR value for a material that has a resistance that increases with time while under bias. Also, each time the sample was biased, a different value for resistance was measured. This also imposes a problem, as the resistance of the sample is inversely proportional to the TCR.

An attempt to find PIP's TCR value was pursued. As expected, due to the continuous rate of change in the resistance, the TCR results were not reproducible. The temperature ramp executed was 8 K/min from 280 - 380 K. The TCR values at 300 K ranged from -0.05 K^{-1} to -0.28 K^{-1}. Without the ability to accurately measure the TCR, which is directly proportional to responsivity ($\Re$), as indicated in Equation (9), all FOMs could not be accurately compared to commercial off-the-shelf bolometers.

The PIP material obviously had a thermal response as indicated from Figure 23, but the question still remained on the type of thermal detector this material was. With the end-state of this thesis being FOMs, it is imperative that an accurate and reproducible K value be found. Since there was no background research found on the type of resistive response in other types of bolometric materials, further investigations on PIP being bolometric ceased. Research was re-vectored to an other type of thermal detector, namely pyroelectric.

3.2.2 PIP...the Pyroelectric Detector

The rationale that led to the realization of PIP being a pyroelectric device was two-fold. First, one of the commonly used materials for pyroelectric devices is PVF (polyvinyl fluoride). The PIP material is made up of ~60% PVA (polyvinyl alcohol). The differences between PVF and PVA are apparent to material scientists and will not be discussed here. The fact that polymer was used in thermal detection introduced the thought that PIP had potential to be a pyroelectric-type material.

The second indication that PIP could be a pyroelectric material was that fact that the material demonstrated ferroelectric properties. As indicated in Chapter 2, ferroelectric materials are also pyroelectric, but in addition to having a spontaneous polarization, also have a reversible dipole moment in the presence of an electric field. This discovery was proven with a simple experiment. The same sample shown in Figure 21 was biased, using the Keithley 6517a's voltage source, with a 100 V. Most ferroelectric type materials are good dielectrics and are used in capacitors. Therefore, after the application of an electric field, a charge can be measured through the electrodes,

and will dissipate with time. Upon removal of the bias, the current was measured through the material. The sample was then biased again, this time, swapping the leads from the original biasing. Again, the current was measured; this time the sign was reversed. This simple experiment further solidified the fact that PIP could be evaluated as a pyroelectric material.

From this point forward, a great deal of research went into the understanding of pyroelectric detectors, as indicated in the background discussed in Chapter 2. One of the significant aspects of pyroelectric detectors is the fact that they generate a current with a change in temperature. Therefore, an experiment was set-up to determine if this concept was true for the PIP material. Basically, the same sample shown in Figure 21 was placed onto a temperature-controlled stage. The stage also had the ability to accurately monitor the temperature of the stage. The details of this experiment will be further discussed in Chapter 4, as the experimental setup is critical in defining the K value for pyroelectric detectors, the pyroelectric coefficient.

The temperature of the stage was increased while simultaneously measuring the current generated by the sample. Again, the pixel located between electrodes 2 and 3 was the pixel under test. As indicated through much of the literature [3], samples are typically biased for a short period of time before measuring the current generated due to a ramp in temperature. The main rationale for this biasing is to align the polar axis perpendicular to the face of the electrodes (see Figure 18b), maximizing the current generated in the material. This biasing technique is termed poling.

The intent of the current generation experiment was three-fold. First, prior to data capture, the sample was biased for 1 hour at 100 V. Once data capture of the current commenced, the time it took for the sample to bleed off the charge was measured. Second, in an effort to determine how the current generated is affected over time, a 7-hour test was accomplished. Throughout the duration of this experiment, the current was recorded using the Keithley 6517a, while simultaneously increasing the temperature conductive stage at random intervals during this 7-hour experiment. Lastly, it is of the utmost importance to have a stabilized ambient electrical output when no thermal stimulus is present. Essentially, what is needed is the noise floor measurement. This was accomplished by not exposing the sample to thermal stimulus for a prolonged period of time in between temperature ramps. The results of this experiment are shown in Figure 24.

Due to the fact that the sample was exposed to thermal stimulus prior to the sample reaching a steady state current output, it is difficult to give a quantitative time for the bleed-off of all charge built up during the 1-hour of biasing. From a quick analysis of the plot shown in Figure 24, the current response seems to be flat-lined at ~ 1.25 hrs. The bleed off of the charge has a strong dependence on the time the sample was biased. Although not displayed in this figure, multiple tests were conducted that show the longer the sample was biased, the longer the charge took to bleed off. Next, the fact that PIP is a pyroelectric device was confirmed as a thermal stimulus generated 4.8 – 8.6 nA of current. The first two temperature ramps were increased from 297 - 350 K at a rate of 8 K/min. When the temperature reaches 350 K, the material no longer recognizes a change

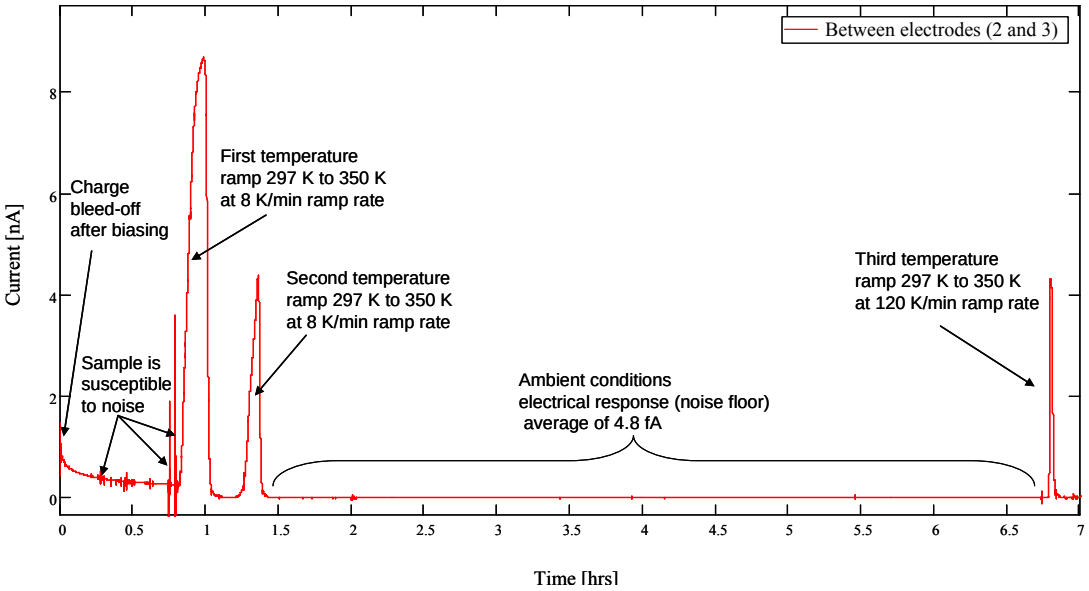

Figure 24: Spontaneous polarization current generated in the sample seen in Figure 21 (pixel between electrodes 2 & 3). The sample was tested over time to evaluate the charge bleed off time after biasing, the thermal response over a long period time with the sample exposed to random intervals of thermal stimuli, and lastly the noise floor.

in temperature and currentdecays back to the background level. If the temperature remains at 350 K, there will be a slower current decay back to zero. In the experiment shown in Figure 24, when the temperature reached the maximum temperature of 350 K, power to the stage was removed which resulted in the stage temperature dropping to ambient conditions, decreasing the pyroelectric current quickly back to zero. It is evident that the first thermal stimulus generated the greatest amount of current. This is typically the case for the first thermal response of a pyroelectric detector after poling. As indicated from [3], "observation of pyroelectric measurements performed subsequent to the traditional poling method lead to a higher value on the first heating and cooling cycle and then stabilizes at a lower value, which can be as much as 50% lower." This 50% decrease in the pyroelectic current is also evident from the second and third temperature

ramps in comparison to the first temperature ramp. Lastly, the noise floor analysis was taken during the 5.3-hour time frame where no thermal stimulus was present. The measured current stabilized to the ambient background conditions of the laboratory where the rms current for the 5.3 hours was found to be ~ 4.8 fA, which is for all practical purposes zero. In an effort to effectively measure a thermal response, a zero flat-lined noise floor is ideal.

3.2.3 Summary of the Material Characterization

The last two sections have summarized the evolution of the material characterization of the PIP material. First, the material was thought to be a bolometric type in which the electrical measured response is resistance. The continuous increase in resistance with respect to time was a hindrance when trying to characterize PIP as a thermal detector. The ability to duplicate TCR measurements is critical, but was not possible. Background research then led to the PIP material having potential to be a pyroelectric detector, which generates a current in response to a thermal stimulus. This hypothesis was confirmed with the results shown in Figure 24, where a spontaneous polarization current was generated when the sample was exposed to a thermal stimulus. The bifurcation on whether PIP was a bolometric or pyroelectric material was easily vectored toward the latter. Now that PIP is a proven thermal sensing material, the need to move to the micro-scale is critical. The next section is dedicated to giving an in-depth understanding of the sample preparation to transition from the macro-scale to the micro-scale, to include the structural analysis of the pixel and the deposition method used to garner small volumes of the PIP material.

3.3 Sample Preparation

The intent of this section is two-fold. In the first section, an analysis of a surface micromachined MEMS structure fabricated with the PolyMUMPs foundry will be discussed. The basis for the chosen design will be described, along with an analytical, modeled, and experimental comparison on the pixels' structural design.

The second section will describe how the PIP material will be strategically deposited to individual pixels. This microdispensing will be performed with Microfab's inkjet printer head. A characterization of the PIP droplet will be performed using a microscope camera, atomic force microscope (AFM), and a white-light interferometer. This analysis will give insight into the topography of a single droplet and the potential sensing area that will be used when the material is deposited onto a pixel.

3.3.1 The MEMS Pixel Designs

As described in Chapter 1, the pixel design must incorporate four major aspects: thermal isolation, interdigitized fingers for the material deposited to complete the circuit, large enough area for untried ink jet deposition, and the ability to be electrically monitored. In this section, each of these attributes will be described. Also, some of the materials used in the PolyMUMPs foundry will be referenced in this section without any description. For a complete description of the PolyMUMPs foundry that fabricated the MEMS devices shown in this thesis, the reader should refer to Appendix 1.

Thermal isolation is critical to the performance of all thermal detectors. The further the distance the sensing material is from the underlying substrate, the more responsive the material will be as a thermal sensor. In an effort to maximize this

distance, the main support structure will be made of Poly-2, and a thin film of gold will be deposited onto the Poly-2. The differences in stress will cause the structure to deflect in the upward z-direction. Figure 25 is a finite-element-modeling image of a Poly-2/gold cantilever beam to illustrate this effect.

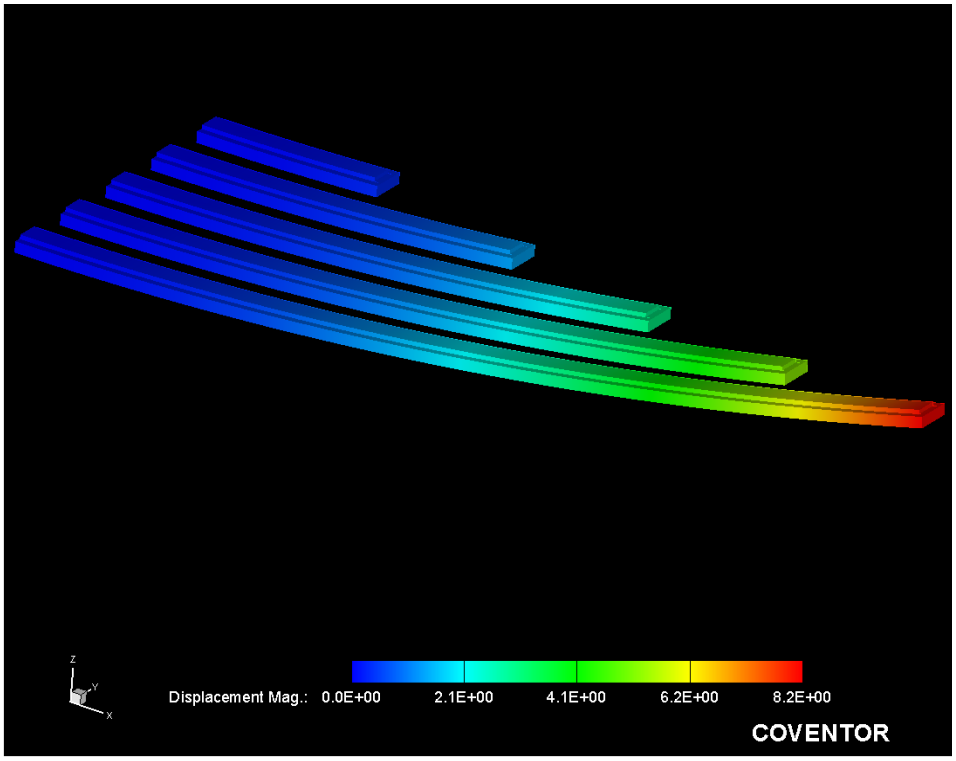

Figure 25: A poly 2-gold cantilever beam modeled in Coventorware. The differences in stress cause the beam to deflect in the z-direction. This effect will be used to maximize thermal isolation in the pyroelectric pixel.

It is evident that the longer the cantilever beam, the more it will deflect. This premise will be used to both maximize thermal isolation and to compensate for the weight of the PIP material. After depositing the PIP material, it is envisioned that the mass of the material will bring the deflection from ~ 40 μm to 10 μm, still leaving

enough thermal isolation for the pixel to be effective as a pyroelectric detector. Figure 26 depicts the cross sectional view of the envisioned pyroelectric pixel, both before and after PIP deposition. This illustration shows two of the many interdigitized fingers using basic cantilevers.

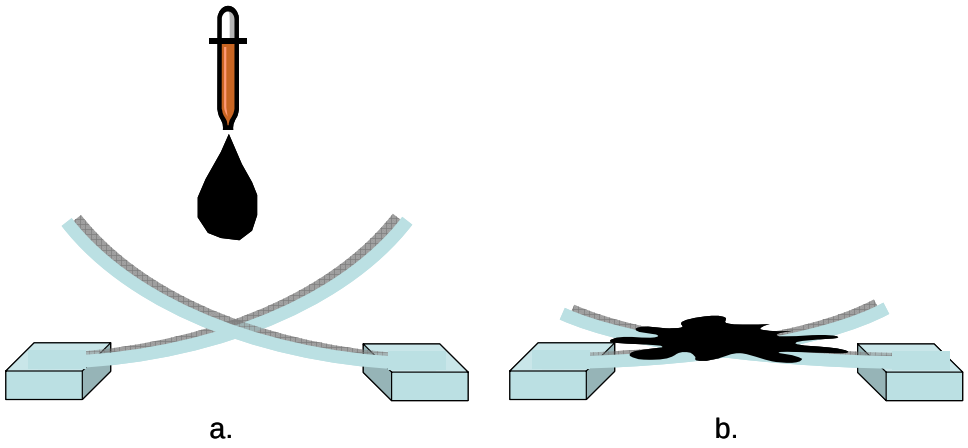

Figure 26: a) An illustration of the pyroelectric structure prior to depositing the PIP material. b) After depositing the PIP material. The structure's initial deflection compensates for the weight of the PIP, but still maintains thermal isolation from the underlying substrate.

The next critical design aspect of the pyroelectric pixel is that it must have interdigitized fingers in order for the novel thermal sensing material to complete the circuit. It is imperative that all current flows through the PIP material. This material is very resistive; therefore, if any two of the interdigitized fingers touch, a short will be created, making the detector dysfunctional. Most pyroelectric designs deposit a conformal layer of material (i.e., TGS, $LiTaO_3$, or PVDF) onto a transparent electrode, which is elevated off the substrate by two structural posts. Another semitransparent electrode will then be deposited on top of the pyroelectric material. Incident radiation will pass through the semitransparent material into the pyroelectric material, ultimately

changing its temperature. Also, in an effort to maximize the absorption of the incident flux, the retro-reflected flux is captured by adding a highly reflective layer to the substrate. Thus, the rays of flux reflect back and forth through the material maximizing absorption and ultimately, output response. Figure 27a is a cross-sectional view of a typical pyroelectric pixel design and Figure 27b depicts a scanning electron microscope (SEM) image of a commercial pyroelectric FPA design.

Figure 28 and 29, illustrate the pixel designs used in this thesis The gap between the interdigitized fingers was to ensure that the fingers never touched after the PIP material was deposited. . Both designs have identical overall dimensions; the major

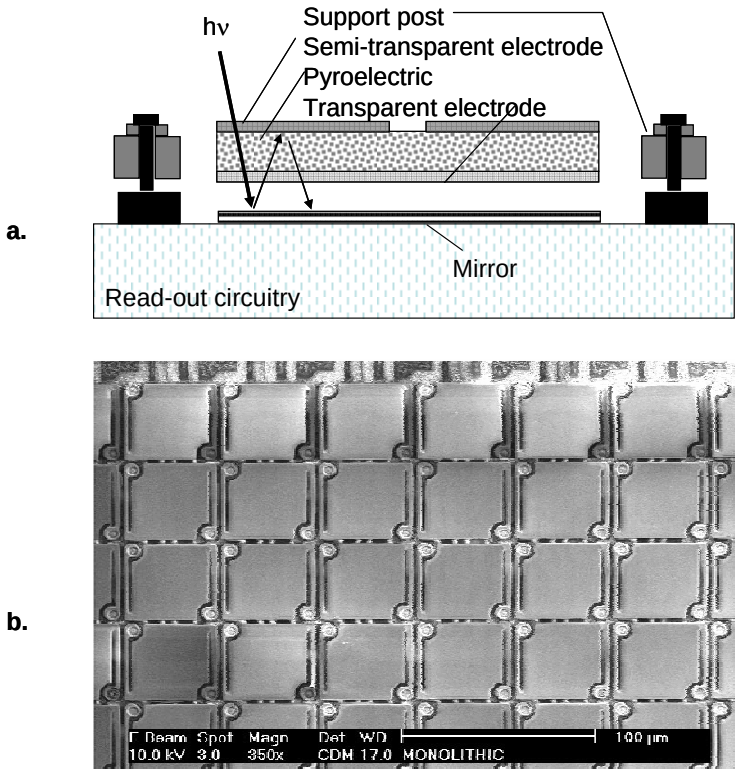

Figure 27: a) A cross-sectional view of a typical pyroelectric pixel. The pixel is thermally isolated from the underlying substrate by the structural posts. b) An SEM image of a portion of 320 x 240 FPA [4].

difference is the number of interdigitized fingers and gaps between the fingers. Figure 28 illustrates the design with 5-μm gaps between fingers, and Figure 29 illustrates the design with 10 μm gaps between the fingers.

Next, the dimensions of the pyroelectric pixels must be large enough to deposit PIP material. The current off-the-shelf pyroelectric detectors have pixel dimensions of ~50 μm x 50 μm. This allows for high pixel density in a small area. The designs of this experiment dwarf the aforementioned off-the-shelf pixels used today. Since inkjet deposition has never been tried before, this proof-of-concept design was made much larger to increase the chance of creating a successful pyroelectric detector design.

The last attribute to be discussed is that the pixels need to have the ability to electrically interact with the outside world. The ultimate goal is to deposit the PIP material onto the pixels, wire bond to a 24-pin chip carrier, and insert this chip into a bread-board for testing and characterizing the PIP material as a viable thermal sensing material. In order to make this possible, the MEMS structure must have bonding pads. Typical bond pad sizes are on the order of 100 μm x 100 μm. However, for the designs of this experiment, the pads were once again made larger to ensure that wire bonding was possible. The bond pads for this PolyMUMPs run were 300 μm x 300 μm to ensure connection from the micro to macro worlds was possible. Also, a typical industry standard places bond pads around the outside of the MEMS device and pixel wiring is done with a maze of addressing lines using Poly-2/gold. This alleviates any shorting that may occur when trying to wire bond across the device. Figure 30 illustrates the MEMS pixels that were used in this thesis.

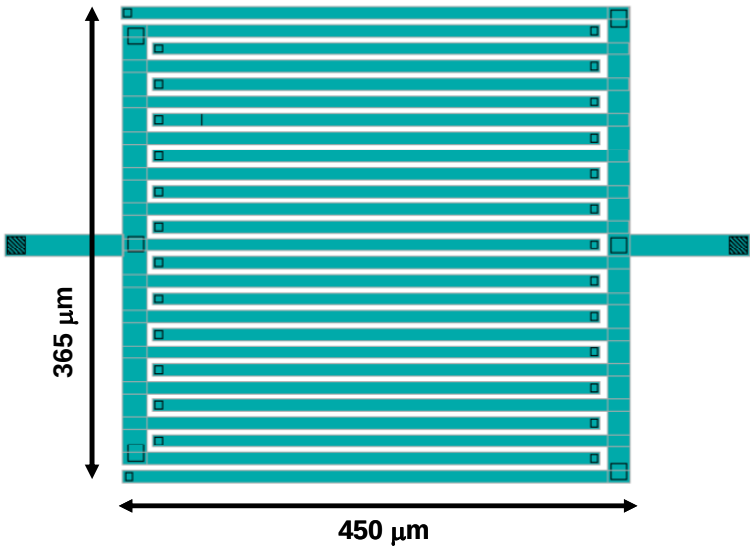

Figure 28: Pyroelectric design with 5 µm gaps between the interdigitized fingers. There are a total of 28 fingers, with widths of 10 µm, in this design that will support the PIP material**.**

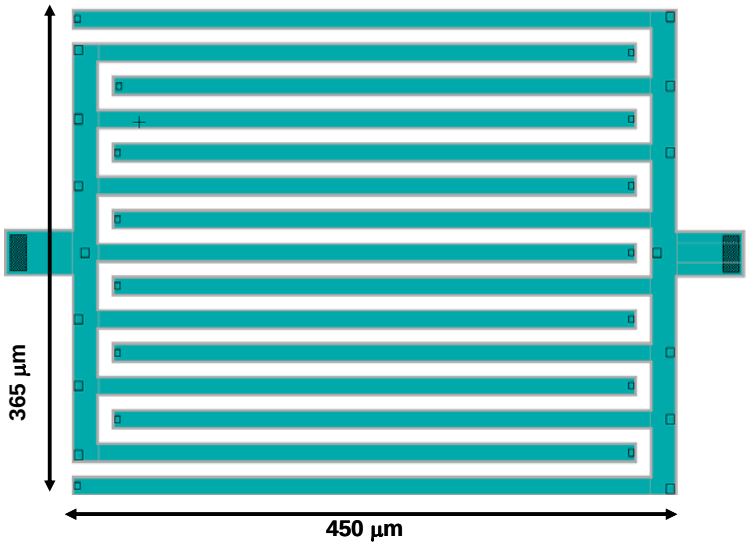

Figure 29: Pyroelectric design with 10 µm gaps between the interdigitized fingers. There are a total of 15 fingers, with widths of 15 µm, in this design that will support the PIP material.

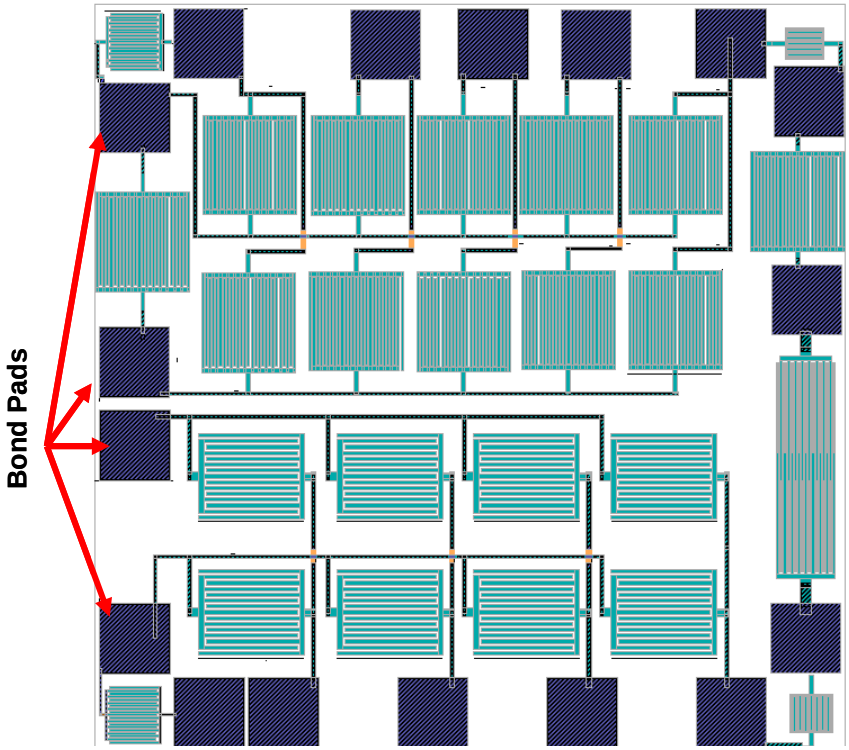

Figure 30: An illustration of the use of bond pads. This allows for the micro to macro connection.

3.3.1.1 Deflection Theory of Bimaterial Micro-cantilevers

When a single cantilever beam is composed of two different material layers, the elongation and contraction differences in the two materials result in either an upward or downward deflection [5]. When the temperature changes, bimaterial microcantilevers undergo bending due to the dissimilar thermal expansion of the two different materials used in the cantilever. This phenomenon is frequently referred to as the "bimetallic effect."[6]. In the PolyMUMPs process, the thin gold film is deposited onto the Poly-2 layer at temperatures ranging between 333-383 K [7]. When the MEMS sacrificial layers are removed, the structures are released, and exposed to room temperature, ~ 300 K. This difference in temperature results in contraction. Due to higher coefficient of thermal

expansion (CTE) of gold, the gold layer contracts more than the Poly-2 layer, resulting in an upward deflection of the bimaterial beam [5].

An illustration of this deflection theory using bimaterials, namely Poly-2_gold, was shown in Figure 25. The main engineering control in exploiting the deflection is length. Since the materials used were limited to the PolyMUMPs foundry, the only user control is design dimensions. It is evident from Figure 25 that by maintaining the same width, the amount of deflection will be increased by increasing the length of the cantilever beam.

The material properties of the PolyMUMPs foundry will now be discussed. Only the materials used in the pyroelectric pixel design described in this thesis will be discussed. Table 3 gives all of the material properties needed for the bimaterial deflection calculations. It must be noted that the values seen with (**), are parameters that vary from run to run within the PolyMUMPS foundry. The other parameters must be experimentally found, but can be retrieved from many of the MEMS published papers.

The deflection derivation of a bimaterial beam can be found in many published articles, with a good description in [5], and therefore, will not be shown here.

Table 3: PolyMUMPs run 71 material properties**.**

Material Property	Poly 2	Gold
Film thickness [μm]**	1.5062	0.5111
Residual stress [MPa]**	-7.3	23.62
Youngs Modulus [GPa]	161	74
Coefficient of Thermal Expansion [K^{-1}]	2.33×10^{-6}	14.3×10^{-6}
Poisson's Ratio	0.23	0.44

The bimaterial deflection is given by

$$z = \frac{3t_{gold}\sigma_{res}L^2}{E'_{poly}t_{poly}^{\ 2}}, \tag{45}$$

where t_{gold} is the thickness of the gold, L is the beam length, t_{poly} is the thickness of the polysilicon (Poly 2 layer), E'_{poly} is the biaxial modulus for polysilicon, which is derived from Young's modulus (E_{poly}) and Poisson's ratio for polysilicon (ν_{poly}) and is expressed as

$$E'_{poly} = \frac{E_{poly}}{1-\nu_{poly}}. \tag{46}$$

The residual stress, σ_{res}, is composed of both the residual stress of the polysilicon, σ_{poly}, the thermal stress between the Poly 2 layer and the gold layer, σ_{therm},

$$\sigma_{res} = \sigma_{poly} + \sigma_{therm}. \tag{47}$$

The thermal stress, σ_{therm}, is due to the fact that gold and polysilicon have different CTEs and the gold is evaporated at a higher temperature than room temperature [5]. Thermal stress is defined as

$$\sigma_{therm} = E'_{gold}\left(\alpha_{poly} - \alpha_{gold}\right)\Delta T \tag{48}$$

where E'_{gold} is the biaxial modulus for gold, and both α_{poly} and α_{gold} are the CTEs for both polysilicon and gold, respectively, and lastly, ΔT is the change in temperature between the gold deposition and room temperatures,

$$\Delta T = T_{room} - T_{fab}. \tag{49}$$

The deflection for the bimaterial cantilever can then be solved by placing Equations (46) through (49) back into Equation (45) to give the result shown in Equation (50) , which can be used to solve the deflection for a bimaterial cantilever beam of any given length,

$$z=\frac{3t_{gold}\left(\sigma_{poly}+\frac{E_{gold}}{1-\nu_{gold}}\left(\alpha_{poly}-\alpha_{gold}\right)\left(T_{room}-T_{fab}\right)\right)L^2}{\left(\frac{E_{poly}}{1-\nu_{poly}}\right)t_{poly}^{\ 2}}. \qquad (50)$$

3.3.1.2 CoventorWare Modeling

CoventorWare is an integrated suite of tools designed to produce accurately modeled MEMS [7]. This modeling tool is the key to success when a proof-of-concept is being designed. Prior to spending the money for design runs or fabrication costs, this software tool allows the user to model and simulate MEMS structures in any given environment. For the two interdigitized designs used in this thesis, CoventorWare was used to optimize all of the design specifications inherent in a well-performing pyroelectric device.

Fortunately, the PolyMUMPs foundry's layer structures are loaded into the software package. This means that all the specifications on thickness, Young's modulus, stress, strain, etc. for all applicable layers, SiN, Poly-0, Poly-1, Poly-2, gold, and both oxides are preloaded. There are some typical parameters that vary from run to run in the PolyMUMPs process, such as the layer thickness and strain. Due to this fact, it is a standard procedure to calibrate CoventorWare to experimental data from a particular run. For example, the pyroelectric pixel designs described in this thesis were created in

PolyMUMPs run 72. Therefore, in this design, five Poly-2/ gold cantilevers were designed along with the pyroelectric designs.

These microcantilevers were tested using an interferometric microscope (IFM) made by Zygo. Interferometry is a traditional technique in which pattern of bright and dark fringes result from an optical path length difference between a reference and a sample beam. The incoming light is split inside an interferometer, one beam going to an internal reference surface and the other to the sample. After reflection, the beams recombine inside the interferometer, undergoing constructive and destructive interference and producing the light and dark fringe patterns. A precision stage and a CCD camera together generate a 3D interferogram of the object that is stored in the computer memory. This 3D interferogram of the object is then transformed by frequency domain analysis into a quantitative 3D image providing surface structure data [8]. The image produced coupled with Zygo's software allows the user to measure accuracy down to 10 nm in x, y, and z axes. Figure 25 showed five Poly-2/gold cantilevers used to calibrate the CoventorWare software. The IFM-measured z-deflection data from these multi-length structures allowed for calibrating the Coventorware software to the experimental results. By varying some of the controllable parameters, the output of ConventorWare can be matched to the experimental data from the simple cantilever structures. This software tool can then be used to model structures that use the Poly-2/gold materials. Once calibrated, CoventorWare was used to model the two MEMS pyroelectric pixel designs. Figure 31 (a and b) illustrate these two CoventorWare modeled pyroelectric pixel designs.

a.

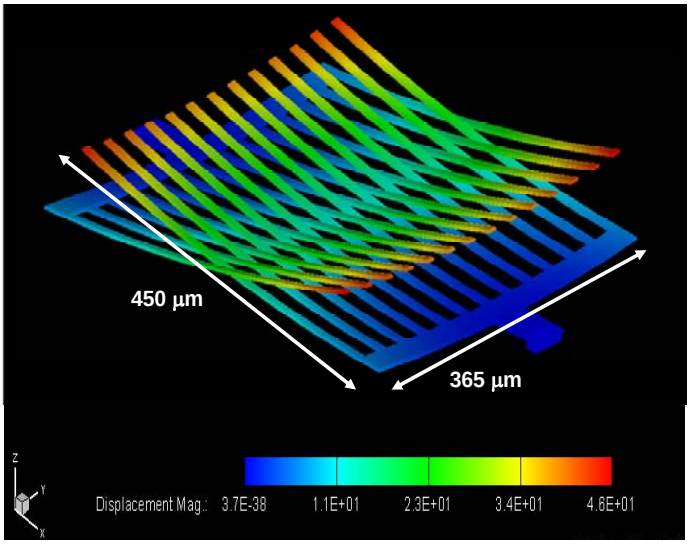

b.

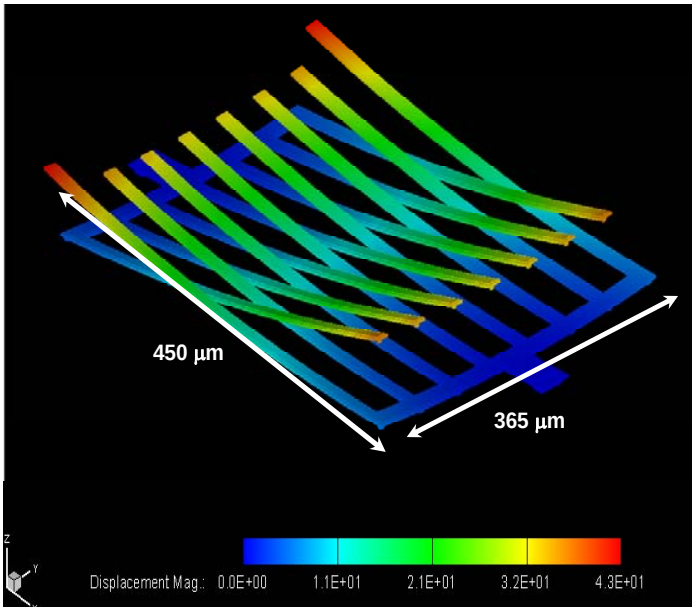

Figure 31: a) A Coventorware model of the small-gaps pixel design. This structure deflects up to ~ 46 µm. b) A model of the large-gaps pixel design. This structure deflects up to ~ 43 µm.

3.3.1.3 Experimental Results on Bimaterial Deflection

Once the PolyMUMPs structures were released, the deflection height measurements were taken. The term "releasing" is often used in MEMS literature in order to explain the removal of the sacrificial layer. The same testing that was done to

the cantilever structures used in the calibration of CoventorWare was also done on the pyroelectric structures. The Zygo is once again employed to measure the deflection height in the pixel designs. Figure 32 is a screen shot of an image taken from Zygo's 3D imaging software. The main discrepancy when using the Zygo for this magnitude of deflection is that the retro-reflected beams will not propagate to the interferometer. The angle is too great to capture all these reflected beams, which results in a less-than-desirable image

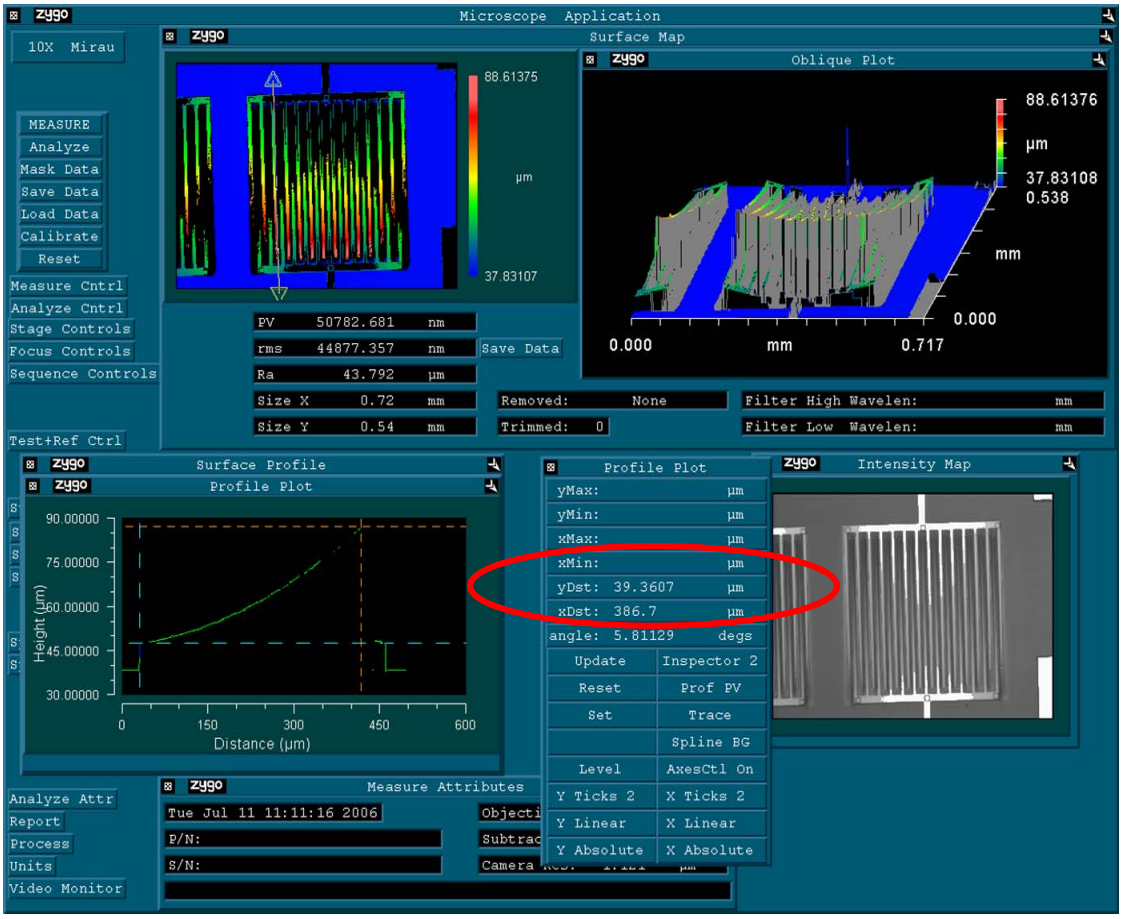

Figure 32: Image from Zygo's IFM that depicts deflection characteristics of pixel design. The max deflection is seen in the "yDst" parameter shows ~ 39.36 µm.

quality. The experimental results from the Zygo give a good estimate into the magnitude of deflection the pixels have.

A second method in determining the amount of deflection in the pixels is by using a microscope with a micrometer adjustable focus (z-axis movement). By bringing different parts of the structure into focus and taking readings on the amount the z-axis stage micrometer moved, an accurate deflection can be measured. This method must also be calibrated prior to assuming each tick mark on the focus control is 1 μm. This was done using an unreleased MEMS structure, which has a thickness of 675 μm (measured with a micrometer). The chip was then placed on the microscope's stage. The stage was first brought into focus and the z-axis micrometer was read. The top of the unreleased MEMS structure was then brought into focus and the z-axis micrometer was once again read. The difference between these two readings resulted in ~ 676 μm. This confirmed that each tick mark on the microscope's micrometer did, in fact, represent 1 μm, and could be used for the deflection measurements on the pixel designs.

Using the aforementioned methodology, the deflection from the pixels was found to be ~ 39.8 μm. Figure 33 illustrates an image of the small-gap pyroelectric pixel. Notice the anchor of where the Poly 2 is adhered to the substrate is in focus, and the tips of the cantilevers are out of focus. This difference was measured using the methods described above.

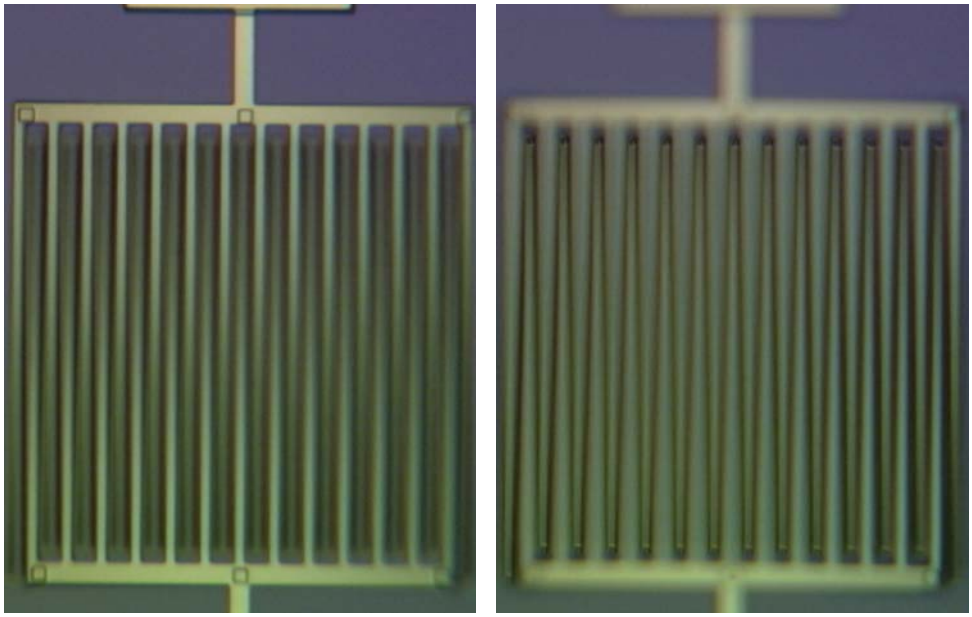

a. b.

Figure 33: An image of the small-gap pyroelectric pixel demonstrating the focusing technique to measure deflection height. a) The microscope is focused on the anchor adhering the structure to the underlying substrate. b) The micrometer z-axis stage height is then rotated to bring the tip of the structure into focus. The amount of micrometer rotation is the deflection height, which was found to be ~ 39.8 μm.

3.3.1.4 Comparative Analysis

This section will be dedicated to comparing the results described in the previous sections. A comparative analysis will be performed on the pixel's deflection using analytical equation predictions, CoventorWare simulated results, and the experimental measurements. All variables needed to solve Equation (50) are either design parameters or fabrication parameters. Table 4 gives a clear description into the value and units given to each variable. These variables were inserted into Equation (50) to give the analytical prediction for deflection. The resulting deflection was found to be $z = 32.2\ \mu m$. It is of critical importance to note that that the derivation that led to Equation (50) did not include the width in either the Poly-2 or gold cantilevers. If the gold is deposited over the

entire width and length of the cantilever, it will cause maximum deflection. This consideration is not taken into account in this derivation. Equation (50) assumes that the length far exceeds the width, which can be neglected.

Table 4: Variables with respective values and units used in Equation (50).

Variable	Value	Units
t_{gold}	0.511	μm
σ_{poly}	-7.3	MPa
E_{gold}	74	GPa
υ_{gold}	0.44	N/A
α_{poly}	2.33×10^{-6}	K^{-1}
α_{gold}	14.3×10^{-6}	K^{-1}
T_{room}	300	K
T_{fab}	333	K
L	400	μm
E_{poly}	161	GPa
υ_{poly}	0.23	N/A
t_{poly}	1.5026	μm

The modeling of the pyroelectric pixels in CoventorWare will now be discussed. As previously described, CoventorWare needed to be calibrated prior to getting accurate results. The only parameter to be varied when trying to calibrate CoventorWare to match the experimental results performed on the cantilever beams was the residual stress of the gold. An enumeration was performed that varied this parameter giving multiple results of deflection on the modeled pixel. The result that matched the experimental data was used. This residual stress value was then changed in the material properties of CoventorWare. All future simulations could then give calibrated results to a particular PolyMUMPs run.

The results for the modeling were shown in Figure 31. Because the experimental results were only performed on the Figure 31a device (smaller gaps design), it will be the

only structure re-addressed in the comparative analysis. The displacement results shown in Figure 31a, once again were found to be $z = 44.6\ \mu m$.

Lastly, the experimental results were found using Zygo's IFM. These results were also confirmed using the aforementioned focal plane measurement. The experimental data showed a deflection of $z = 39.8\ \mu m$.

All of the comparative results found can be seen in Figure 34. It is evident that a precise method of measuring the deflection of the pixels has yet to be determined. The analytical expression lacks the width of the structure, which can cause large standard deviation. The CoventorWare model only alters one of the many variables it uses in the algorithm to solve for deflection. This also gives a large standard deviation in the results. Lastly, the experimental results were found with two different methods producing similar results, which are considered the most accurate deflection results. More accurate analytical prediction calculations need to be researched. It is evident that it is important to find a solution that incorporates the width of the cantilevers. This would more accurately be able to predict the results and give a closer comparison between both the CoventorWare and experimentally measured results. The deflection distance between the modeled and experimentally measured is fairly close. The minute differences can be accounted for due to CoventorWare's calibration technique. There are many variables that could be tweaked to try to emulate experimental results. This effort is beyond the objective of this thesis. CoventorWare is a modeling tool that is used to give good approximations toward device development.

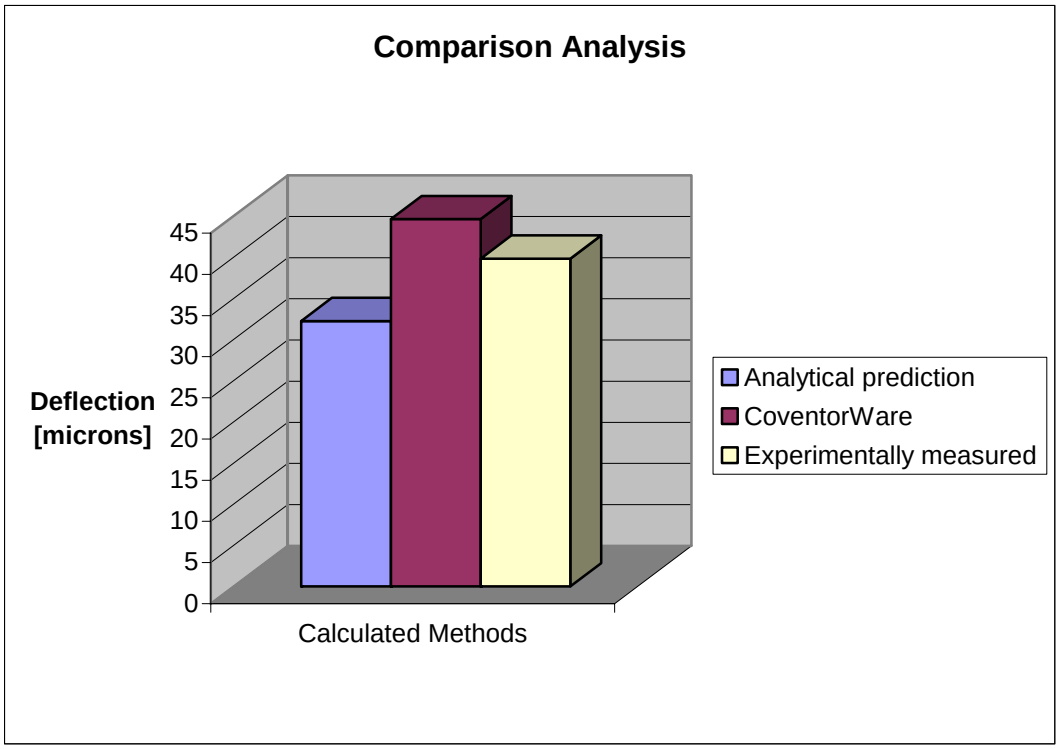

Figure 34: A comparative analysis illustration of the three methods described in this section**.**

The pixel design was analyzed to ensure that enough thermal isolation was attained to compensate for the deposition of the PIP material. The design requirements for the pixels: thermal isolation, interdigitized fingers for the material deposited to complete the circuit, large enough for untried ink jet deposition, and lastly, the electrical connections, were achieved and described in this section. Now that the pixels that will be supporting the PIP material have been discussed, it is time to better understand the deposition method used to micro-dispense minute volumes of the PIP material onto the MEMS pixels.

3.3.2 The Deposition Method

This thesis topic follows-on the researchof a previous student [9]. One lesson learned from previous research was that a deposition method was needed. The PIP material's viscosity is a bit thicker than water and the PIP dries very fast. The previous deposition method used was spincoating the PIP material onto a released MEMS structure. This method coated everything, to include address lines and bond-pads, which did not allow for individual pixel testing. An image of the results of spincoating PIP onto a MEMS structure is shown in Figure 35. It is evident from Figure 35 that a newly devised deposition technique was needed in an effort to dispense the PIP onto individual micron-scaled pixels. A solution to this problem was created by AFRL/MLPJE, which is

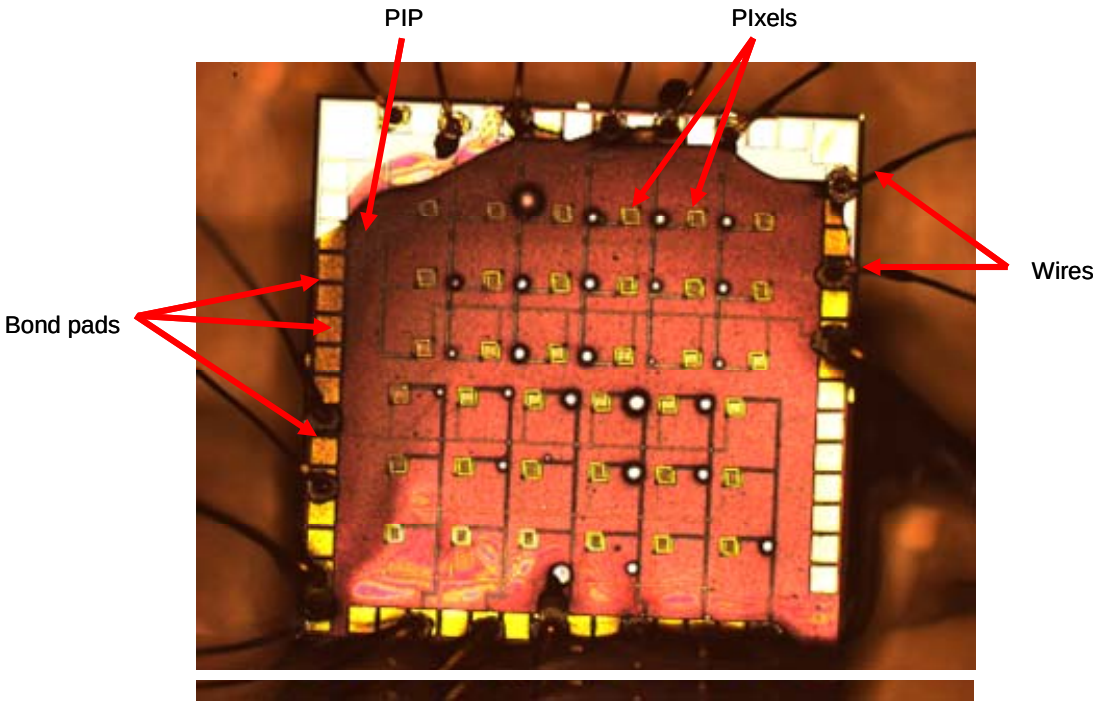

Figure 35: A post-deposition image of PIP on a MEMS structure. The material was spin-coated and didn't allow for pixel to pixel characterization. Also, this deposition method negated the micron-scale effort [9].

inkjet deposition, and will be discussed in this section of the thesis. The inkjet deposition system will first be discussed, followed by PIP droplet characterization. A thorough understanding into both droplet surface area and droplet thickness is critical in order to characterize PIP on a MEMS pixel.

3.3.2.1 The Inkjet System

MicroFab Technologies, Inc. is one of the leading developers for microdispensing and precision printing using inkjet technology [10]. At the onset of researching an ideal deposition method, MicroFab was contacted for guidance. The result of the consultation was the creation of an inkjet deposition system that allowed for printing accurately to MEMS structures using various aqueous solutions. The inkjet system assembly used to deposit material in this thesis is shown in Figure 36.

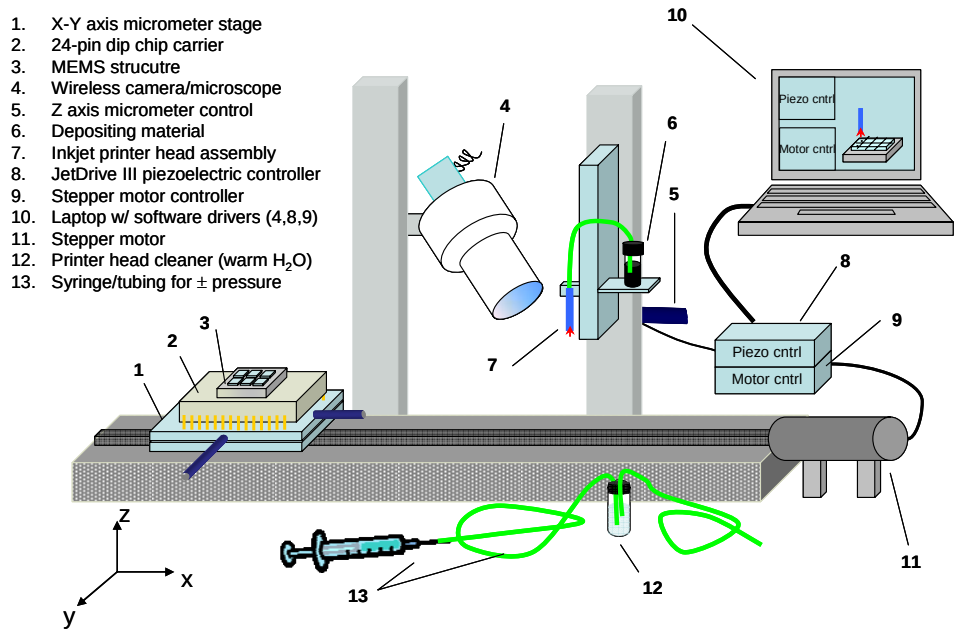

Figure 36: Inkjet deposition system used to dispense micro-droplets of material onto the MEMS pixels in this thesis.

The deposition system shown in Figure 36 was created by AFRL/MLPJE using some key parts from MicroFab (i.e., inkjet printer head and JetDrive III controller). The inkjet printer head assembly is critical to successful micro-deposition. The basic construction of this piece is a cylindrical glass tube drawn to an orifice of 30 – 60 μm in diameter. This tube is encased with a piezoelectric actuator and mounted into a metal housing that provides mechanical protection and support. An image of the inkjet printer head assembly provided by MicroFab is shown in Figure 37. As described in the background of this thesis, when a piezoelectric material is biased, it will compress, and when the bias is removed, the material expands back to its original state. In an effort to squeeze micro-droplets out of the printer head, a voltage pulse is used. By varying the parameters of this voltage pulse, various materials can be deposited. This voltage pulse, with all applicable user-controlled parameters, is shown in Figure 38.

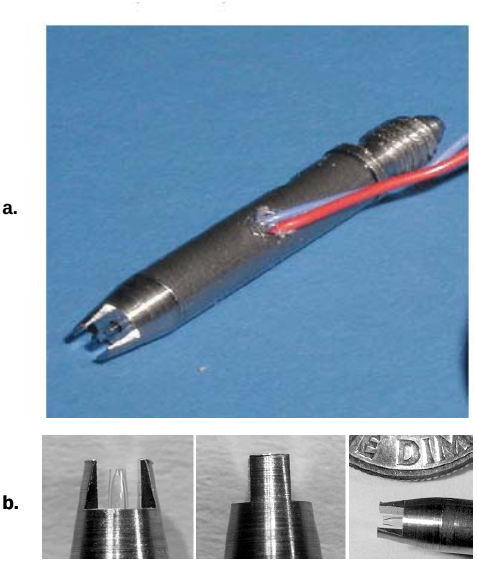

Figure 37: MicroFab's inkjet head, model MJ-AT-01, that was used in this thesis to deposit the PIP material. a) An image of the complete inkjet printer head assembly. b) A magnified image of the glass orifice (30 μm in diameter). [10].

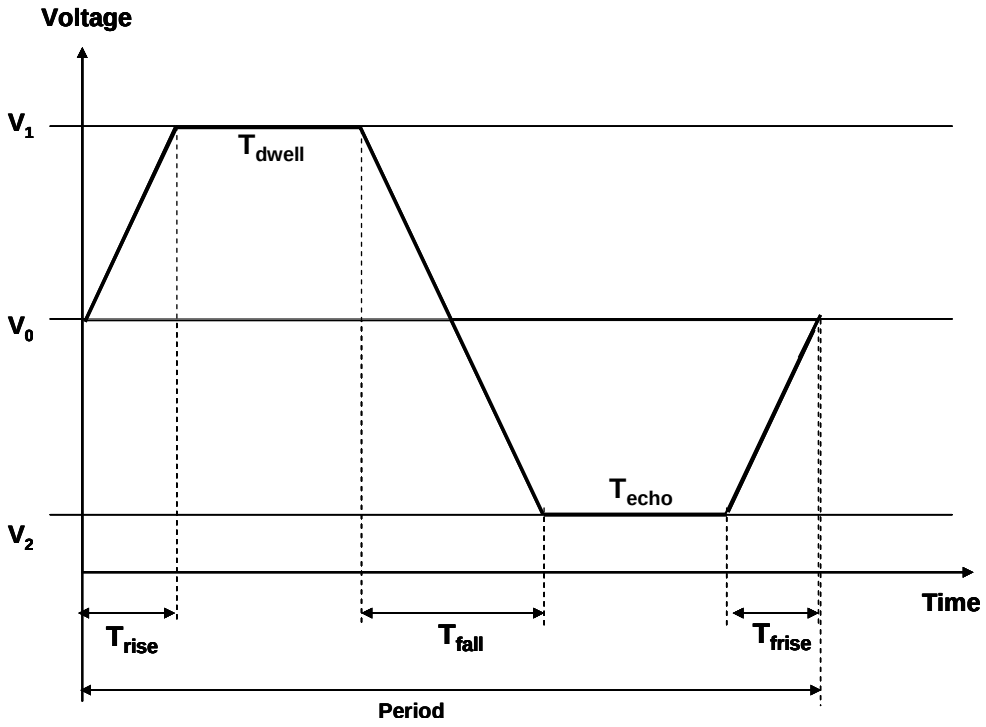

Figure 38: A unipolar pulse that is typically used to control the material deposited through the inkjet printer head. The printer head is encased with a piezoelectric material that when biased dispenses single micron-size droplets [10]. These time parameters are the process variables for depositing different materials.

Finding the ideal parameters for a particular material using this voltage pulse is an important and tedious process. In order for the inkjet printer head to print accurately targeted droplets to pixels, an unperturbed output stream is required. This process must be done daily because parameters found on one day may not be the same on the next. All of the probable output fluidic streams that are encountered when changing the parameters of the voltage pulse can be seen in Figure 39. The desired output stream is shown in Figure 39c. In an effort to achieve this objective, an iterative process of changing the variables of the voltage pulse was accomplished. Also, it must be noted that the JetDrive piezoelectric controller has both an internal and external trigger. With the internal trigger

mode, a continuous triggering allows for an output stream of fluid in lieu of a single droplet. To print droplets, the external triggering mode is used, which is controlled by the stepper motor. When the motor is at a key location, a trigger is sent to the JetDrive III and a single droplet is dispensed. Therefore, once the ideal fluidic stream is achieved, using the internal triggering, just prior to printing to a pixel, the triggering mode is quickly switched to external to dispense droplets to key locations on the MEMS structure.

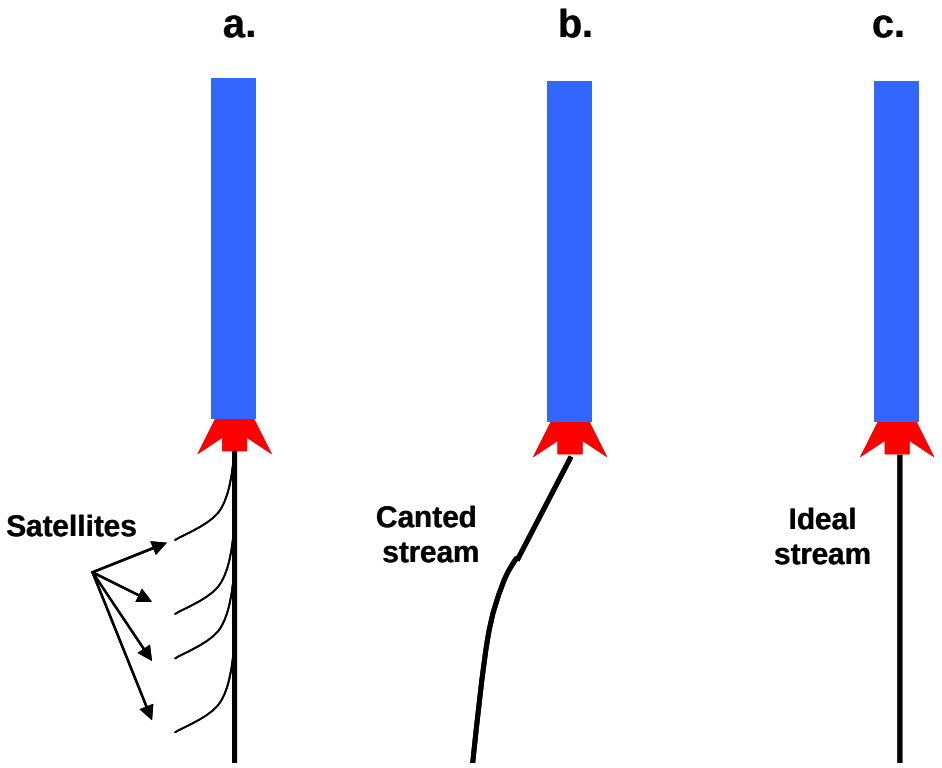

Figure 39: An illustration of the probable output fluidic streams seen when depositing materials through the inkjet printer head. a**)** This output stream creates small unwanted satellite streams when the parameters V_1, V_2, and frequency are not set correctly adjusted. b) A canted output fluidic stream is typically seen when T_{rise} and T_{fall} are not properly set. c**)** The ultimate goal is the ideal stream.

Once the aforementioned output steam is attained, the stepper motor is engaged and the x-y micrometer stage that holds the MEMS structure moves in the x-direction toward the inkjet print head. A program written in visual basic controls both the external triggering of the piezoelectric controller and the x-axis translation, allowing for droplet control. Again, a description of this control is best depicted using a figure. Figure 40 is an illustration on the capabilities of the visual basic program. This program gives the user the ability to control the number of droplets produced in a row, which is defined as a line. In the case of this thesis, a line is essentially a pixel. The line spacing is the gap between each pixel, and the number of times droplets that are dispensed on top of one another is a layer. This basically controls the thickness of the material deposited.

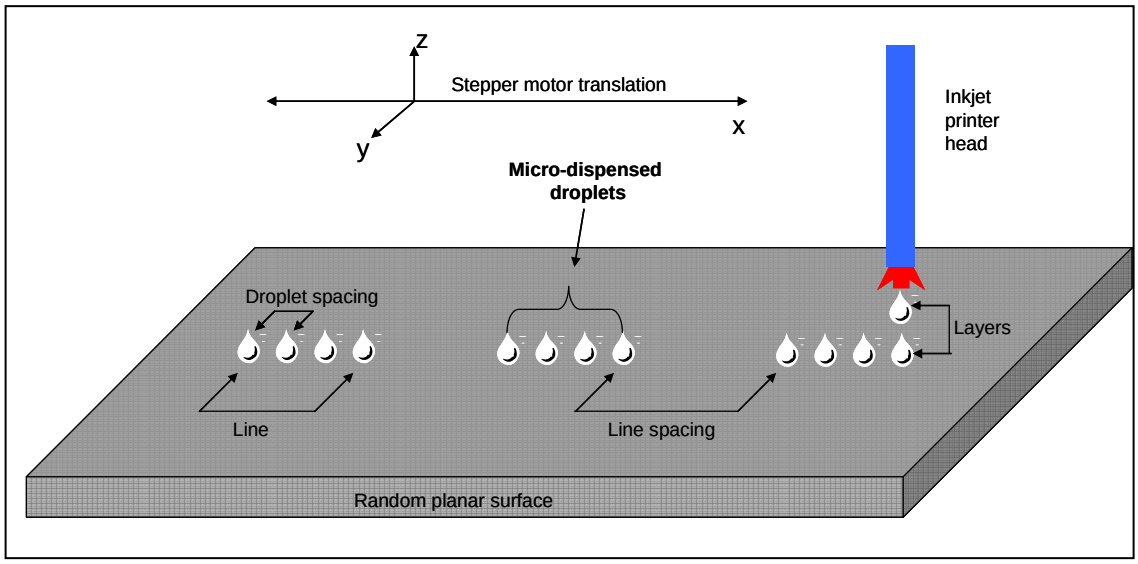

Figure 40: A visual depiction of the user-controlled parameters of the visual basic program. The stepper motor only translates the stage that holds the MEMS structure in the x-direction. The user has control over the number of droplets in a row (line), the spacing between lines, and lastly, the number of layers (thickness).

Printing to individual pixels was designed around this pre-existing program, which led to some fine-tuning modifications. Since the stepper motor only controlled printing in the x-direction, a modification was needed to allow for fine-tuning user control in both the x and y directions (x-y micrometer stage). By monitoring the microscope image of the deposition process, the user can calibrate the precise impact location of the droplets. Now that the system used to deposit the droplets has been discussed, the next logical step is to characterize the droplets produced by this deposition system. The next section is dedicated to analyze the accuracy, quality/dimensions, and topography of the inkjet-deposited droplets.

3.3.2.2 Inkjet Droplet Characterization

This section's objective is to analyze the performance of the inkjet deposition system used in this thesis. Once the ideal stream (shown in Figure 39c) is attained, the stepper motor controller is engaged using the visual basic program. The stage that supports the MEMS structure now moves towards the inkjet head. Also at this time, the triggering is switched to external, so that individual droplets can be dispensed. To properly characterize the inkjet deposited droplets, a cleaned silicon surface (acetone bath/nitrogen dried) was used as the targeted object. In this section, the accuracy of the deposition system, the quality/dimensions of the droplet, and the topographic landscape of the droplet will be analyzed.

The deposited droplet accuracy is critical to the success of this thesis. Therefore, a complete understanding of how accurate the visual basic program that controls the dispensing of a droplet in a specific location will be investigated. This effort will be

accomplished using an Optronics digital camera and a KLA-Tencor profilometer. The parameters, shown in Figure 40, controlled by the visual basic program, were varied to ensure the system could precisely deposit droplets where and when the software commands instructed. Distance between droplets and layer numbers (droplets on top of one another) were two of the main parameters that were varied. Figure 41a illustrates a microscope image of a 1000 μm line width with droplet spacing of 200 μm. Figure 41b shows the cross-sectional profile of the droplet image seen in the adjacent photo. The profilometer measures a thickness in microns vs. the distance traversed using the stylus of the profilometer. It is evident that the locations of the droplets as dictated by the visual basic program are fairly accurate. The gaps between the droplets are seen on average to be ~ 200 μm in separation. An error analysis for the amount of variance between what the program said would happen to what actually was measured is beyond the scope of this thesis. Since the pixel dimensions are large, perfect accuracy is not needed and can be the focus of further research.

The thickness generated from subsequent droplets is another analysis that can be done from Figure 41b. It is evident from the profile that the droplets have a coffee ring effect (thicker on the edges than in the center). This will be analyzed in more detail with the use of an AFM and IFM. On average, the thickness at the center of the droplet increases by 0.25 μm with each droplet. Also, the droplet accuracy for each layer does not change the individual droplet diameter by a noticeable amount. The thickness results are best analyzed using the other aforementioned imaging tools.

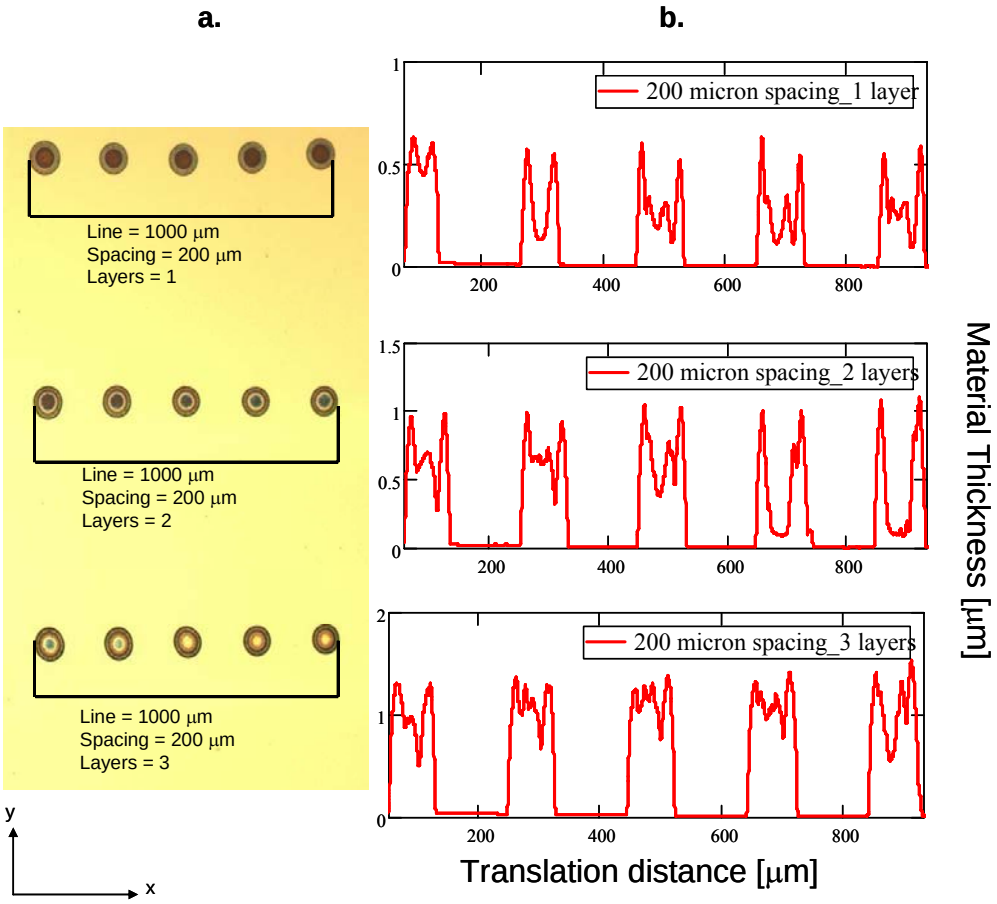

Figure 41: a) Microscope photograph of 200 μm spaced droplets. Image was used to prove the accuracy of droplet spacing and accuracy of subsequent droplets dispensed onto one another forming a layer of material. b) Associated profilometer plot depicting the cross-sectional of the droplets.

The quality of the PIP droplets is the next topic of discussion. The diameter of a single droplet is best shown with an AFM image and is illustrated in Figure 42. A Digital Instruments Mulitmode AFM (Nano-scope IIa controller) was used to capture droplet images. The droplet shown in this image has three layers. The diameter was found to be ~ 145.73 μm, and although there are multiple layers, the droplet maintains a circular shape. This demonstrates the precision of the inkjet depositing system for adding

subsequent droplets. The coffee ring effect is very evident from the topographic image shown in Figure 42b. Ideally, a uniform layer would be deposited, but because the splashing effect is inherent in ink-jetted droplets, coffee ring topography is seen. The solution to mitigate the coffee ring effect is to increase the evaporation rate of the solvent upon droplet deposition on the surface, minimizing the splash wave that propagates, and hence eliminating the coffee-ring [11]. The thickness around the edges of the droplet was measured to be 1.5 μm, and the center, 0.75 μm. Also, the diameter of the three-layer droplet was found to be ~ 145.73 μm.

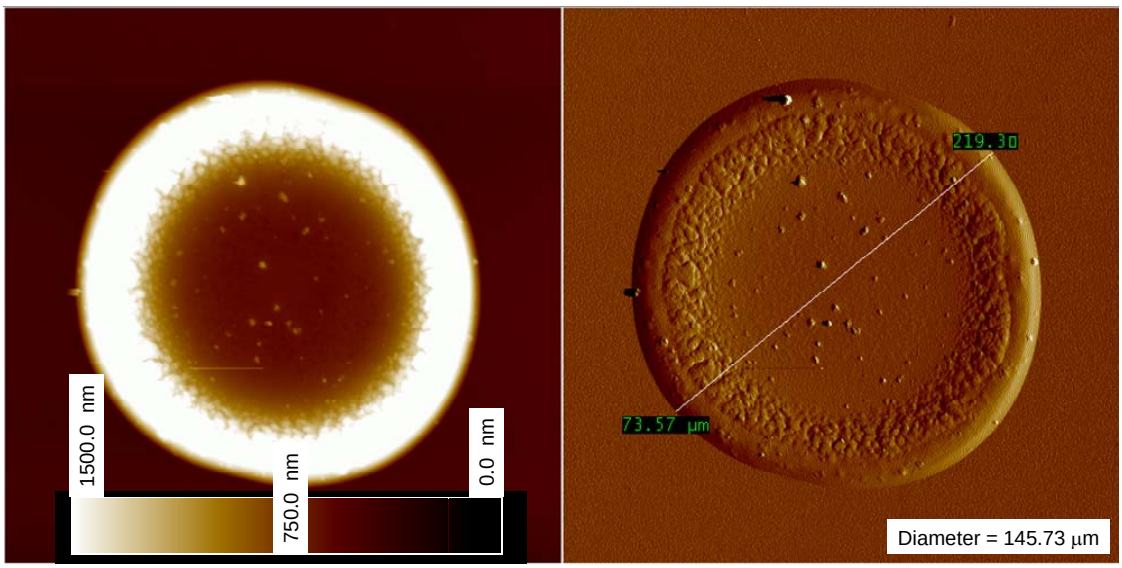

a. **b.**

Figure 42: An AFM image of a single droplet with three layers depicting the coffee ring effect. It is evident from the image that the targeted precision of the 2nd and 3rd droplet was extremely accurate because the droplet didn't change its circular shape. a) The thickness around the edges of the droplet is ~1.5 μm, while the center was found to be ~ 0.75 μm. b) Topographic image - the diameter of the droplet was found to be ~ 145.73 μm.

The thickness can be determined from the AFM image shown in Figure 42b, but is best seen by white light interferometry. Using a Wyko NT 1100 optical profiler, the thickness of the three layers could be analyzed. This image is shown in Figure 43, where again the coffee ring effect is seen. The thickness around the edges was found to be ~ 1.5 μm and the center, ~ 0.25 – 0.4 μm.

In comparison to the spin-coat method, where everything is covered in the deposited material, the inkjet deposition method can strategically deposit material to the MEMS pixels. Now that the micron-droplets have been analyzed on a planar surface, the next section will be dedicated to the results that occurred when the PIP was inkjet deposited onto the MEMS structures described in this thesis.

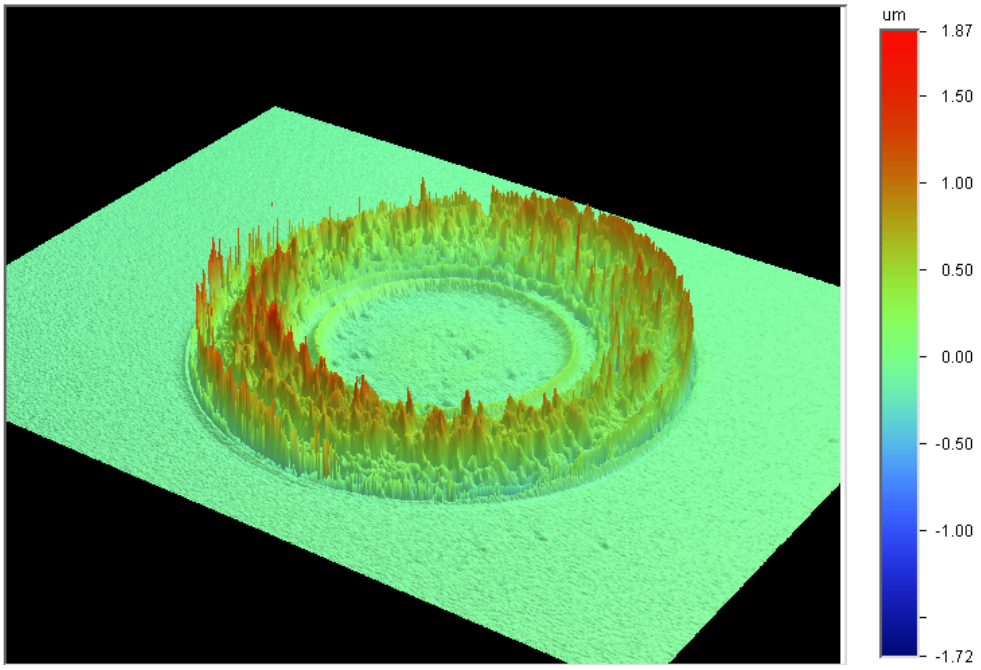

Figure 43: A white-light interferometer image of a single droplet with three layers. This image also demonstrates the coffee ring effect. The thickness around the edges of this three layer droplet is seen to be ~1.5 μm and the center thickness is ~ 0.25 – 0.4 μm.

3.3.2.3 PIP on pixels

At this point, it is necessary to describe how the pixels designed for this thesis were less than ideal. As described in the background, thermal isolation from the underlying substrate is of great importance. This effort enhances the pixel's performance by having the ability to both heat/cool the sensing material quickly. It will be shown that the interdigitized finger designs did not achieve this objective. The material weight far exceeded the ability of the fingers to support the dispensed droplets while still remaining elevated off the substrate. The pixel's lack of thermal isolation did not eliminate the material's response to incident thermal radiation, but did impede it, as will be described in the next couple chapters of this thesis. This section will be dedicated to analyze the pixel's structural shortcomings to support the droplets of PIP and maintain thermal isolation. Also, a discussion on the effective sensing area of the pixel will be conducted, which is critical to being able to compare the PIP pyroelectric pixels to commercial off-the-shelf pixels.

Once the inkjet deposition method was mastered, it was time to print to a MEMS pixel. Initially, a single droplet was printed to a pixel and then analyzed under a FEI/Philips XL 30 FEG ESEM SEM . It was found that a single droplet was not viscous enough to remain on top of the pixel. The goal was for the material to coat between the fingers as to complete a connection between the two sets of fingers. The connection between the sets of fingers is what acts as the sensing area. An SEM image of this single droplet is shown in Figure 44. The original concept when designing the pixels was that one droplet would be thick enough to uniformly cover the pixel fingers and maintain

isolation. It is evident from Figure 44a and b that the thermal isolation is maintained but only stringers of material connect the interdigitized fingers rather than a conformal layer. The result of this investigation led to depositing more than one layer per pixel in order to better control the layer of PIP that completed the connection between the fingers. Unfortunately, this effort completely removed the thermal isolation aspect from the pixel design.

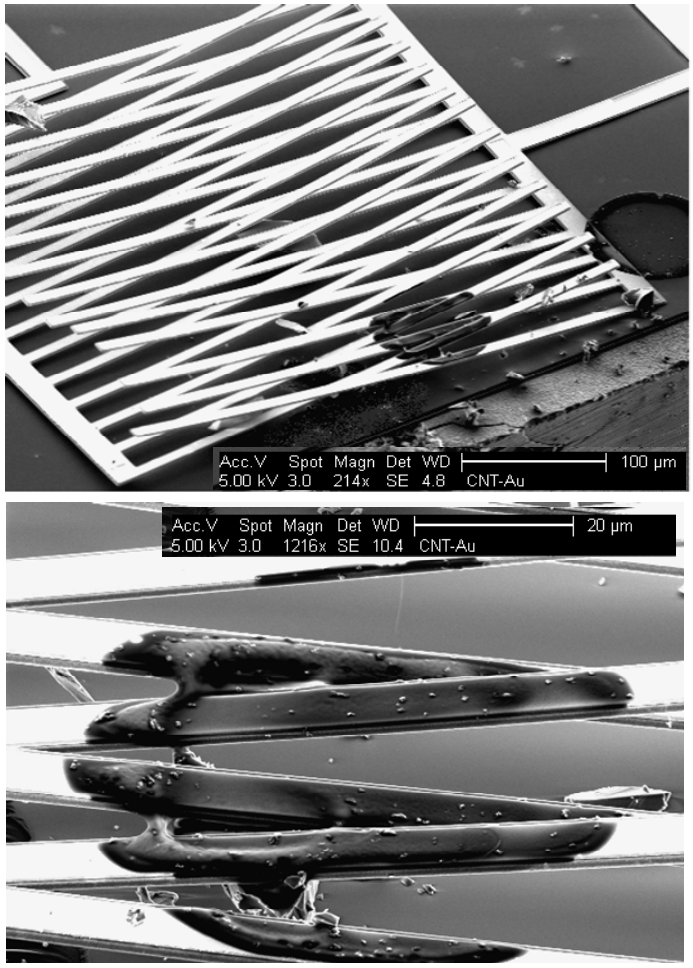

Figure 44: An SEM image of a single droplet dispensed onto the MEMS small-gaps pixel. a**)** 214 x's magnification showing the small droplet with respect to the large pixel. b) A 1261x's magnification zooming in on the droplet. Although thermal isolation is maintained, it is evident that a single droplet isn't viscous enough to uniformly cover the interdigitized fingers.

To illustrate the concept of multiple layers annulling the thermal isolation, another microscope image was taken, as shown in Figure 45. This image demonstrates where deposited PIP adhered the inderdigitized fingers to the substrate, while the locations without PIP still remain thermally isolated.

The last analysis will be finding the effective thermal sensing area. The actual pixels used for FOM testing will be evaluated. Figure 46 shows the inkjet deposited droplet on the pixel used for FOM analysis. Figure 46a illustrates the dimensions of the droplet with respect to the pixel size. Figure 46b shows the up close dimensions of the sensing area used in calculating the surface area. The pixel used was the small-gap pixel previously shown in Figure 28. The sensing area is the entire area

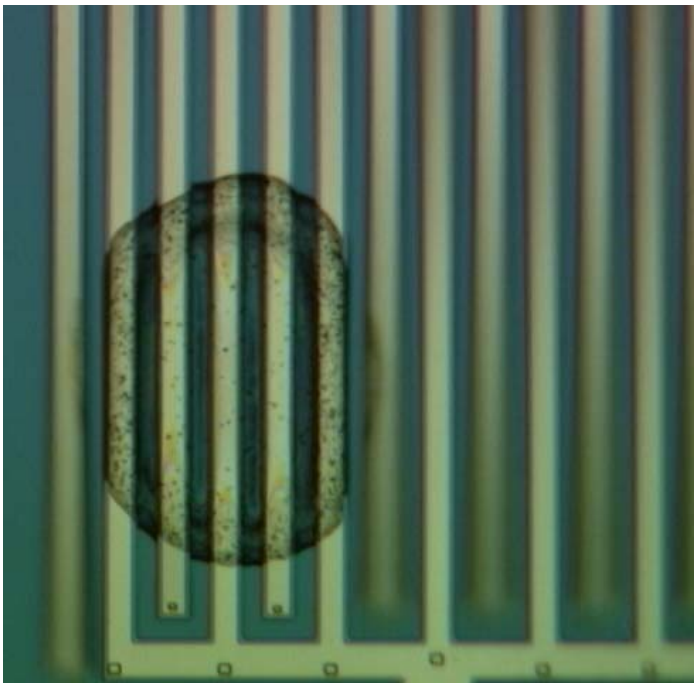

Figure 45: A microscope image illustrating how multiple layers cause the inderdigitized fingers to adhere to the underlying substrate, annulling thermal isolation. The image is out of focus where there is thermal isolation and in focus where the fingers are stuck to the substrate by the PIP material.

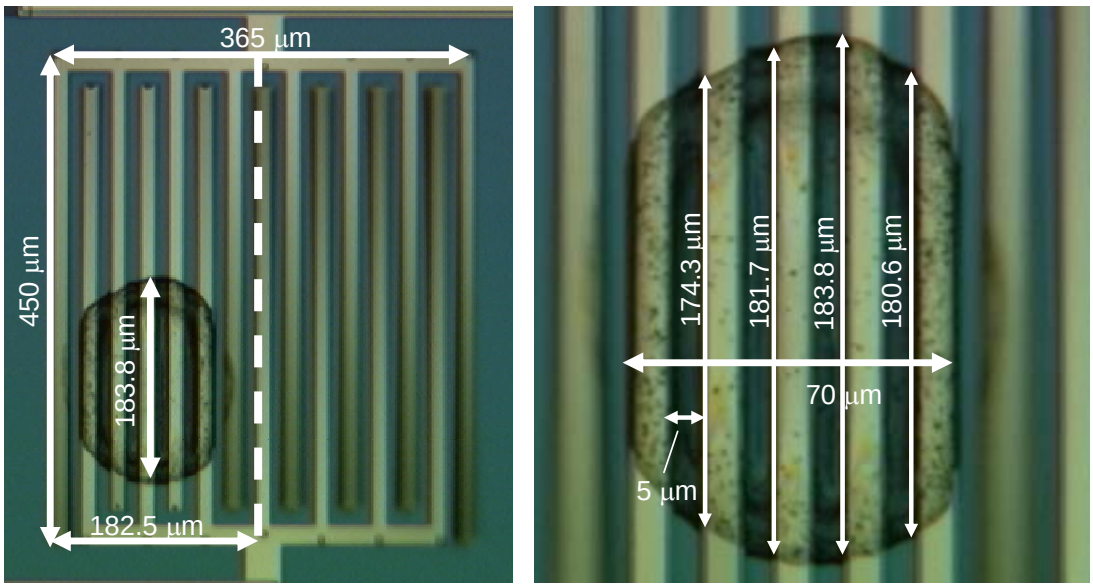

Figure 46: Two images taken by a microscope camera illustrating approximate dimensions of the inkjet deposited droplet (5 layers). This allows for calculating for both the surface area/cross-sectional area of the effective sensing region. a) Photo of the effective sensing area of the PIP with respect to the dimensions of the pixel. b) Magnified image of part a) that was measured using the software of the microscope camera**.**

covered by the PIP material, and will be approximated with an ellipse. The major and minor axes were measured to be 183.8 µm and 70 µm, respectively. The effective sensing area was then calculated to be 1.01 x 10^4 μm^2.

3.4 Chapter Summary

Chapter 3 provided a better understanding into the electrical properties of the thermal sensing material. The mystery of why the resistance continually increased with respect to time when treating the material as a bolometer was solved by finding that current was generated when the sample was heated. This type of detector is pyroelectric,

and led to a confirmation experiment where the sample was tested over a ~ 7-hr timeframe and proved PIP to be a pyroelectric thermal sensing material.

The pixel structural design was then evaluated analytically, numerically, and experimentally to demonstrate the benefits of surface micromachined MEMS structures. The main objective was to maintain thermal isolation after the material was inkjet deposited. The thermal isolation results were then analyzed and compared using three different methods: analytical, numerically, and experimental. A thorough investigation into the inkjet deposition method was then done. The system was first described, followed by a characterization of the droplets onto a planar surface. Once the inkjet deposition system was validated, printing to the MEMS pixels was then performed. This effort showed less-than-ideal results for maintaining the thermal isolation between the interdigitized fingers and the underlying substrate. Depositing multiple layers led to the fingers sticking to the substrate, leaving further research into an ideal pixel design. Now that the samples have been prepared, all of the experiments and test methodologies that were accomplished to give comparable pyroelectric detector results will be discussed.

3.5 Works Cited

[1] Keyword "Materials science," http://www.wikipedia.com

[2] Brott, Lawrence L., Rozenzhak, Sophie, M., "A Poly (vinyl alcohol) / Carbon-Black Composite Film: A Platform for Biological Macromolecule Incorporation." *Advanced Materials*, vol 16, pp 592 – 596, Apr 2004.

[3] Roeder, J.F, et al, "Liquid delivery MOCVD of PLT pyroelectric detectors," *Proceeding of the IEEE*, pp 227 – 230, 1996.

[4] Muralt, Paul, "Micromachined infrared detectors based on pyroelectric thin films," *Reports on Progress in Physics*, vol 64, pp 1139 – 1388, Sept 2001.

[5] Denninghoff, Daniel. *Power scavenging MEMS robots.* MS Thesis. AFIT/GE/ENG/06-17. School of Engineering and Management, Air Force Institute of Tehcnology (AU), Wright Patterson AFB, OH, March 2006.

[6] P.G. Datskos, N.V. Lavrik, "Performance of uncooled microcantilever thermal detectors." American Institute of Physics, vol. 75, pp 1134 – 1148, Apr 2004.

[7] http://www.coventorware.com

[8] http://www.computereq.com, "Zygo New View 100 Maxim GP Interferometer Microscope."

[9] Kaieda, Tetsuo. *Protein Impregnated Polymer (PIP) Film Infrared Sensor Using Suspended Microelectromechanical systems (MEMS) Pixels.* MS Thesis. AFIT/GE/ENG/05-10. School of Engineering and Management, Air Force Institute of Tehcnology (AU), Wright Patterson AFB, OH, September 2005.

[10] http://www.microfab.com

[11] Molesa, Steven, Redinger, David, R. "High quality inkjet-printed multilevel interconnects and inductive components on plastic for ultra-low-cost RFID applications," *Materials Research Society*, vol 769, Jun 2003.

IV. Figure of Merit Analysis

4.1 Chapter Overview

This chapter will be dedicated to provide a detailed understanding of how the FOM calculations were made. In an effort to capture all applicable variables needed in solving the FOMs, both analytical analysis and experimental testing are required. Each section will be devoted to a FOM. A description of how to solve or experimentally test each variable within that FOM will then be discussed. The data found in this section will give insight into how well the micron-droplets of PIP on the MEMS pixels perform as an IR detector.

4.2 Pyroelectric Coefficient

One parameter that governs the performance of a pyroelectric material is the pyroelectric coefficient. In a pyroelectric material, a change in temperature alters the steady state dipole moment of the material which, in turn, varies the spontaneous polarization of the material. The variation of the spontaneous polarization generates a displacement current that is parallel to the polar axis, and is described by

$$I_{pyro} = Ap\frac{dT}{dt}, \tag{51}$$

where, I_{pyro} is the displacement current, A is the cross-sectional area normal to the direction of current flow, p is the pyroelectric coefficient (which is the objective of this investigation), and dT/dt is the change in temperature with respect to time. A simple rearranging of Equation (51) allows for finding the pyroelectric coefficient, which was shown in Equation (10). The current generated is directly proportional to the pyroelectric

coefficient. Therefore, in an effort to design the most sensitive pyroelectric detector, a material that demonstrates the highest pyroelectric coefficient is desired.

One method that allows for accurate measurements of the pyroelectric coefficient is termed "the quasi direct method." This method was first introduced by Byer and Roundy in the early 1970s [1] and is currently one of the most widely used methods in determining this important material parameter. In an effort to collect low noise measurements, again the Keithley 6517a electrometer was used. The experimental set-up used MMR's K-20 temperature controller, along with their low temperature micro-probe pressure chamber.

First, MMR's low temperature micro probe (LTMP) is a compact material characterization station designed for industrial and laboratory applications where precision temperature control and electrical measurement conditions are essential [2]. The LTMP allows for accurate temperature conditions ranging from ~ 80 - 400 K. Cooling is accomplished with the Joule-Thomson effect using a high pressure nitrogen gas coupled with a pressurized chamber. Heating is accomplished using the stage's resistive heating element where the temperature of the stage/sample is monitored with a silicon diode transducer. Electrical throughputs attached to micro-probes allow for precise electrical contact to the sample under test. In an effort to accurately control the stage/sample temperature, MMR's K-20 temperature controller was used. Using an RS-232 connection, the K-20 can be controlled with a laptop using MMR's software. This software package allows for both temperature control and data logging, detected by the Si

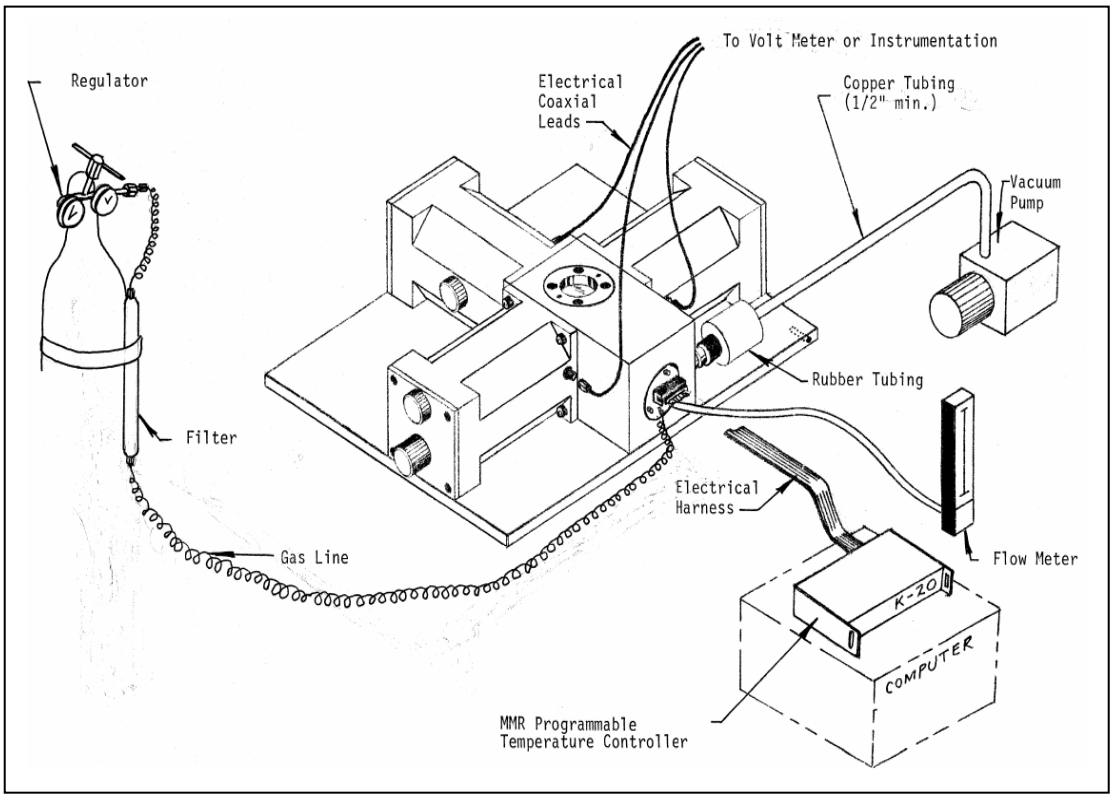

Figure 47: A generic setup shown by MMR technologies [2]. This system was used in the process for finding the pyroelectric coefficient.

diode, of both time and temperature at a 5 Hz rate. MMR's typical setup is shown in Figure 47.

Referring back to Equation (51) and using Byer and Roundy's paper on the quasi direct measurement technique, pyroelectric current measurements were taken. By accurately measuring the cross-sectional area and knowing dT/dt, which is essentially the temperature ramp of the stage, an accurate measurement on the material's pyroelectric coefficient can be obtained. A more specific illustration to the test setup used to find the pyroeletric coefficient used in this thesis is shown in Figure 48. The sample shown in Figure 21 was placed onto MMR's thermal stage with a thermally conductive double sided copper tape. It is also important to note that the assumption was made that the

temperature of the stage and the sample were the same. The electrometer was controlled via GPIB-USB with a Dell laptop using National Instruments Labview (V8.2). A modified program, compliments of Keithley, was used to control, monitor (real-time), and record data (~ 7.5 Hz). The K-20 temperature controller, as previously described, was controlled via RS-232, and came equipped with its own software driver.

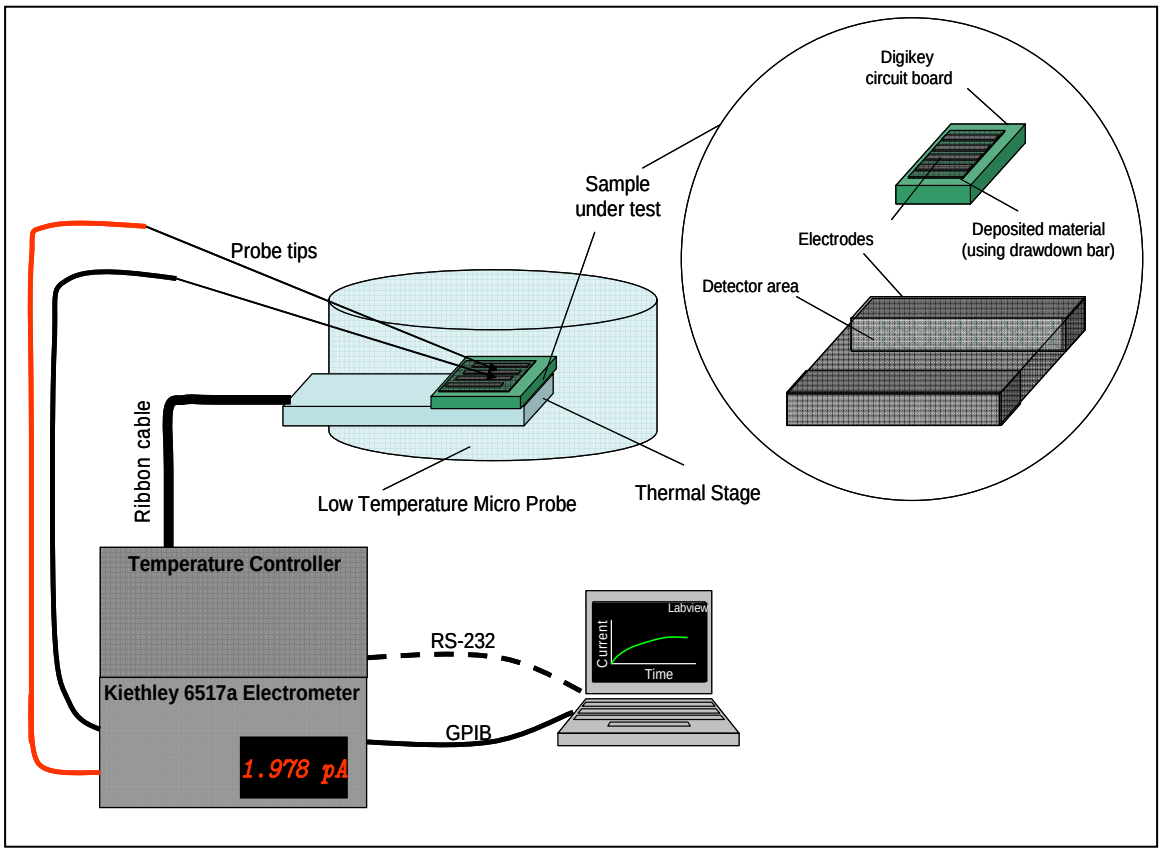

Figure 48: The experimental setup used to measure the pyroelectric current in this thesis. While accurately ramping the stage temperature on which the sample is mounted, a pyroelectric current is generated and measured.

This system setup allowed for accurate analysis of the current produced due to a change in sample temperature. Testing standards were quickly adapted to minimize variable differences when administering tests. These standards are shown in Table 5.

Two probe tips were placed on electrodes 2 and 3 of the sample under test. The co-axial outputs were connected to Keithley's triaxial cable directly into the electrometer. Ramp rates from 1 - 120 K/min were achievable using the MMR software. Also, due to the microphonic noise, testing was commenced at nighttime to mitigate any unwanted perturbations in the data. Once the sample was placed on the stage and a vacuum of 150 mTorr attained, the chamber was allowed to cool down to 275 K.

Table 5: Standard parameters used in measuring the pyroelectric coefficients.

Parameter	Value
Chamber pressure	150 mTorr
dT/dt	4 K/min
Electrodes used	2 and 3
Temperature range of stage	275 K – 380 K
Sample thickness	Varied (measured with profilometer)
Length of electrode	7 mm

Traditionally, preparing the sample for pyroelectric current measurements includes a poling process. In this poling process, the sample is heated and then cooled, while simultaneously placing a bias voltage across the sample. As indicated by J.F. Roeder in 1996 [3], overestimations of pyroelectric coefficients have been made using the traditional poling method. This article pioneers a new method of poling that mitigates this overestimation and is the method used in this thesis. Both the traditional and modified methods are depicted in Figure 49. The poling bias used for this thesis was 20 V, and the ramp rate was 80 K/min. The maximum temperature for the poling treatment was 380 K. The entire poling process took ~ 11 min.

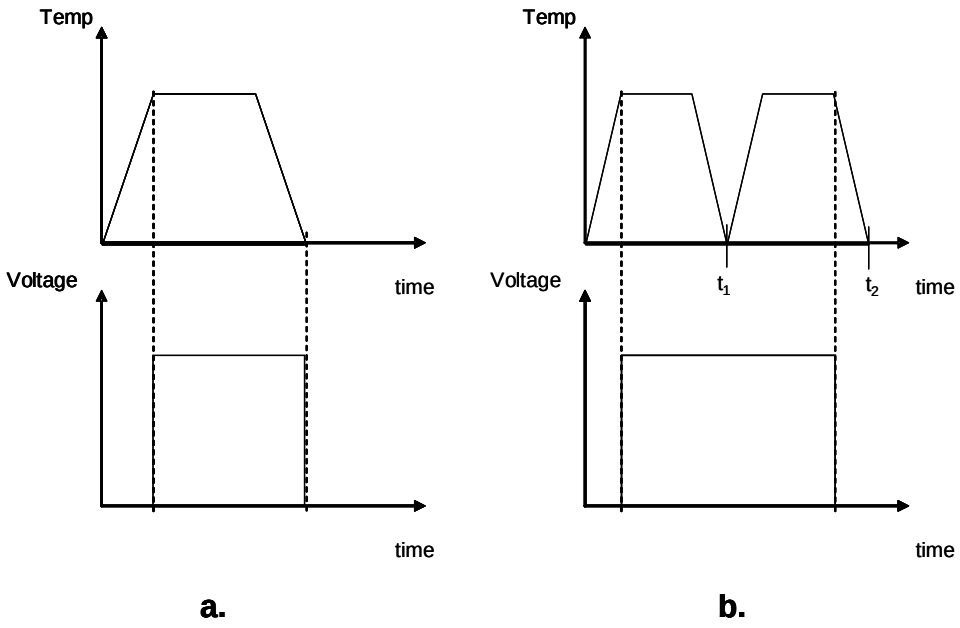

Figure 49: a) Traditional poling method used that was found to overestimate the measured pyroelectric coefficient. b) Modified poling method used in this thesis [3].

Once the poling treatment was complete, the pyroelectric measurements commenced. Since the PIP material, thus far, had only been used as a bolometric detector, variations of the PIP materials were examined in an effort to find the optimal solution to be used as a pyroelectric detector. The material that generates the most amount of displacement current when heated will be the best candidate for inkjet deposition. Also, to validate the pyroelectric current measurement setup used in this thesis, a sample of PVF_2, a known pyroelectric detection material, was similarly tested.

4.3 Responsivity ($\Re$)

The setup used in this thesis used two pixels connected in series or parallel (termed compensated pyroelectric detector). Both configurations were used, but it was found that the series compensated system worked best, and is what was used for this

thesis. In the compensated system, one of the pixels is blackened for maximum absorption of radiation, while the other pixel is made from a reflective material. In theory, only one pixel will be exposed to incident radiation and the signal produced from this pixel will be amplified, whereas all other temperature and mechanical contributions affecting both detectors at the same time will be eliminated. It was found that this effort mitigates microphonic noise so that a higher SNR can be found. The use of the compensated pixel design was crucial in finding a thermal response from the pixels and is shown in Figure 50. The major difference was this thesis' pixels only used an absorptive material (carbon black). Therefore, there was a need to completely focus radiation onto one pixel and leave the other pixel unexposed.

Unfortunately, it is very difficult to position the pixel under test so that the Ge lens focuses all incident radiation to the specific area of the pixel. Due to the fact that Ge is opaque in the visible spectrum, visually finding where the incident radiation that was being focused is not possible. A thermal response was found using the Ge lens system in the radiometric setup, but gave less than ideal results due to the fact that both pixels were exposed to the thermal source.

The radiometric setup is shown in Figure 51. Since the radiation was directed at both pixels, the full potential of the material's response was not being exploited. If each detector in the compensated pixel arrangement is subjected to the same amount of incident heat, their signals will neutralize each other and the total signal output will be zero [5]. In an effort to obtain a thermal response from the pixels using a blackbody source, the lens system (item 3), shown in Figure 51, was rotated (~ 30° from the normal

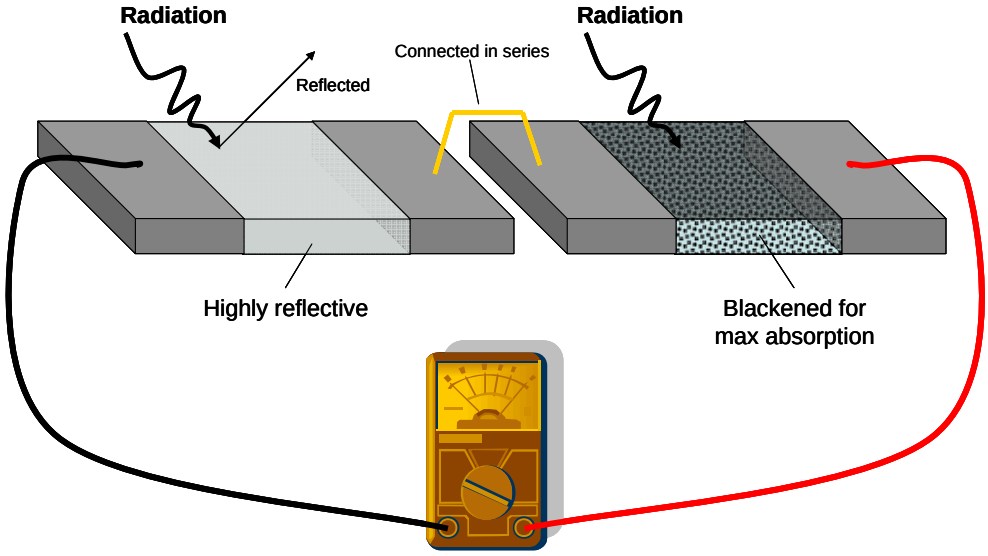

Figure 50: Ideal compensated pyroelectric detection system used to mitigate microphonic noise.

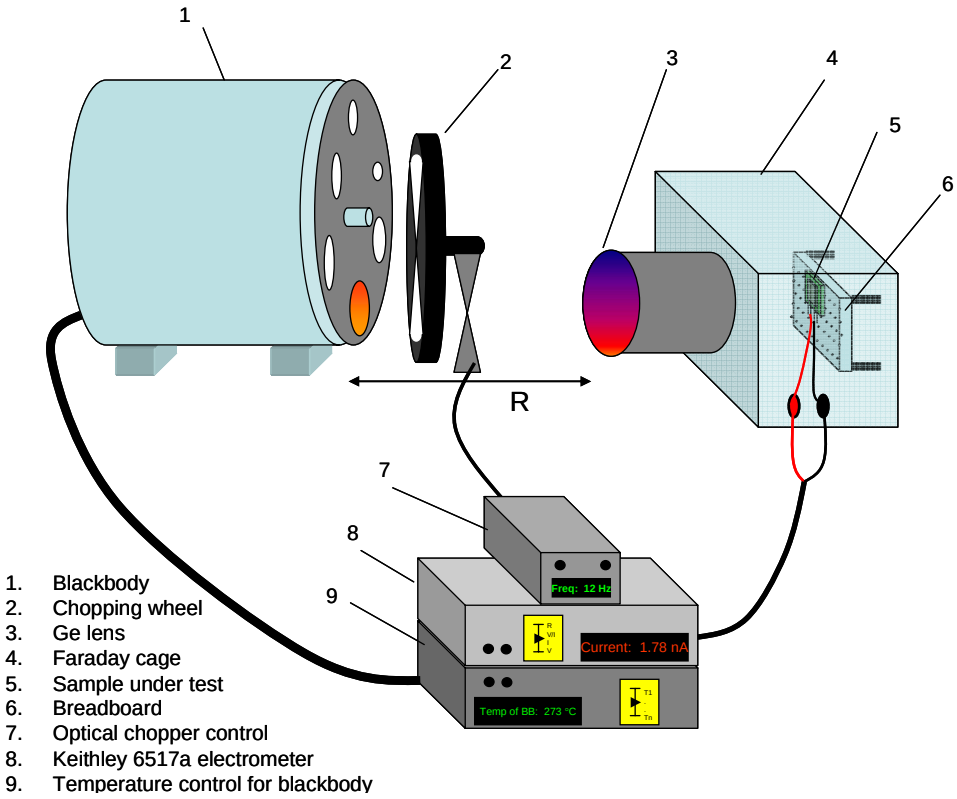

Figure 51: The radiometric setup used in this thesis.

to optical axis) to allow for only one pixel to be exposed to the blackbody source, while the other compensated pixel collected background flux. By defocusing the incident flux to capture a thermal response, an accurate flux calculation, could not be obtained. Without an accurate value for flux, responsivity, NEP, and detectivity could also not be found. Therefore, in place of the blackbody, a HeNe laser (632 nm) was used.

The laser source is ideal for the testing of these pixels because the compensated pyroelectric detection system can be used by only directing the incident power at the pixel under test. This setup is shown in Figure 52. The HeNe laser's output power is rated at 5 mW and it has a spot size with a diameter of ~ 1.5 mm at a range of 2 feet. In an effort to focus this incident beam down to the size of one of the MEMS pixels (~ 400 x 350 μm^2), a focusing optic was used with a focal length of 25 cm. The pixel under test was then positioned so that the focused HeNe spot size covered the entire pixel. The output from the pixel was first directed through an SR 560 (Stanford Research, Inc.) voltage pre-amplifier and then into the Keithley 6517a electrometer. As previously described, the output of a pyroelectric detector needs amplification, using one of the two circuits shown in Figure 19 or 20. In lieu of this circuit, a voltage pre-amp was used. Labview was used to control and collect data from the electrometer at a rate of 7.5 Hz.

Instead of making a radiometric calculation for the flux received at the detector, an optical power meter was used. By replacing the pixel with the power meter, accurate power measurements could be made, giving another way to obtain a value for responsivity. It will be shown that using the HeNe as the thermal source was the most effective way to collect good data from the pixels under test.

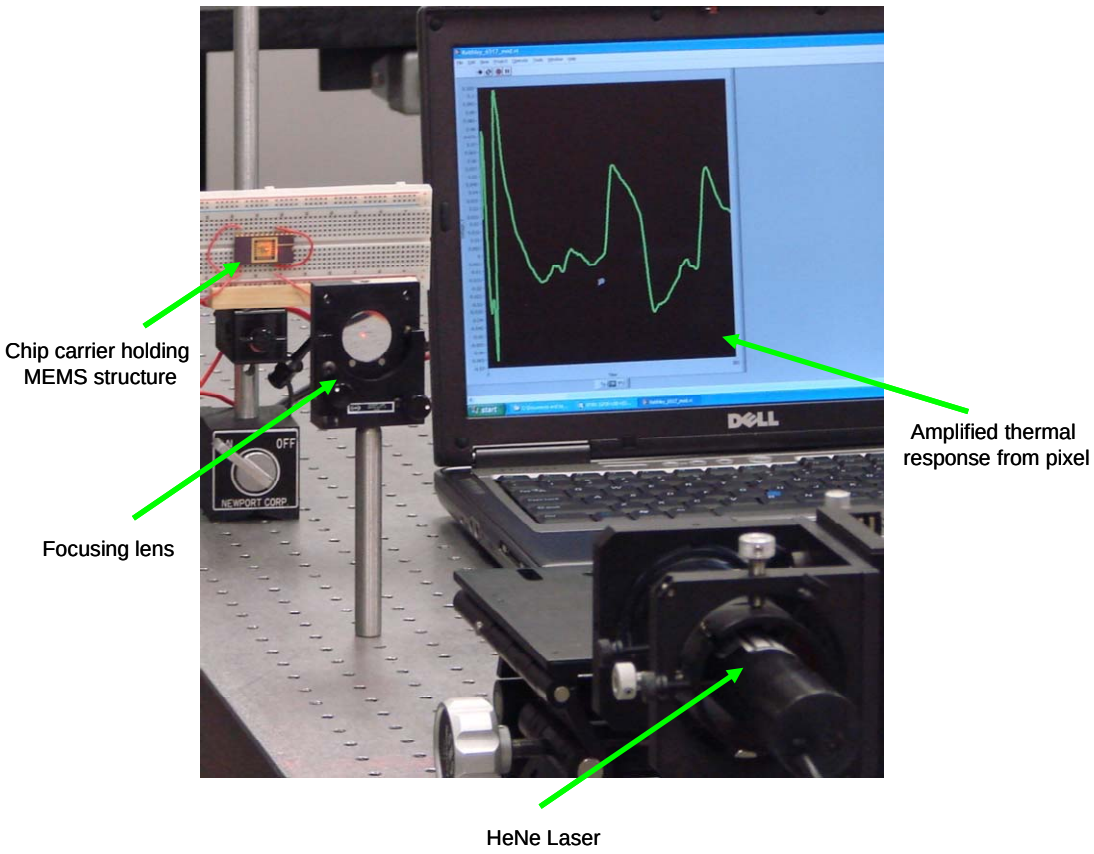

Figure 52: Responsivity test setup using a HeNe laser as the heat source.

4.4 Thermal Time Constant (τ_{th}) / Electrical Time Constant (τ_e)

This section will discuss how both the thermal time constant and electrical time constant will be found. Many assumptions will be made in these calculations and will be discussed when appropriate. First, the thermal time constant will be described. Second, since a voltage pre-amp is used to measure the voltage output, it is important to incorporate the electrical time constant into the calculations.

The same thermal time constant measurements taken for a thermister (another type of thermal sensor) will be used for pyroelectric device investigated in this thesis.

The value for the thermal time constant can be measured by exposing the detector to thermal radiation, then removing the thermal stimulus. The output signal of the detector will decay to a negative value (below the background noise floor) and slowly grow back to this noise floor value. The thermal time constant is the time at which the thermal response reaches 63.2% of the growth back to the background noise floor minus the time at which the thermal response reached its lowest value in the decay. This description is best represented in an illustration and is shown in Figure 53. Once a thermal response is found with the pixel, the thermal time constant can be measured.

One other component that is inversely proportional to the thermal time constant is the thermal conductance. Thermal conductance pertains to the structural posts that attach the elevated pixel to the substrate. This parameter has a dependence on both the materials used and their dimensions. To achieve the greatest rise in temperature of the pixel, the thermal conductance of the support structure needs to be minimized (Equation (6)). To minimize the thermal time constant (Equation (7)), the heat capacity needs to be as low as possible. For this thesis, the thermal conductance calculation will follow the analysis used by Chaobo [6]. Although, the equation is not perfectly suited for the interdigitized finger pixels used in this thesis, the calculations will give a good approximation. Also, since multiple layers of the material were needed to electrically complete the interdigitized finger circuit, the volume of material (thermal mass) was increased. The heat capacity is directly proportional to thermal mass, which when increased, also increased the thermal time constant.

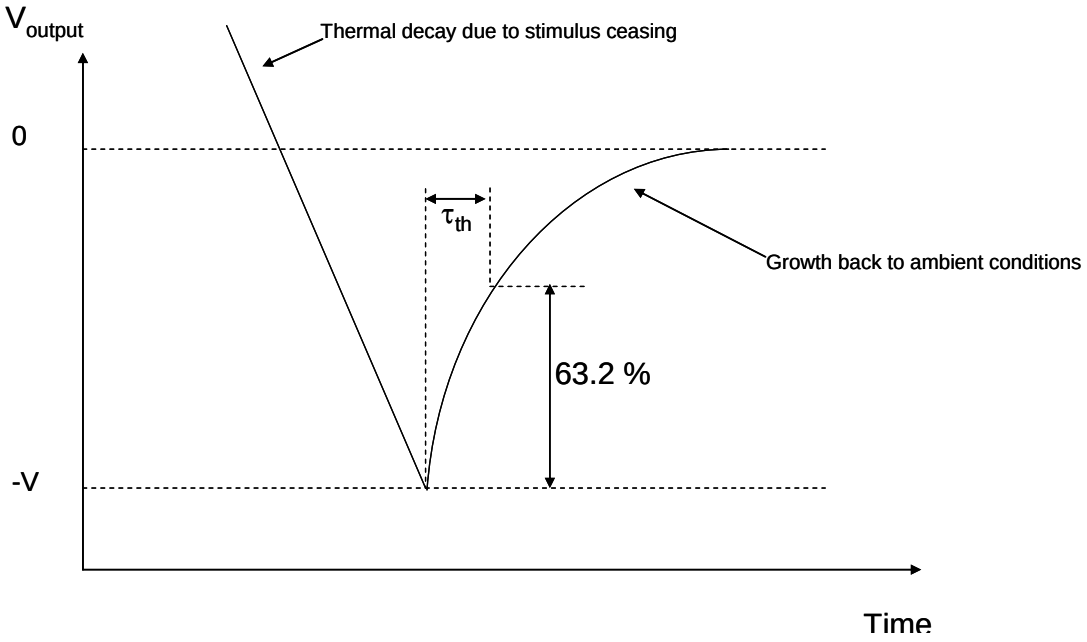

Figure 53: Technique to determine the thermal time constant as defined for a thermister which will be used in this thesis

The total thermal conductance is expressed as

$$G_{th} = G_{leg} = n^{-1}\left(\frac{L_{leg}}{k_{Poly2}A_{Poly2} + k_{Au}A_{Au}}\right)^{-1} \quad (52)$$

where G_{leg} is the thermal conductance of the metal (Au) /polysilicon (Poly-2) legs, n is the number of interdigitized fingers, L_{leg} is the length of the leg, k is the thermal conductivity, and A is the cross-sectional area of the specific leg material. Figure 54 summarizes all of the parameters seen in Equation (52). In Figure 54a, the top view of the small-gap MEMS pixel that was used is shown. The L_{leg} is the length of the pixel leg, and 1/13 of the interdigitized fingers is encompassed by the red box. The value for n will be the number of interdigitized fingers covered by the sensing area of the PIP (as seen from Figure 46, n = 3).

The other variable in the thermal time constant equation is heat capacity, C_{th} [J/K]. Although not necessary as it is not part of any of the required FOMs, it could be easily calculated given the thermal time constant, τ_{th} and the thermal conductivity, G_{th} (from Equation (7)). C_{th} consists of both material and geometrical attributes. As previously described typically thermal detector materials have a small heat capacity. However, the larger the volume of material deposited (thermal mass), the higher the heat capacity. Since the heat capacity is directly proportional to the thermal time constant, the thicker the material is the slower the response time. Due to the poor pixel design, multiple droplets of material were deposited, thereby increasing the thermal mass, which resulted in a slower than expected thermal time constant.

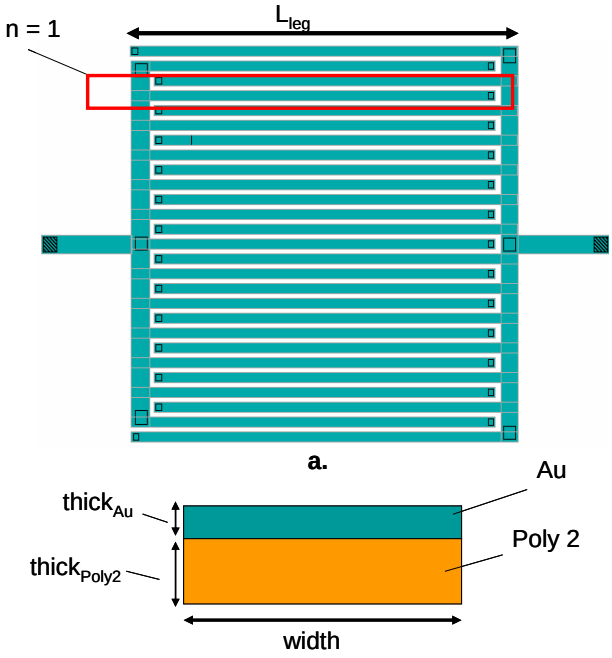

Figure 54: The small finger pixel used in this thesis depicting the dimensions that are used in the thermal conductance calculation. a) Top view showing the length of the leg and what is meant by the number of interdigitized fingers (red box is showing 1/13). b) Cross-sectional view showing the dimensions that are used in the area calculation.

The electrical time constant is the next topic of discussion. According to Dereniak [7], the electrical time constant is dependent on the parallel capacitance (C_d) and resistance (R_d) that comprise the pyroelectric material's equivalent circuit. This circuit was shown in Figure 13. In an effort to find these values, a Hewlet Packard 4284a LCR

meter was used. The value found for the electrical time constant will be another approximation because the lowest frequency measurement made by the HP 4284a was 20 Hz. If this was to be an accurate measurement, the same frequency at which the signal is chopped should be the frequency at which C_d and R_d are measured. Unfortunately, a thermal response of 20 Hz was not successfully achieved due to the lack of thermal isolation between the pixels and the substrate. However, the values given at 20 Hz for both C_d and R_d will be used for the calculation of the electrical time constant, and can be found by

$$\tau_e = C_d R_d . \tag{53}$$

4.5 Noise Equivalent Power (NEP)

NEP is typically a sufficient enough FOM to evaluate and compare the performance of a single pixel; it describes the radiant power incident on the detector that produces a signal equal to the rms detector noise. The noise in a detector is typically a result of multiple sources, many of which are difficult to measure and/or calculate. Therefore, to alleviate finding all of the individual noise sources, the NEP was found by visually monitoring the output thermal response. The incident flux is continuously attenuated until the output response is equal to the background noise.

Most IR lenses are not transimissive in the visible; therefore, focusing of thermal radiation is difficult. The positioning of the pixel in the blackbody test case was not optimized due to this fact. Future work needs to be accomplished at placing the pixel at the focal plane of the IR lens in an effort to maximize the responsivity using a blackbody source. However, using the HeNe laser as the thermal source makes pixel positioning easy. Since this laser operates at 632 nm (red), the pixel under test can be strategically positioned so that the spot size encompasses the pixel. This effort allows for testing the compensated pyroelectric pixel system by only illuminating the pixel under test.

In an effort to attenuate the amount of incident radiant power that reaches the pixel using the HeNe laser as the source, a variable neutral density filter was used. This filter is shown in Figure 55, and allowed for NEP measurements. The filter, made by Oriel optics, is a grading of aluminum deposited on top of glass. The more the wheel is rotated, the thicker the aluminum becomes, and the more the laser power is attenuated. This thickness of the grading is irrelevant because a power meter was used to collect the incident flux for each rotation of the filter wheel. By replacing the pixel under test with a power meter, accurate total incident power measurements were made. NEP testing began with the collection of noise floor data for ~ 1 minute. With no filter, the laser was turned on and the signal was chopped using a 0.33 Hz rate for ~ 10 periods. The laser source was then covered and the filter wheel was placed as to attenuate the laser power. Prior to exposing the pixel to the thermal stimuli, noise floor data was collected. The process of rotating the wheel (more attenuation), chopping, covering the source, and collecting noise floor data continued until the magnitude of the output signal voltage was the same as the

Figure 55: An image of the neutral density filter used to variably attenuate the HeNe power seen by the detector.

rms noise. It will be shown in the next chapter that additional attenuation was needed in an effort to force the output signal of the detector closer to the noise floor.

4.6 Detectivity (D*)

A FOM that is directly proportional with the detector performance is detectivity (D*). This FOM takes into account both the detector sensing area (A_d) and signal bandwidth (Δf). D* was defined in Equation (43). Once the NEP, A_d, and Δf are found, the D* value could easily be calculated.

4.7 Chapter Summary

Chapter 4 was dedicated to discussing all of the variables needed in finding FOMs for a pyroelectric detector. Some of the variables, such as the pyroelectric coefficient,

thermal time constant, and NEP, needed to be experimentally determined. Now that each of the FOMs has been explicitly described, a thorough investigation into the results found is in order. This will be the foundation for Chapter 5.

4.8 Works Cited

[1] Byer, R.L., Roundy, C.B., "Pyroelectric direct measurement technique and application to a NSEC response time detector." *IEEE Trans. Sonics Ultrasonics,* vol 3, pp 333 – 338, Nov 1971.

[2] MMR Technologies, Inc, "Low temperature microprobe user's manual." Copyright 1985, part number A9200300, Rev 7/85.

[3] Roeder, J.F, et al, "Liquid delivery MOCVD of PLT pyroelectric detectors," *Proceeding of the IEEE*, pp 227 – 230, 1996.

[4] Keyword "Lambertian", http://www.photonicsdirectory.com

[5] Rogalski, Antoni., *Infrared Detectors*. The Netherlands, Gordon and Breach Science Publishers, 2000.

[6] Li, Chaobo, et al, "A novel uncooled substrate-free optical-readable infrared detector: design, fabrication and performance." *Measurement Science & Technology,* vol 17, pp 1981 – 1986, Jun 2006.

[7] Dereniak, E.L., Boreman, G.D. *Infrared Detectors and Systems*. New York: John Wiley & Sons, Inc., 1996.

[8] Datskos, Panos, G., Lavrik, Nickolay, V., "Detectors –Figures of Merit." *Encyclopedia of Optical Engineering*, pp 349 – 357, 2003.

V. Results and Analysis

5.1 Chapter Overview

In this section of the thesis, all of the results that have been collected will be presented. In Chapter 4, each section was broken out describing in detail the experimental setup used to find a particular FOM. Although not intuitively obvious, there was logic in the descriptive order used in discussing these FOMs. Once the material was found to be pyroelectric, the pyroelectric coefficient is the most important parameter that governs how well the material generates pyroelectricity in the presence of a thermal stimulus. This will be the first results section described.

The rest of the FOMs, responsivity, thermal/electrical time constants, noise equivalent power, and lastly, detectivity, are all detector parameters that were found once the material was deposited onto the pixel. These FOMs could be found once a thermal response was found from the pyroelectric detector.

The series compensation configuration was found to give the best thermal response. In this system, only one pixel could be exposed to the thermal source and because of this the HeNe was found to give the best results. Therefore all FOM results that are presented used the HeNe as the thermal source. At the end of this chapter, a thermal response using the blackbody source will be shown. This effort is to prove that the material under test was not only responsive to 632 nm, but also to IR wavelengths.

This chapter's sections will directly correspond to those of Chapter 4. For each FOM the results will first be presented, followed by the analysis of the results. At the

end of this chapter a comparative analysis will be performed with off-the-shelf technology vs. the results found in this thesis.

5.2 Pyroelectric Coefficient

Once PIP was found to be pyroelectric, a control experiment such as the one shown in Figure 1, was performed using the pyroelectric coefficient system setup described in the previous chapter. This effort was accomplished to determine the TlpA protein's role in this pyroelectric material. The result of this experiment would determine exactly what material should be the focus of inkjet printing to the MEMS pixels.

This pyroelectric control experiment consisted of measuring the current generated from four different samples: PVA, PVA_CB, PVA_CB_TlpA, and PVA_TlpA. All samples incorporate glycerol in an effort to give the PVA its flexible properties. Using the same circuit board shown in Figure 21, all the aforementioned materials were deposited onto the circuit board with a pipette, and then using the squeegee technique, the electrodes were uniformly coated with comparable thicknesses. Since the thickness of the material was directly proportional to the current that is generated (see Equation(51)), accurate measurements were taken using a profilometer. Also, all measurements were taken between electrodes 2 and 3 for each material under test. The only two parameters that varied between each test were the thickness and the material. Table 6 shows all of the materials and their applicable thicknesses used in this test case. The results from this pyroelectric current test can be seen in Figure 56.

As previously stated, the objective of this test was to determine the role of the TlpA protein, and ultimately determine the ideal material to deposit onto the MEMS

Table 6: Material thicknesses of the samples used in determining the optimal material to inkjet deposit onto the MEMS pixels.

Material	Thickness [µm]
PVA	38
PVA_CB	36
PVA_CB_TlpA	26.7
PVA_TlpA	38.8

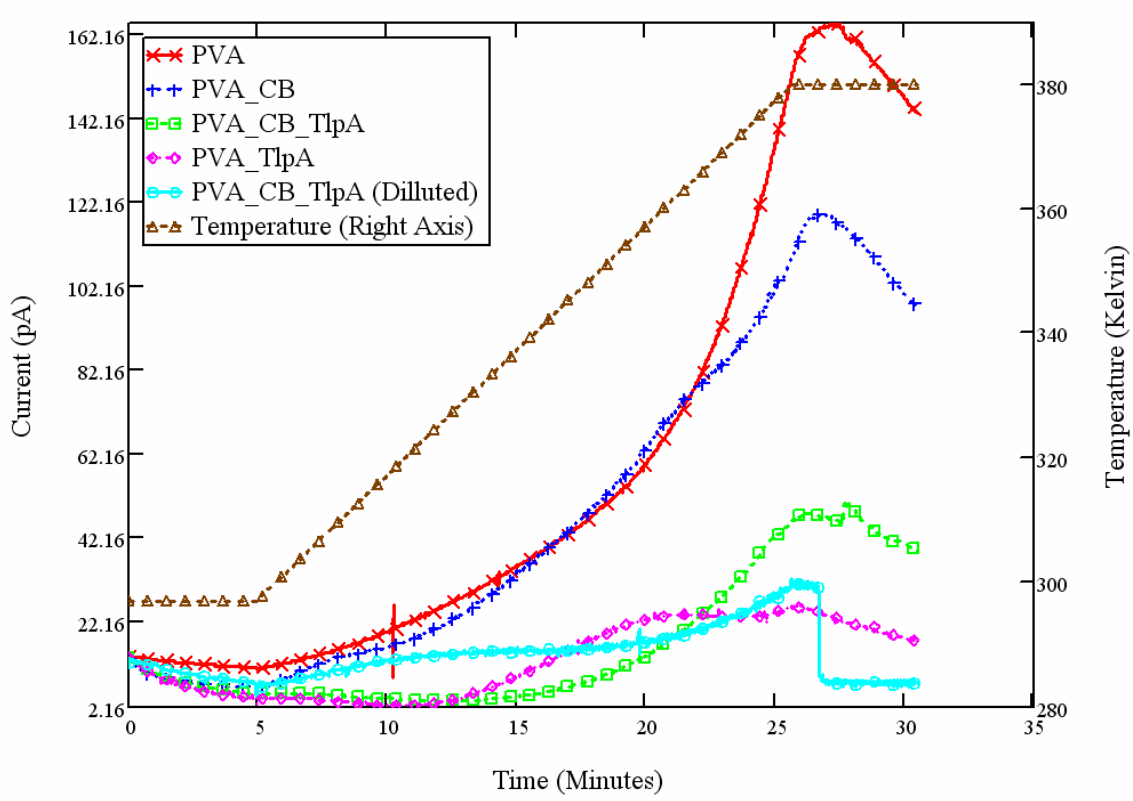

Figure 56: Results of pyroelectric current test performed on 4 different samples in an effort to determine the benefit of the TlpA protein when PIP is treated as a pyroelectric material (without a bias).

pixels. Since the pyroelectric coefficient is directly proportional to current generated, the sample that produces the greatest amount of current with the 4 K/min temperature ramp would be the better material to be used as a detector. This figure clearly shows that the TlpA protein hinders rather than benefits the thermal response of the pyroelectric

material. This contradicts the results found by AFRL/MLPJE when the material was thought to be bolometric.

It is clearly evident that the PVA alone generated the most current in response to the 4K/min thermal stimuli. Not too far behind PVA, was PVA_CB, which is a well proven IR absorber, due to the emmisivity of carbon black ($\varepsilon \sim 0.8$ [2]). A decision to inkjet deposit PVA_CB was made due to this property. Therefore, for the rest of this document the term PIP will no longer be used, and in its place will be PVA_CB.

To inkjet print, the PVA_CB material needed to be diluted in an effort to reduce its viscosity. Therefore, various dilution ratios of the material were printed in an effort to find the ideal continuous output stream (see Figure 39). The PIP material tested in Figure 56 was not diluted, and therefore had a ratio of 0:1. The least diluted material that was able to be printed was 3:1 (for every 1 mL of solution there was an additional 3 grams of water) and will be the material that will be described throughout the rest of the results section of this thesis.

Fortunately, AFRL/MLPJE was able to obtain PVF_2 (polyvinyl fluoride) and prepare a sample the same way the PVA_CB sample was prepared. PVF is a well known and well documented pyroelectric polymer that is currently used commercially. Thus, a pyroelectric coefficient comparative analysis was accomplished between the 3:1 PVA, 3:1 PVA_CB, and the well known PVF, using the macro-circuit boards shown in Figure 21. Again, using the squeegee technique, the materials were coated in a thin film. The material thickness for the 3:1 PVA was found to be 8.31 μm, the PVA_CB, 4 μm, and the

PVF, 63.7 µm. The PVF material was dissolved in dimethyl formamide. A 4 K/min temperature ramp was used in this test case and the results are shown in Figure 57.

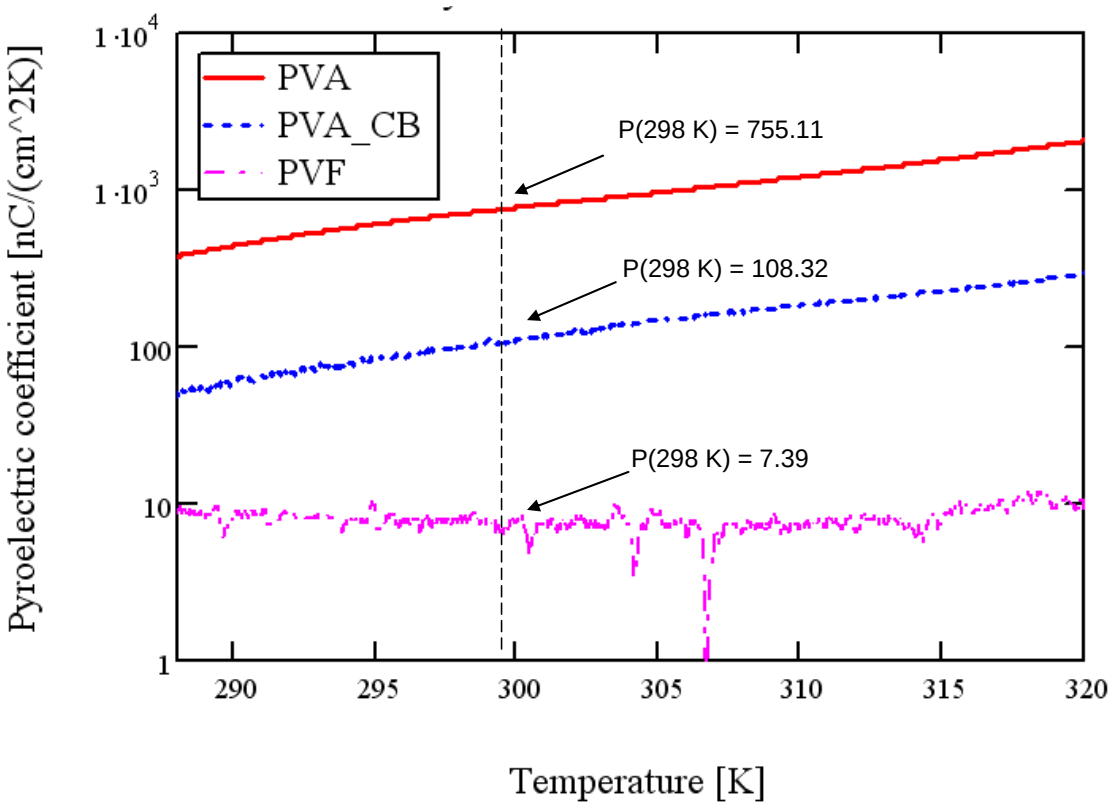

Figure 57: Pyroelectric coefficient comparison between PVA, PVA_CB, and PVF.

From the analysis of Figure 57, it is evident that the PVA alone outperformed the PVA_CB, and the PVF. The comparative analysis is done at room temperature (298 K) because currently published articles use this temperature and it is the temperature at which the detector will operate. Also, this plot shows that the carbon black particles actually hinder the ionic transfer of the material in response to the thermal stimulus. Although this hindering decreased the pyroelectric coefficient by ~ 640 nC/(cm^{2}K), the carbon black particles are a proven IR absorber, and the PVA_CB solution is what was

ultimately deposited to the MEMS pixels. It is evident that further research needs to be done on the use of PVA alone, as a pyroelectric detection material.

Referring to Table 7, PVF has a published pyroelectric coefficient of ~ 3.2 nC/(cm^{2}K) at room temperature [7]. This is 4.14 nC/(cm^{2}K), lower than the PVF material's pyroelectric coefficient measured here. These results demonstrated that the "quasi direct method" experimental setup gave results on the same order of magnitude published previously, affirming that the results found for PVA and PVA_CB are valid. Also, the PVA results showed how much better this material is in comparison to a known pyroelectric polymer.

As previously stated, the pyroelectric coefficient is a material parameter that governs the performance of that material as a pyroelectric detector. Therefore, Figure 57 is a good illustration depicting the benefit of using the PVA_CB material. Both the PVA and PVA_CB show values two orders of magnitude higher than what was measured for the PVF. Referring to Table 7, the PVA and PVA_CB materials are shown to outperform all other pyroelectric materials, as well. From this table, each pyroelectric material has a defined Currie temperature, which is the temperature at which the material loses its pyroelectric properties. It must be noted that the Currie temperature was never found for the PVA or PVA_CB materials. The maximum allowable temperature of the conductive stage was rated at 380 K, which also leaves more research into material characterization. This shows that PVA_CB can be proven to outperform ~ 55 % of listed materials shown in Table 7 since it shows both a higher pyroelectric coefficient and a higher Currie temperature.

Table 7: Pyroelectric materials and their properties [7].

Material	Material Type	Temp of Measurement (K)	Pyroelectric coefficient, p ($nCcm^{-1}K^{-1}$)	Heat capacity, c_{th} ($Jcm^{-3}K^{-1}$)	Dielectric constant, ε_r	Currie Temperature, T_c (K)
TGS	Crystal	308	55	2.6	55 (1 kHz)	322
DTGS	Crystal	313	55	2.4	43 (1 kHz)	334
TGFB	Crystal	333	70	2.6	50 (1 kHz)	346
ATGSAS	Crystal	298	70	-	32 (1 kHz)	324
$LiTaO_3$	Crystal	298	23	3.2	47	938
SBN-50	Crystal	298	55	2.34	400	394
PGO	Crystal	298	11	2.0	$5x10^{-4}$ (100 Hz)	451
PGP:Ba3	Crystal	298	32	2.0	$1x10^{-3}$ (100 Hz)	343
PZFNTU	Ceramic	298	38	2.5	290 (1 kHz)	503
PCWT-4/24	Ceramic	298	38	2.5	220 (1.5 kHz)	528
PVF_2[7]	Polymer	298	3.2			
PVDF	Polymer	298	2.7	2.43	12 (10Hz)	353

5.3 Responsivity (ℜ)

This section will be dedicated to presenting the results of the responsivity measurements using the HeNe laser as the thermal source. In an effort to capture the incident flux power of this laser, the pixel under test will be replaced with an optical power meter. The voltage data logged from the thermal response will be analyzed in an effort to calculate HeNe responsivity. Also, at the end of this section a thermal response from a 700 K blackbody will be shown, demonstrating a response from a broadband IR source.

5.3.1 HeNe Responsivity

The best results were captured using a 5-mW HeNe laser. Using an Oriel lens, the spot size was focused onto one of the two compensated pixels. The signal was chopped at ~ 0.33 Hz which allowed for a maximum output voltage response. After the thermal response data was collected, the MEMS structure was replaced with an optical

power sensor to collect the power from the laser. The responsivity data was collected by attenuating the HeNe laser's output using the aforementioned neutral density filter. The voltage response from the HeNe source is shown in Figure 58. The change in voltage in response to the illumination of the laser was found to be 28 mV, averaged over ten periods. When the MEMS pixels were replaced with an optical power meter, the incident attenuated HeNe power was measured to be 1.68 μW. The responsivity calculation resulted in,

$$\Re_{V\_HeNe} = \frac{\Delta V}{\Phi_e} = \frac{28\,\text{mV}}{1.68\,\mu\text{W}} = 1.66\,x10^4\ \frac{\text{V}}{\text{W}}. \tag{54}$$

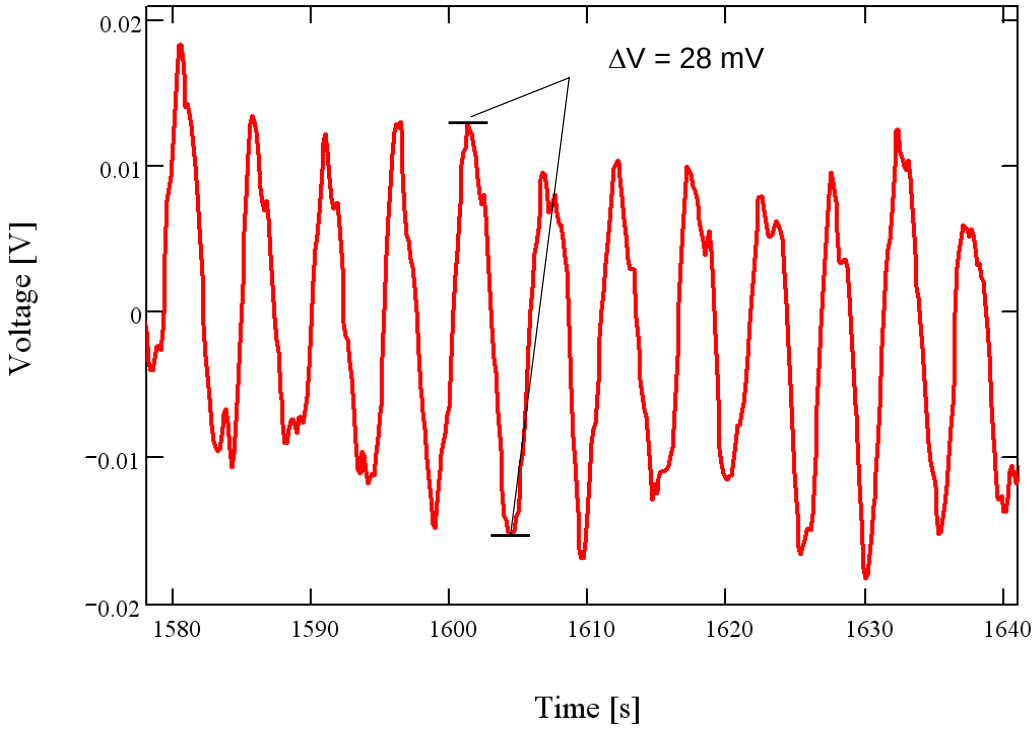

Figure 58: Thermal response using an attenuated 5-mW HeNe laser as the thermal source. The ΔV was found to be 28 mV.

5.3.2 Blackbody Thermal Response

As described in Chapter 4, a thermal response was found using a blackbody source. Due to improper alignment with the lens system, the imaged blackbody aperture was much larger than the pixel area, exposing both pixels in the compensated configuration. According to [3], if both pixels are subject to the same amount of thermal radiation, their signals will neutralize each other leaving the total output signal equal to zero. Therefore, in an effort to expose one of the two pixels and capture a thermal response, the lens system was rotated ~ 30 ° from the normal to the optical axis. The system setup used to capture a thermal response from the blackbody is shown in Figure 59.

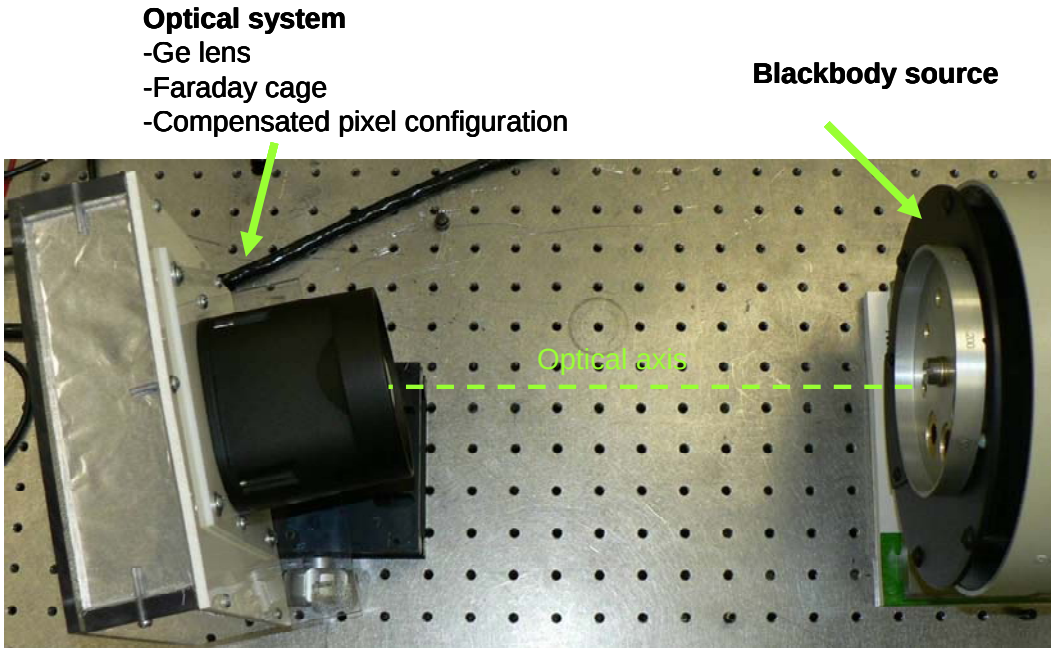

Figure 59: The optical system used to obtain a thermal response from a blackbody source. Since the imaged blackbody aperture was much larger than the size of the pixel the optical system needed to be rotated ~ 30 ° from the normal to the optical axis. This effort only exposed one of the two pixels in the compensated design to incident flux from the blackbody source.

A modulation frequency of 0.125 Hz was used after exposing the PVA_CB pixel to the 700-K blackbody source. The open aperture of the blackbody was set at 1-inch, and with a Keithely 6517a electrometer, voltage response data was collected. The thermal response to a 700-K blackbody is shown in Figure 60. Although an accurate flux calculation could not be made because the optical system needed to be defocused for these measurements (see Chapter 4), it is evident that the PVA_CB pixel responded to blackbody thermal radiation. Future research needs to concentrate on focusing IR radiation down to the dimensions of a pyroelectric pixel or properly shielding on of the compensated pixels from the blackbody radiation.

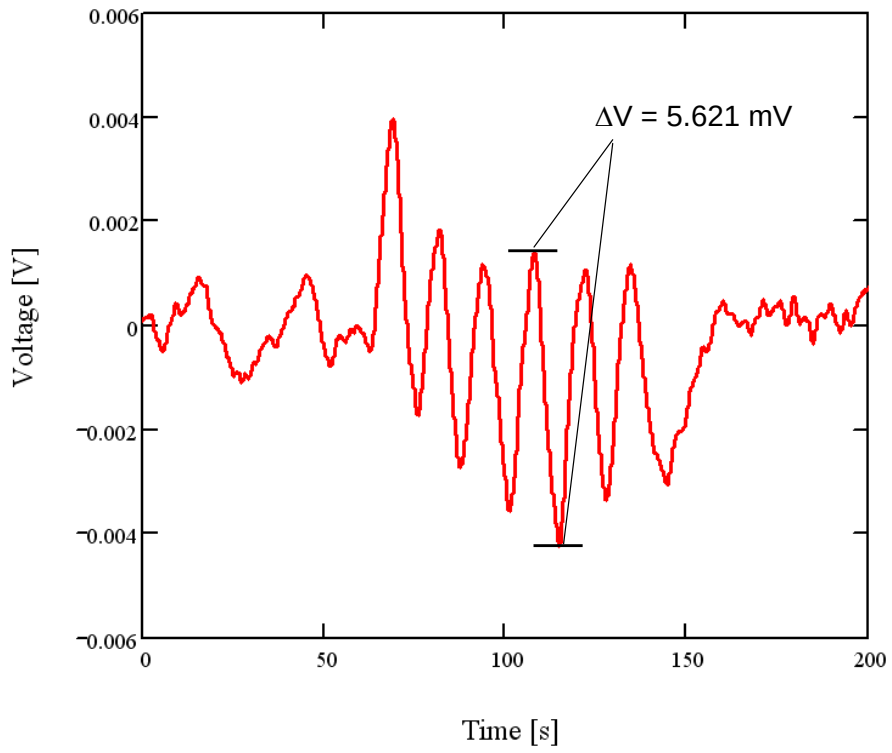

Figure 60: The thermal response using a 700 K blackbody source. The peak to peak ΔV was found to be 5.621 mV.

The responsivity calculation found in this thesis was accomplished using a HeNe as the thermal source. This effort allowed for visually focusing the incident radiation onto one of the two pixels in the compensated pixel configuration. A thermal response was then found using a 700 K blackbody, demonstrating that the material is sensitive to IR wavelengths. Due to alignment problems with the Ge lens system, accurate flux values could not be found, leaving room for further research.

5.4 Thermal Time Constant (τ_{th}) / Electrical Time Constant (τ_e)

The thermal time constant is a FOM that determines how fast the pixel can bleed off its heat after being exposed to a thermal stimulus. The main rationale for this FOM is to show the potential of a material/pixel design for use in an imaging system. A standard imaging system operates at 30 frames/sec (30 Hz). The pixel response time should be somewhat shorter than 1/30 sec. According to Kruse, a common practice is to make the response time of the pixel, 1/3 of the reciprocal of the frame rate. In the case of 30 Hz, the response time would be ~ 10 msec [4]. Since thermal isolation is one of the major contributors in a fast thermal response time, it will be shown that the pixel designs used in this thesis have much room for improvement.

The thermal response using the HeNe laser showed the best results, and will be used in the thermal response time investigation. Figure 61 illustrates this thermal response, which looks almost identical to the thermister's thermal response, shown in Figure 53. Using the 63.2 % thermister criteria, the time constant for the pixel under test for this thesis was found to be 3.59 sec. This is approximately two orders of magnitude slower than required to use this pixel/material in a thermal imaging system. As shown

from Figure 44, multiple droplets of PVA_CB were desposited to coat the interdigizied fingers, thereby increasing the thermal mass of this pyroelectric material. This is likely the main reason for the slow response time. In an effort to achieve a faster response time using the inkjet deposition system, a better pixel design needs to be constructed that will allow for accommodating a single layer of deposited material (less thermal mass). This will potentially give the pixel/material the response time needed to use this material in a thermal imaging system.

As discussed previously, there are two other components involved in the thermal time constant, heat capacity, C_{th}, and thermal conductance, G_{th}. Since the thermal time constant has already been found, according to Equation (7), if either heat capacity or

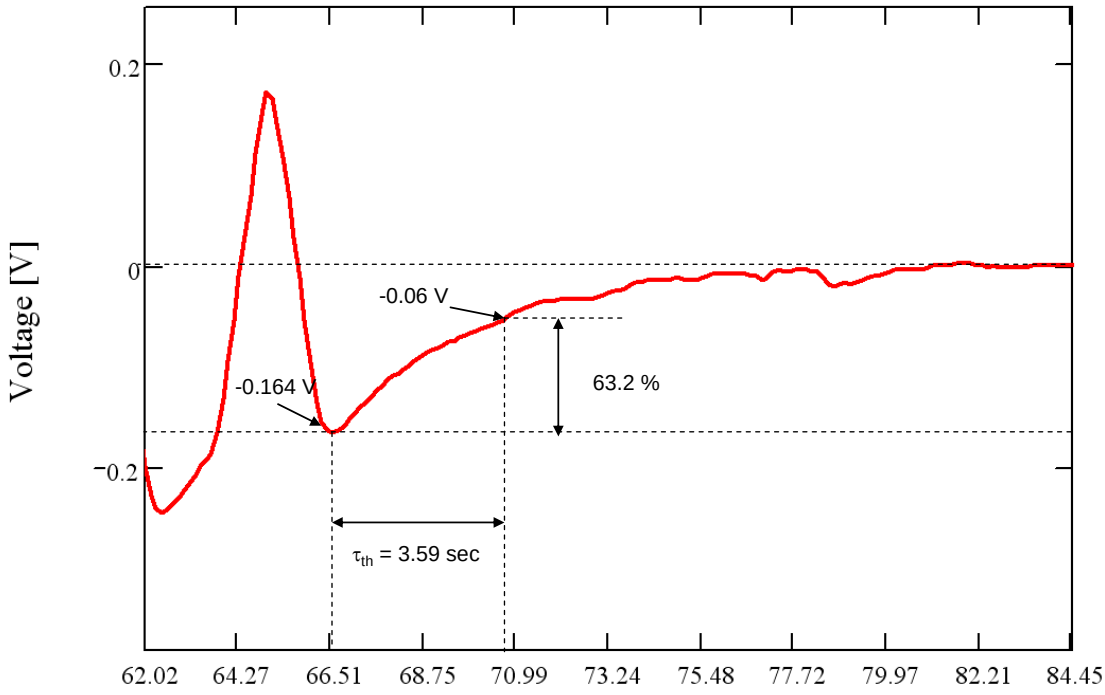

Figure 61: The thermal response from the MEMS pixels depicting the thermal response time according to the thermister time constant criteria. The thermal response time was found to be 3.59 sec.

thermal conductance can be found, the other can easily be determined. Thermal conductance will be solved using Equation (52), and from this, the heat capacity will then be found.

The parameters used to solve Equation (52) are shown in Table 8, which result in a thermal conductance of 1.504 μW/K. Thus, rearranging the terms in Equation (7) allows for solving the heat capacity, which was found to be 5.41 μJ/K. These calculations need to be readdressed when an ideal thermally-isolated pixel is designed. Since there was no thermal isolation, the value found for thermal conductance is not accurate. Thermal conductance is a measure of how well the pixel absorbs and dissipates heat. When the structure is adhered to a near-infinite heat sink (i.e., the substrate), the pixel's thermal conductance can not be calculated using Equation (52). Also, because the heat capacity is a key material parameter of the active region, experiments need to be accomplished to find the heat capacity for the PVA_CB material.

Table 8: A list of the all parameters used in solving Equation (52).

Parameter	Value
Number of interdigitized fingers covered by PIP (n)	3 (See Figure 54)
Length of finger (L_{leg})	450 μm
Thermal conductivity of Poly2 (k_{Poly2})	32 W/(m-K) [5]
Cross-sectional area of Poly2 (A_{Poly2})	10 μm x 1.5 μm
Thermal conductivity of Gold (k_{Au})	310 W/(m-K)
Cross-sectional area of Gold (A_{au})	10 μm x .5 μm

The electrical time constant is calculated from Equation (53). Using a HP 4284a LCR meter, operating in parallel capacitance and parallel resistance (PCPR) mode, the equivalent circuit parameters can be found. The lowest frequency at which these values were obtained was 20 Hz. If this measurement was to be done correctly, both the

chopping frequency and the frequency at which the equivalent circuit values were collected should be the same. Unfortunately, due to the length of the thermal time constant, a chopping frequency of 20 Hz was not obtained. Thus, an assumption that a modulation frequency of 20 Hz was made, and, therefore, that the parallel capacitance and resistance values measured at 20 Hz are valid for measuring the electrical time constant. These values are shown from the data given by the LCR meter, and can be seen in Figure 62.

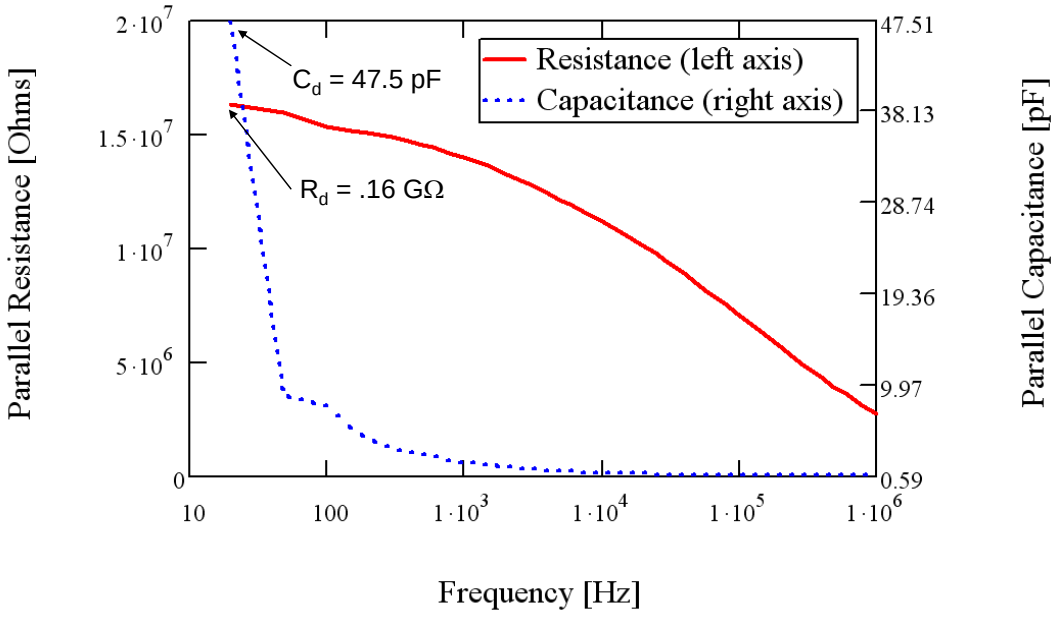

Figure 62: Parallel capacitance and parallel resistance data taken from a HP 4284a LCR meter. Values for the equivalent circuit (seen in Figure 19) that model the pyroelectric detector were found in an effort to solve the electrical time constant.

The capacitance and resistance found at 20 Hz are 47.5 pF and 0.16 GΩ, respectively. This leads to an electrical time constant of 7.6 msec which is the time required to charge the small-signal capacitance (C_d) through the small-signal resistor (R_d) to 63.2 % of a full charge.

5.5 Noise Equivalent Power (NEP)

This section will describe the results found in the NEP experiment using the HeNe as the thermal source. In an effort to attenuate the incident thermal flux on the pixel, a neutral density filter (Figure 55) was used.

When the HeNe was used as the thermal source, a SNR of one was found by attenuating the laser's power with a neutral density filter. For each turn of the filter, a corresponding power measurement was made with an optical power meter. This effort ultimately led to a minimal detectable signal with a corresponding NEP. A second neutral density filter was needed to further attenuate the HeNe to find the NEP.

Figure 63 shows the first examination of the NEP using the HeNe laser as the heat source. The minimal incident flux (thickest grading on ND filter) was found to be 2.9 μW at the detector. It is evident that the signal is still well above the noise floor which does not result in a value for NEP. An additional test was then executed adding additional ND filters, further attenuating the HeNe source. Figure 64 illustrates a further attenuated HeNe source that still shows the signal above the background noise floor. This flaw can be attributed to monitoring the NEP real-time in Labview. During the experiment, the magnitude of the thermal response signal appeared identical to the background noise. When the data was post processed, the thermal response was clearly still greater than that of the background noise.

The experimentally found NEP was 21.3 nW. This value will be used in determining the value for detectivity (D*). It is important to note that the background noise variance can be minimized immensely by the proper shielding and

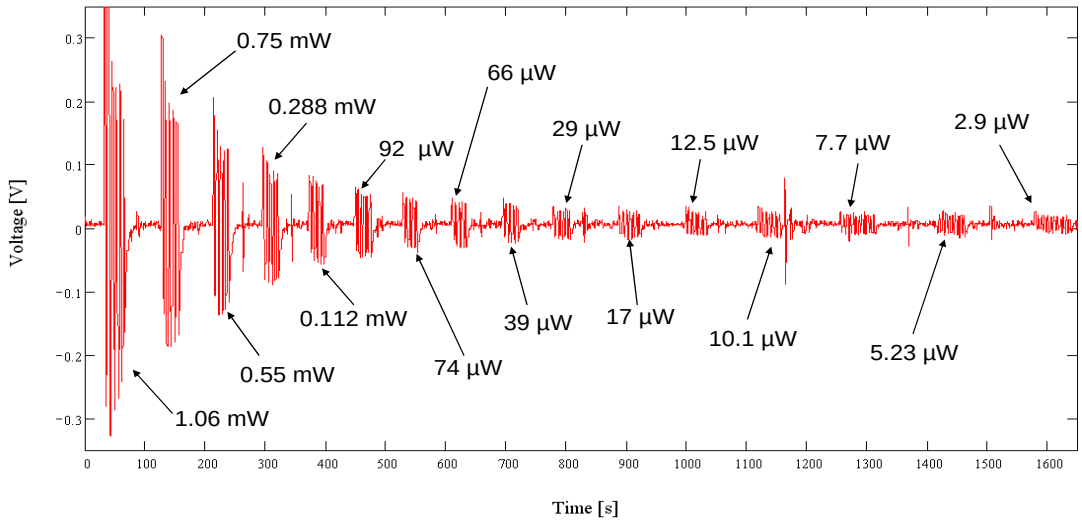

Figure 63: Thermal response from an increasingly attenuated HeNe laser. The laser was attenuated using a neutral density filter in an effort to find the NEP. It is evident that the signal is still well above the background noise floor, even with a measured 2.9 µW of incident power.

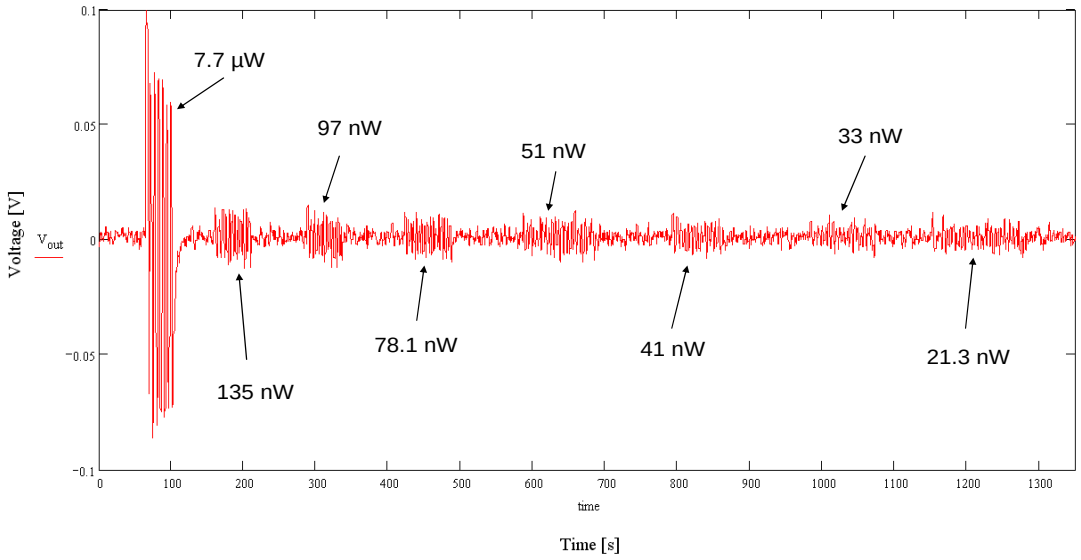

Figure 64: A further investigation into the NEP using the HeNe source. The NEP was found to be 21.3 nW**.**

connections, thereby decreasing the NEP values even further. Due to detectivity being inversely proportional to the NEP, comparable D* values will be lower than expected.

5.6 Detectivity (D*)

The detectivity for the thermal detector designed in this thesis will be evaluated using the NEP value found in the previous section. Due to the fact that an accurate flux calculation could not be made, a value for D* could not be found for the blackbody source. This section will be dedicated to calculating the D^*_{HeNe} using Equation (43).

Applicable values for solving detectivity are shown in Table 9. The D* values are far less than current IR detector technology which is attributed to the pixel's lack of thermal isolation over the underlying substrate. The empirically–determined D^*_{HeNe} was found to be $1.93 \times 10^5 \left[\text{cm}\sqrt{\text{Hz}}/\text{W}\right]$.

Table 9: Blackbody and HeNe detectivity results.

Heat Source	(A_d) [cm^2]	(Δf) [Hz]	(NEP) [nW]	Detectivity (D*) $\left[\text{cm}\sqrt{\text{Hz}}/\text{W}\right]$
Blackbody (700 K)	1.01×10^{-4}	0.063	---	---
HeNe	1.01×10^{-4}	0.167	21.3	1.93×10^5

In an effort to analytically calculate the detectivity found in Equation (43), all parameter values will be presented followed by the D* result found. All applicable parameters relating to the source will correspond to using the HeNe laser and the assumption will be made that the detector is operating in the Johnson noise-limited region. Table 10 defines each of the parameters and their applicable values needed in solving for the D* given by Equation (43). The analytically-determined for D* was found to be $1.59 \times 10^6 \left[\text{cm}\sqrt{\text{Hz}}/\text{W}\right]$ which is an order of magnitute greater than the D^*_{HeNe} that was solved for using the experimentally solved NEP. Many assumptions

were made in an effort to obtain some of the values shown in Table 10, which resulted in more than a 724% error. The D^*_{HeNe} is a more accurate value, and will be used in the comparison section that follows.

Table 10: Parameters used in solving for D* seen in Equation (43).

Parameter	Value
Area of detector (A_d)	3.602×10^{-5} [cm^2]
Equivalent resistance (R_d)	0.16 [GΩ], at 20Hz from LCR meter
Pyroelectric coefficient (p)	108.32 [nC/(cm^2 K)], at 298 K
Emmissivity (ε)	0.8, for carbon black
Modulation frequency (ω)	2.07 [rad], chopping frequency 0.33 Hz
Temperature of detector (T_d)	298 [K], room temperature
Thermal conductance (G_{th})	1.504 [μW/K]
Thermal time constant (τ_{th})	3.6 [sec]
Electrical time constant (τ_e)	7.6 [msec]

5.7 PVA_CB-based Pyroelectric Detector vs. Off-the-shelf Thermal Detectors

In an effort to best quantify all the FOMs that were found in this thesis, an analysis will be performed comparing the PVA_CB-based thermal detector to a list of other thermal detectors. The other detector FOMs were obtained from an article that was published in 1972 by E.H. Putley [6]. Although this article is more than thirty years old, a baseline understanding of the PVA_CB-based detector's potential will be shown. The comparison analysis between thermal detector types, to include PVA_CB, is shown in Table 11.

The obvious performance FOM that is less than ideal in the PVA_CB pyroelectric detector is the thermal response time. The root cause of the slow response time was the thermal mass of the multiple deposited droplets of PVA_CB. The initial

thoughts in the pixel construction was that the interdigitized fingers, once released, would deflect in the z-direction enough to support a single droplet of the inkjet-deposited PVA_CB. It is evident from the image in Figure 44 that a single droplet was not enough to complete the circuit across the interdigitized fingers. Therefore, multiple droplets were needed, increasing the heat capacity, which increased the thermal time constant. Also depositing the material onto a thermally isolated structure will increase the responsivity. Reponsivity is directly proportional to dT/dt, as shown in Equation (51). The faster the sample heats up/cools off, the more current will be generated and the higher the responsivity will be. The NEP is comparable to other thermal detectors, but could be much lower using proper shielding techniques in an effort to mitigate noise. Also, the integration time is inversely proportional to the electrical bandwidth (Δf). If the integration time is decreased, Δf increases, and so does detectivity. Basically, a new pixel structure needs to be designed and constructed.

Table 11: Summary of thermal detectors to include the PVA_CB pyroelectric [6].

Detector type	T_d [K]	A_d [cm^2]	τ_{th} [s]	$\Re_v$ [V/W]	NEP [W]	D* [cm $Hz^{1/2}$/W]
PVA_CB pyroelectric	298	1.01×10^{-4}	3.59	1.66×10^{4}	21.3×10^{-9}	1.93×10^{5}
TGS pyroelectric	298	10^{-2}	1×10^{-6}	1000	-	10^{9}
$BaTiO_3$ bolometer	298	10^{-3}	1×10^{-3}	10	-	3.5×10^{5}
$Tl_2SeAs_2Te_3$ bolometer	298	10^{-3}	1	100	-	1.5×10^{7}
Golay cell	298	6×10^{-2}	15×10^{-3}	-	2×10^{-10}	
Thermopile	298	10^{-3}	0.1×10^{-3}	100		3×10^{8}
Au/Si_3N_4 microcantilever	298	6×10^{-5}	0.3	-	3.46×10^{-10}	3.59×10^{7}

5.8 Chapter Summary

The results of this thesis were presented and discussed in this chapter. First, it was proven that the TlpA protein inhibited the performance as a pyroelectric material. Thus, the material chosen to be inkjet deposited included only the PVA and carbon black. A comparison analysis between a known pyroelectric polymer, PVF, was used to validate the pyroelectric coefficient experimental setup and also demonstrate how well the PVA and PVA_CB materials performed in comparison. Once a thermal response was found, the FOMs could then be easily found. All FOMs measured/calculated were then presented in Table 11 to compare performance with other thermal detectors. The main reason for the PVA_CB-detector shortfalls could be attributed to the lack of thermal isolation from the underlying substrate and could potentially be fixed with a different pixel structure. This fix needs to be the first follow-on research topic. With this approach, the FOMs for this newly found material are envisioned to exceed the performance of published uncooled thermal detectors shown in Table 11.

5.9 Works cited

[1] Brott, Lawrence L., Rozenzhak, Sophie, M., "A Poly (vinyl alcohol) / Carbon-Black Composite Film: A Platform for Biological Macromolecule Incorporation." *Advanced Materials*, vol 16, pp 592 – 596, Apr 2004.

[2] Dereniak, E.L., Boreman, G.D. *Infrared Detectors and Systems*. New York: John Wiley & Sons, Inc., 1996.

[3] Laser Components (UK) Ltd., "Pyroelectric Detectors in Theory and Practice." Application Notes, 1999

[4] Kruse, Paul, W., Skatrud, David, D., *Uncooled Infrared Imaging Arrays and Systems.* Boston, MA: Academic Press, 1997.

[5] Joachim et al., "Characterization of selective polysilicon deposition for MEMS resonator tuning," JMEMS vol 12, pp 193 – 200, 2003.

[6] Hudson, Richard, D. *Infrared Detectors.* Halsted Press: John Wiley & Sons, 1975.

[7] Newsome, R.W., "Measurement of the pyroelectric coefficient of poly(vinylidene fluoride) down to 3 K," *The Amercian Physical Society*, vol 55, num 11, pp 7264 – 7271, 1997.

VI. Conclusions and Recommendations

6.1 Chapter Overview

This chapter will be broken into two separate sections, a conclusion section, and a recommendation section. The conclusion section will describe some of the highlights from each of the chapters to include observations that were made, and present the contributions that this research will give the scientific community. The recommendation section will describe some of the remedial actions required to fix the shortfalls in the FOMs and to realize the ultimate objective, an IR FPA detection system using PVA_CB. Also, additional experimental data will be presented to demonstrate another feature in the PVA_CB material, the piezoelectric effect.

6.2 Conclusions

6.2.1 Thesis Summary

Chapter 1 gave a brief discussion on the background of using the first-ever biomimetic thermal sensing material. The background to this thesis topic was then presented, demonstrating that AFRL/MLPJE proved, on the macroscopic scale, that the PIP material was thermally responsive to the IR. This was a good transition to the problem statement: to move from the macro-world to the micron world in an effort to find the FOMs that govern the performance of the material/pixel.

Chapter 2 presented background describing many types of thermal detectors. Since it was found that PIP was a pyroelectric material (shown in Chapter 3), a more in depth discussion was made on the theory and practice of pyroelectric devices. This

chapter was used as the foundation for any discussions made throughout the rest of the document.

Chapter 3 began with a discussion on how the PIP material was found to be pyroelectric. The preparation of the sample was then discussed, describing the pixel structure and how the material was deposited at the micron scale. After the material was deposited onto the pixel, it was considered an IR detector which could then be characterized with FOMs.

The intent of Chapter 4 was to define how the FOMs were to be either analytically or experimentally found. These FOMs included the pyroelectric coefficient, responsivity, thermal/electrical time constants, noise equivalent power, and detectivity. Once a thermal response was found from the pixel, these FOMs could then be easily obtained.

Chapter 5 both presented and analyzed the results for the FOMs. The TlpA protein was found to hinder the performance of the material operating as a pyroelectric device. Therefore, the PVA_CB was used as the material of choice for deposition and detector characterization. The pyroelectric coefficient showed performance characteristics orders of magnitude better than current pyroelectric polymers that are used. The pyroelectric coefficient for PVA was 755.11 nC/(cm^2 K) and for the PVA_CB, 108.32 nC/(cm^2K). The detector FOMs for the PVA_CB detector were inferior in comparison to off-the-shelf thermal detectors. NEP_{HeNe} was found to be 21.3 nW, with a D^*_{HeNe} equal to 1.93 x 10^5 $\frac{cm\sqrt{Hz}}{W}$. The main reason for this was the pixel design. When the PVA_CB was inkjet deposited onto the MEMS structure, thermal isolation was lost

which decreased significantly dT/dt which can be found in almost all of the expressions for the FOMs. Therefore, future research efforts need to concentrate on the pixel design which will further improve detector performance.

6.2.2 Scientific Contributions of this Thesis

The research discussed in this thesis will benefit the DOD and the IR detector community with several novel contributions.

1. Identified a new pyroelectric material that shows extreme potential for use as the active region in a thermal imaging system.
2. Demonstrated that inkjet deposition is an effective method to strategically deposit micron sized droplets (with the ability to control layer thickness) of a pyroelectric polymer material.
3. Devised a unique approach to finding the NEP by attenuating a HeNe thermal source with a neutral density filter while simultaneously monitoring (real-time) the SNR until the background noise variance equaled the signal output (definition of NEP).
4. Analyzed shortfalls in FOMs due to the pixel design and its lack of thermal isolation. Correcting this will achieve higher performing detector FOMs and pave the way for an FPA imaging system using this material.

6.3 Recommendations

Several recommendations were briefly mentioned in previous chapters. Here, the recommendations will be elaborated upon to provide a research vector worth considering.

The less than desirable FOMs found from the MEMS pixel can be attributed to the lack of thermal isolation. Maintaining thermal isolation while withstanding the force of the inkjetted droplet of material needs to be addressed. One consideration would be to use a bulk micromachining technique that incorporates a two-mask photolithography process. Basically, a cantilever of silicon nitride (SiN) will be suspended over a wet-etched cavity of silicon (Si). In an effort to electrically interact with the PIP material, interdigiized electrodes will be deposited onto the SiN cantilever. Using this technique, the user has control over the thermal isolation of the pixel.

Figure 65 illustrates the envisioned design of a PVA_CB-based imaging system. Due to the droplet size of the PVA_CB (180 µm in diameter), there is a limitation to the dimensions of the pixel.

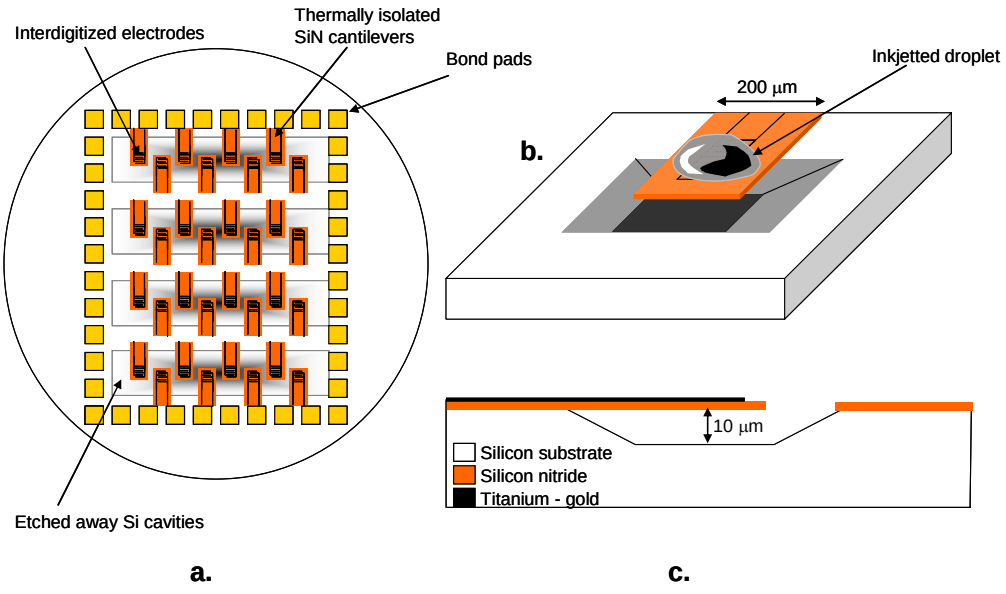

Figure 65: An envisioned design for a focal plane array PIP imaging system. **a.)** Construction of an 8 x 4 focal plane array design. **b.)** Thermal isolation is achieved from the underlying bulk etched substrate using a SiN cantilever. The diameter of the inkjet deposited droplet is 180 µm therefore the cantilever width was designed for 200 µm. **c.)** A cross-sectional view of the pixel. The isolation is user controlled with etch time.

It is shown in Figure 65b that the width of one pixel needs to be ~ 200 μm. Also, a FPA of 100 x 100 pixels is envisioned, and can be seen in Figure 66. The dimensions were based off a single inkjet droplet of the PIP material. Using the dimensions shown in Figure 66a, a 100 x 100 pixel-FPA can be fabricated on a 3 cm x 3.3 cm sample. This design will allow for thermal isolation by giving the PVA_CB droplet a platform to be dispensed upon. The thermal isolation will be achieved by the etched-out substrate. Also, the thinner the SiN layer, the higher the dT/dt. Therefore, a study is needed to determine the minimal thickness of the SiN cantilever that will withstand the force of an inkjetted droplet of PVA_CB.

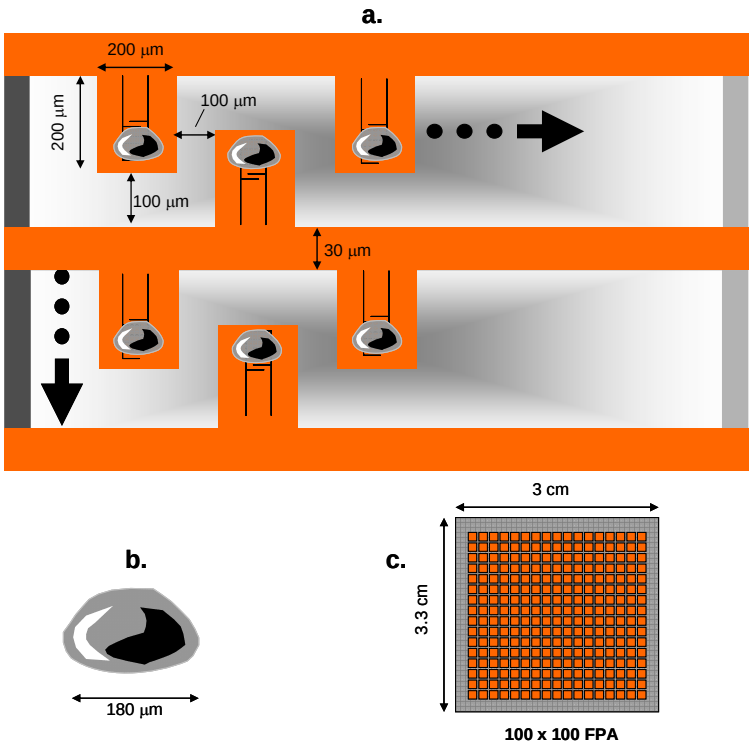

Figure 66: a.) The dimensions of the envisioned FPA using inkjetted droplets of PIP. **b.)** The design is based off the dimensions of a single inkjet droplet that was studied in this thesis. **c.)** Using the dimensions found in **a.)** a 100 x 100 pixel FPA can be fabricated on a 2.3 cm x 2 cm sample.

This thesis used a voltage preamplifier to amplify the signal's thermal response. Ideally, each pixel would have its own integrated circuit amplifier (as in Figure 19 or Figure 20) and a readout circuit that amplified and read each pixel's electrical output in a sequential process. There are many articles published that discuss monolithic readout circuits that could be used in the PIP-based FPA. The reader and follow-on researcher is referred to [1,2] for insight on read-out-circuit designs. Since CMOS is compatible with the envisioned design shown in Figure 66, the amplifier and readout circuit could be designed with 37 transistors in an area of 6 μm x 6 μm [1], which is a small enough real-estate that it can be accommodated by each pixel.

6.4 Other Features of PVA_CB

Since the PIP material was found to be ferroelectric, there are a few other factors that are worth mentioning about the material studied in this thesis. Recall that all ferroelectric materials are pyroelectric, and subsequently, all pyroelectric materials are piezoelectric. This gives PIP all of these unique properties. These unique properties can lead to potential applications and are worth investigating for future research.

First, piezoelectric materials will generate a voltage when compressed and, conversely, have a conformal change in shape in the presence of an electric field. A simple experiment was conducted to demonstrate this concept. The sample shown in Figure 21 using PIP as the material under test was placed under the Zygo (white light interferometer). Once a good fringe pattern was found, a 100 μm upward scan was measured which captured an image. The sample was then biased for ~ 5 min with 100 V and another 100 μm scan using the Zygo was taken. Thus, two images of the exact same

spatial location were taken (one with zero bias, and the other with a 100 V bias) to see if the piezoelectric effect is present. This piezoelectric experiment is seen in Figure 67.

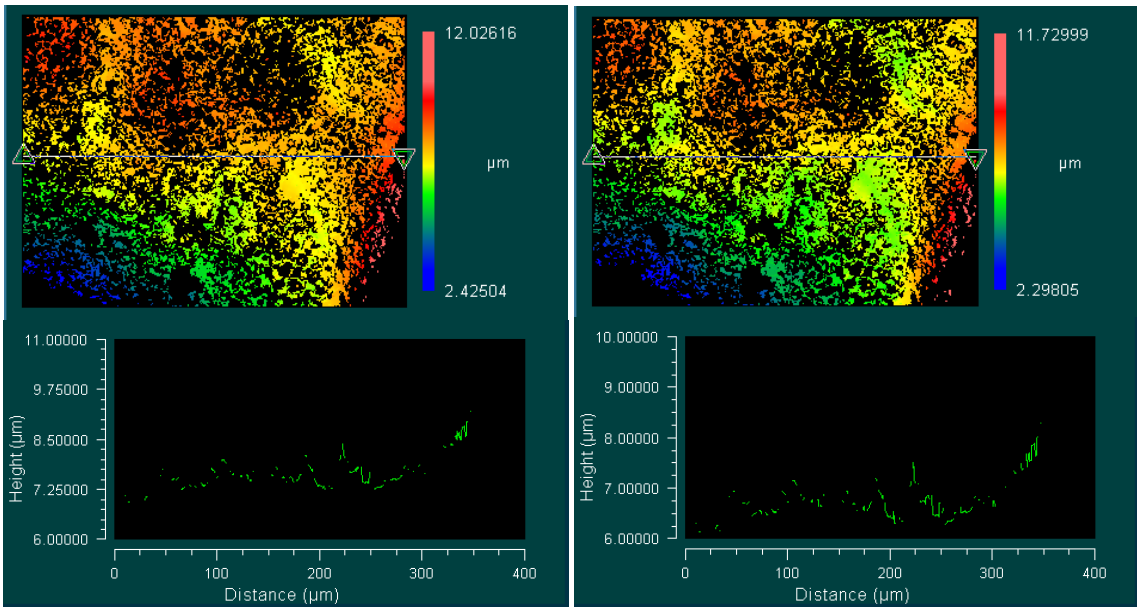

a. **b.**

Figure 67: Zygo images illustrating PIP's piezoelectric effect. **a.)** An image of PIP deposited onto one of the electrodes (with no bias applied). **b.)** The same image taken after the sample was bias at 100 V for 5 minutes. It is evident from these two images that the ionic makeup of the material seems to traverse toward the respective electrodes there by thinning the material by ~ 0.26 µm in the presence of an electric field.

Since the PIP material is black, less than ideal images were captured due to the absorption of the incident light. In Figure 67a, an image was first captured with the material in steady state conditions, and in Figure 67b an image of the same location was captured after ~ 5 minutes of the material being biased with 100 V. The ionic makeup of the material constituents appeared to cause ion movement toward an electrode, thereby decreasing the thickness of the material in the Zygo's field of view. The material thickness decreased by ~ 10.7 % (~0.26 µm) in the presence of an electric field. Many

applications can be realized with materials that have piezoelectric properties, leaving further research into exploiting PIP's piezoelectric properties.

6.5 Chapter Summary

The PVA_CB material demonstrates excellent potential for use in an FPA thermal imager. This thesis gave insight into how much potential by characterizing the FOMs of a single detector. It was evident that the FOMs found are less than ideal and can be attributed to the lack in thermal isolation between the active region (where the PIP was deposited) and the underlying substrate. An envisioned design, shown in Figure 65, should maximize isolation even after deposition, thereby enhancing the FOMs. An IR image should be achievable in three thesis research efforts from now. The next follow-on should concentrate on fabricating the SiN cantilever designs which can be characterized with improved FOMs compared to FOMs in this thesis. Research following that effort should focus on the amplification/readout integrated circuit, co-located with the pixel, to optimize circuit design by monitoring output signal integrity. Lastly, a systems approach thesis should integrate these four theses with the end-state of capturing an IR image with all components manufactured/characterized in-house.

6.6 Works Cited

[1] Kleinfelder, Stuart, et al, "A 10,000 Frames/s CMOS Digital Pixel Sensor," *IEEE Journal of Solid-State Circuits,* vol 36, pp 2094 – 2059, Dec 2001.

[2] Hsieh, Chih-Cheng, et al, "Focal-Plane-Arrays and CMOS Readout Techniques of Infrared Imaging Systems," *IEEE Transactions on Circuits and Systems for Video Technology,* vol 7, pp 594 – 605, Aug 1997.

Appendix A: The PolyMUMPs® Process

PolyMUMPs®, is a commercial fabrication process that uses a three-layer polysilicon surface micromachining method which is available to universities and professionals in industry. The MEMS devices can be constructed in a CAD-based program called L-edit. These designs are then submitted to MEMSCAP, which is the company that uses the PolyMUMPs® foundry. There is an approximate turn-around-time of two months from design submittal until the devices are fabricated and returned. This appendix will be dedicated to give an overview of the fabrication process. The reader is to refer to contact MEMSCAP for more detailed information.

The fabrication process starts with a clean 100 mm diameter, (100) orientatation n-type silicon wafer. First, a 0.6 μm layer of silicon nitride (SiN) is deposited by way of low pressure chemical vapor deposition (LPCVD). The SiN is extremely resistive, and acts as the electrical insulating layer. Second, a 0.5 μm layer of polysilicon, termed Poly-0, is deposited on top of the SiN. Standard photolithographic processes are used with the Poly 0 mask to define where the Poly-0 layer will remain by blanketing those areas with photoresist. The unwanted regions are then removed using a reactive ion etch (RIE). Next, the first of two releasable layers is deposited. This layer is made of phosphosilicate glass (PSG), which is used as a sacrificial layer, and is termed Oxide-1. At this point, the wafer is then annealed in argon, for ~ 1 hr at 1050 °C. Two more photolithographic mask sets are then accomplished to remove portions of the Oxide-1 where the dimples are formed, followed by an Anchor-1 etch. The dimple etch removes 0.75 μm (in depth) of

the Oxide-1 layer, while the Anchor-1 etch removes the entire thickness of the Oxide-1 layer.

The next step deposits another layer of polysilicon, this time called Poly-1. On top of this layer is also deposited another PSG layer, which is again mitigates residual stress in the Poly-1 layer. This PSG layer is annealed at 1050 °C, and acts as a hard mask for the RIE of the Poly-1. Once this process is complete, a second oxide layer with a thickness of 0.75 μm is deposited, termed Oxide-2.

Two etches are possible on the Oxide-2 layer, Poly-1_Poly-2_Via or Anchor-2. The Via etch is used to remove Oxide-2, and the Anchor-2 etch is used to remove both Oxide-1 and Oxide-2 layers. The last polysilicon layer is then deposited, called Poly-2. Again, on top of Poly-2, in an effort to mitigate residual stress, another PSG layer is deposited and annealed. The last step in the PolyMUMPs process is to deposit a thin layer of gold. This 0.5 μm layer of gold is evaporated onto the wafer where the unwanted areas are removed using lift-off. The gold layer only adheres to the Poly-2 layer. The layer compositions used in the PolyMUMPs process are seen in Figure 68.

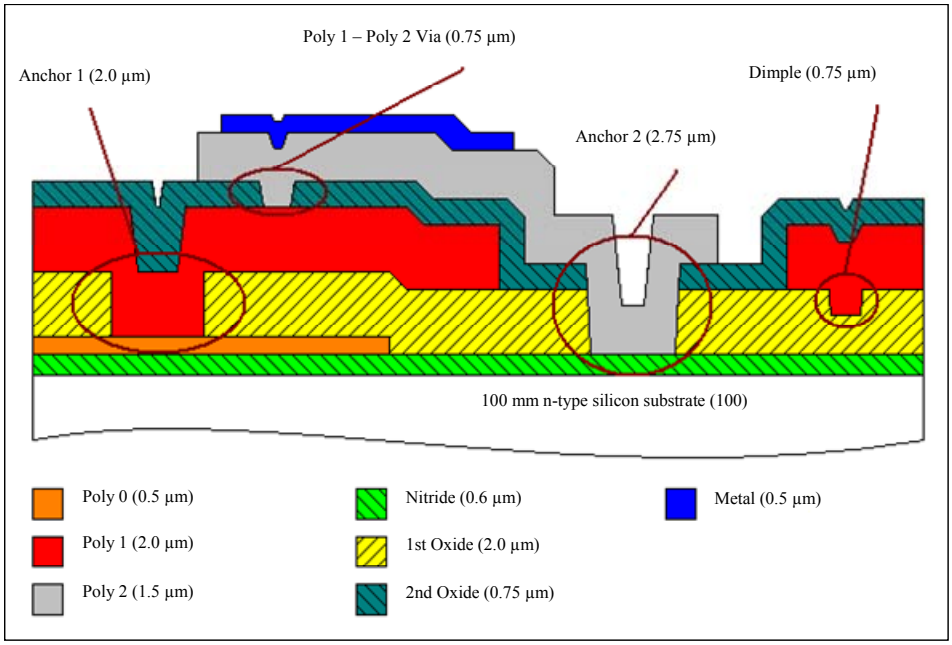

Figure 68: The layer composition of the PolyMUMPs process. The pixels that were used in this thesis were constructed using this process.

Appendix B: The PolyMUMPs® Design

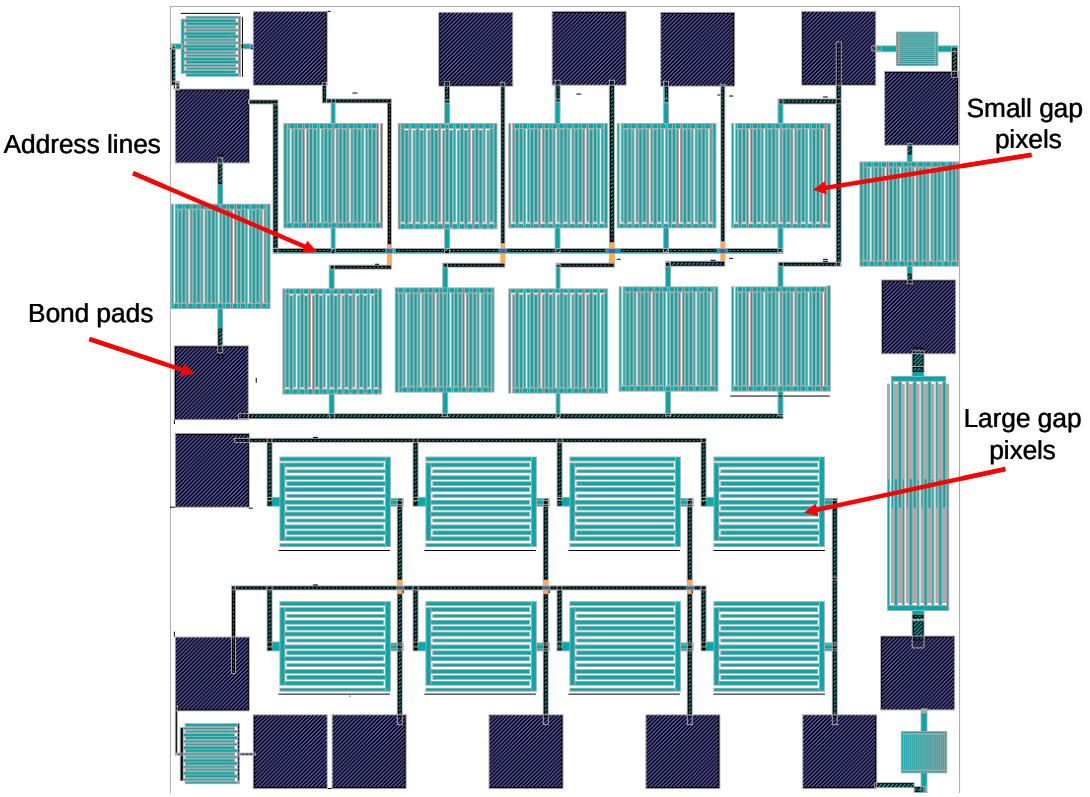

Figure 69: PolyMUMPs run 73.

MUMPs®: 73 (original designs)

Layout: Variations of pixel designs using the top two layers of the PolyMUMPs process (Poly-2/gold). Each pixel is electrically connected using a row-column addressing scheme. The wires were made from Poly-2/gold/anchor -2. The bond pads allow for wirebonding to a chip package to connect to outside world.

Comments: All pixel designs did not support the weight of the PVA_CB, proving the interdigitized finger structures less than ideal for inkjet deposition.

Vita

First Lieutenant Allard was born in Utica, NY. Upon graduating from high school he attended a two-year college where he obtained an associates degree in general studies.

On 21 Feb 1996, Lt Allard enlisted in the USAF. After finishing tech school, specializing as a technician in satellite and wideband communication, Lt Allard was stationed at Keesler AFB, as a maintenance journeyman. From Keesler, he was sent to Kuwait in support of operation Southern Watch. In Apr of 1999, Lt Allard was assigned to the 50th Communication Squadron at Schriever AFB, as an Air Force Satellite Control Network (AFSCN) liason.

In Jun of 2001, Lt Allard was accepted into airmen education and commissioning program (AECP), where he attended Colorado Technical University, receiving his undergraduate degree in electrical engineering. After graduating from OTS in Apr 2003, Lt Allard was assigned to the 746 Test Squadron at Holloman AFB, where he earned the distinction of lead flight test engineer. His developmental test and evaluation flight test experience touched numerous high visibility programs, to include joint precision and approach landing systems (JPALS), joint attack surface standoff missile (JASSM), and small diameter bomb (SDB). He has accrued over 139 hrs of flight test experience in four different aircrafts (C-12J / C-12D / MH-60 / MH-53).

First Lieutenant Allard is currently a student in the physics department at the Air Force Institute of Technology (AFIT). He is scheduled to graduate in Mar 2007, with a degree in Electro-Optics. His master's thesis on characterizing an in-house designed

infrared (IR) thermal detector, using a novel pyroelectric material, laid the foundation for future research in developing an IR camera, which could reach the theoretical performance limits. Following AFIT, 1Lt Allard will serve in the biomimetics branch at the Air Force Research Laboratory.

REPORT DOCUMENTATION PAGE

Form Approved
OMB No. 074-0188

1. REPORT DATE *(DD-MM-YYYY)*	2. REPORT TYPE	3. DATES COVERED *(From – To)*
22-03-2007	Master's Thesis	Aug 2005 – March 2007

4. TITLE AND SUBTITLE

CHARACTERIZATION OF POLYMER-BASED MEMS PYROELECTRIC INFRARED DETECTOR

5a. CONTRACT NUMBER

5b. GRANT NUMBER

5c. PROGRAM ELEMENT NUMBER

6. AUTHOR(S)

Allard, Mark E., 1Lt, USAF

5d. PROJECT NUMBER
N/A

5e. TASK NUMBER

5f. WORK UNIT NUMBER

7. PERFORMING ORGANIZATION NAMES(S) AND ADDRESS(S)
Air Force Institute of Technology
Graduate School of Engineering and Management (AFIT/EN)
2950 Hobson Way, Building 640
WPAFB OH 45433-8865

8. PERFORMING ORGANIZATION REPORT NUMBER
AFIT/GEO/ENG/07-01

9. SPONSORING/MONITORING AGENCY NAME(S) AND ADDRESS(ES)
Air Force Research Laboratory (AFRL/MLPJE)
3005 P Street, Bldg 651
Wright-Patterson AFB, OH 45433-7702
(937) 255-3808, ext 3174
(Lawrence.Brott@wpafb.af.mil)

10. SPONSOR/MONITOR'S ACRONYM(S)

11. SPONSOR/MONITOR'S REPORT NUMBER(S)

12. DISTRIBUTION/AVAILABILITY STATEMENT

APPROVED FOR PUBLIC RELEASE; DISTRIBUTION UNLIMITED.

13. SUPPLEMENTARY NOTES

14. ABSTRACT

AFRL/MLPJE had developed a novel thermal sensing material termed protein- impregnated-polymer (PIP). Thus far, a proof-of-concept has been demonstrated using a macro-sized pixel (0.64 mm^2) as a bolometric detector. In an effort to better characterize this novel thermal sensing material, experimental data was used to determine figures of merit (FOMs) comparative to off-the-shelf thermal detectors. Microelectromechanical (MEMS) pixels were designed and used as the support structure for an inkjet-deposited droplet of the PIP. During the material characterization, two observations were made: PIP is a pyroelectric material, and the polymer (polyvinyl alcohol (PVA)) without the protein was found to be more suited for measurements taken on the micro-scaled pixels. Both PVA and PVA doped with carbon black (PVA_CB) were the materials focused on in this research, with the latter being the material used for FOM characterization. Pyroelectric coefficients for PVA and PVA_CB were found to be 755.11 nC/(cm^2 K), and 108.32 nC/(cm^2 K), respectively, which are both two orders of magnitude higher than values for current pyroelectric polymers. A responsivity of 1.66×10^4 V/W, thermal time constant of 3.59 sec, noise equivalent power of 21.3 nW, and a detectivity of 1.93×10^5 cm $Hz^{1/2}$ /W were the FOMs found in this thesis. Although the calculated FOMs are not stellar in comparison to current thermal detector technology, this material shows much promise. The shortfalls in FOMs could potentially be attributed to a poor pixel design. This thesis plants the scientific seed in cultivating a thermal imaging focal plane array (FPA) using a newly found pyroelectric polymer.

15. SUBJECT TERMS
MEMS, pyroelectric, bolometric, uncooled, thermal detector, figure of merit (FOM), polyvinyl alcohol (PVA)

16. SECURITY CLASSIFICATION OF:			17. LIMITATION OF ABSTRACT	18. NUMBER OF PAGES	19a. NAME OF RESPONSIBLE PERSON
a. REPORT	b. ABSTRACT	c. THIS PAGE			Fellows, James, A., Lt Col, USAF
U	U	U	UU	173	19b. TELEPHONE NUMBER *(Include area code)* (937) 785-3636, ext 7230 (James.Fellows@afit.edu)

Standard Form 298 (Rev. 8-98)
Prescribed by ANSI Std. Z39-18